

Electronic Theses and Dissertations, 2004-2019

2015

Inverse-Consistent Determination of Young's Modulus of Human Lung

Behnaz Seyfi Noferest
University of Central Florida

 Part of the [Biomechanical Engineering Commons](#)
Find similar works at: <https://stars.library.ucf.edu/etd>
University of Central Florida Libraries <http://library.ucf.edu>

This Doctoral Dissertation (Open Access) is brought to you for free and open access by STARS. It has been accepted for inclusion in Electronic Theses and Dissertations, 2004-2019 by an authorized administrator of STARS. For more information, please contact STARS@ucf.edu.

STARS Citation

Seyfi Noferest, Behnaz, "Inverse-Consistent Determination of Young's Modulus of Human Lung" (2015).
Electronic Theses and Dissertations, 2004-2019. 5149.
<https://stars.library.ucf.edu/etd/5149>

INVERSE-CONSISTENT DETERMINATION OF YOUNG'S MODULUS OF HUMAN
LUNG

by

BEHNAZ SEYFI NOFEREST
B.Sc., K.N. Toosi University of Technology, 2007
M.Sc., University of Central Florida, 2012

A dissertation submitted in partial fulfillment of the requirements
for the degree of Doctor of Philosophy
in the Department of Mechanical and Aerospace Engineering
in the College of Engineering and Computer Science
at the University of Central Florida
Orlando, Florida

Fall Term
2015

Major Professor: Olusegun J. Ilegbusi

© 2015 Behnaz Seyfi Noferest

ABSTRACT

Human lung undergoes respiration-induced deformation due to sequential inhalation and exhalation. Accurate determination of lung deformation is crucial for tumor localization and targeted radiotherapy in patients with lung cancer. Numerical modeling of human lung dynamics based on underlying physics and physiology enables simulation and virtual visualization of lung deformation. Dynamical modeling is numerically complicated by the lack of information on lung elastic behavior, structural heterogeneity as well as boundary constraints. This study integrates physics-based modeling and image-based data acquisition to develop the patient-specific biomechanical model and consequently establish the first consistent Young's modulus (YM) of human lung.

This dissertation has four major components: (i) develop biomechanical model for computation of the flow and deformation characteristics that can utilize subject-specific, spatially-dependent lung material property; (ii) develop a fusion algorithm to integrate deformation results from a deformable image registration (DIR) and physics-based modeling using the theory of Tikhonov regularization; (iii) utilize fusion algorithm to establish unique and consistent patient specific Young's modulus and; (iv) validate biomechanical model utilizing established patient-specific elastic property with imaging data

The simulation is performed on three dimensional lung geometry reconstructed from four-dimensional computed tomography (4DCT) dataset of human subjects. The heterogeneous Young's modulus is estimated from a linear elastic deformation model with the same lung

geometry and 4D lung DIR. The biomechanical model adequately predicts the spatio-temporal lung deformation, consistent with data obtained from imaging. The accuracy of the numerical solution is enhanced through fusion with the imaging data beyond the classical comparison of the two sets of data. Finally, the fused displacement results are used to establish unique and consistent patient-specific elastic property of the lung.

To my lovely parents

ACKNOWLEDGMENTS

I would like to thank my Ph.D. advisor, Dr. Olusegun Ilegbusi for supporting this project intellectually and financially. His trust and dedication encouraged me to embark on this research project and pursue it towards the end. Special thanks to my co-advisor, Dr. Anand Santhanam with the University of California Los Angeles, for his advisement and inputs to this research.

I am truly grateful to my other committee members, Dr. Alain Kassab and Dr. Faisal Moslehy for their guidance. Specifically, I would like to thank Dr. Kassab who always offered support and guidance to me during the years of my graduate education.

I am grateful to the members of our research group especially Nadun Kuruppumullage for his constant friendship and support. I am thankful to many of my friends for their sincere help and friendship. Specifically, Reza Akhavian for his endless compassion, motivation, help, and support.

I am also very thankful to my loyal and supportive friend and roommate, Zahoora Sanjabi.

Last, but not least, I would like to thank my beloved family. Thanks to my lovely parents for always believing in me and inspiring me to do my best. I am always grateful for all sacrifices they have made and for all they have done for me. Special thanks to my wonderful sister, Bahareh and his beloved husband, Hamid. I cannot thank you enough for encouraging me throughout this experience. I also would like to thank my caring siblings, Behnam, Behnoush, and Sepideh.

I acknowledge the support of the National Science Foundation (NSF) that supported this project financially under the grant number #CMMI-1200841.

TABLE OF CONTENTS

ABSTRACT.....	iii
ACKNOWLEDGMENTS	vi
TABLE OF CONTENTS.....	vii
LIST OF FIGURES	xii
LIST OF TABLES	xv
CHAPTER 1: INTRODUCTION.....	1
1.1 Problem Statement	1
1.2 Research Objectives	3
1.3 Organization of the Dissertation	4
CHAPTER 2: LITERATURE REVIEW	6
2.1 Physiology of the Respiratory System	6
2.2 Mechanical Properties of Lung Parenchyma	7
2.2.1 Tensile Tests	8
2.2.2 Elastography	8
2.3 Constitutive Equations	9
2.3.1 Solid Models	9
2.3.2 Two Phase Models	12

2.4	Biomechanical Modeling of Human Lung.....	13
2.4.1	Material Models	14
2.4.2	Effect of Gravity	18
2.4.3	Boundary Conditions	20
2.4.4	Accuracy of Biomechanical Models.....	22
2.4.5	Efficiency of Biomechanical Models.....	23
2.5	Integration of Experimental and Simulation Methods	24
CHAPTER 3: PATIENT- SPECIFIC MODEL OF LUNG DEFORMATION USING		
SPATIALLY DEPENDENT CONSTITUTIVE PARAMETERS.....		
3.1	Introduction	26
3.2	Materials and Methods.....	28
3.2.1	Principle	28
3.2.2	Governing Equations	29
3.2.3	Lung Geometry	30
3.2.4	Analysis and Boundary Condition.....	31
3.2.5	Material Properties.....	33
3.2.6	Implementation	35
3.3	Results and Discussion.....	36
3.4	Summary	40

CHAPTER 4: MODELING AND VALIDATION OF HUMAN LUNG DEFORMATION	41
4.1 Introduction	41
4.2 Materials and Methods	42
4.2.1 Image Registration	43
4.2.2 Biomechanical Modeling	44
4.3 Computational Details	51
4.4 Results	52
4.5 Discussion	60
CHAPTER 5: ANALYTIC INTERMODEL CONSISTENT MODELING OF VOLUMETRIC HUMAN LUNG DYNAMICS	62
5.1 Introduction	62
5.2 Materials and Methods	64
5.2.1 Fusion Algorithm	64
5.2.2 4DCT Registration using Optical Flow (<i>f4DCT</i>)	66
5.2.3 CFD Model Analysis (<i>fCFD</i>)	67
5.3 Results	72
5.3.1 Image Registration Results	72
5.3.2 CFD Results	75
5.3.3 Optimal Results from Fusion Algorithm	76

5.3.4	Validation.....	77
5.4	Conclusion.....	81
5.5	Nomenclature	83
5.6	Appendix: Numerical Solution of the Objective Functional.....	86
CHAPTER 6: EFFECT OF GRAVITY ON SUBJECT-SPECIFIC HUMAN LUNG DEFORMATION		91
6.1	Introduction	91
6.2	Materials and Methods.....	92
6.2.1	Geometry Reconstruction and Mesh Generation	92
6.2.2	Governing Equations	94
6.2.3	Computational Details	96
6.2.4	Input Data.....	97
6.2.5	Boundary Condition and Applied Loading.....	98
6.3	Results	100
6.4	Summary and Conclusions.....	109
CHAPTER 7: CONCLUSIONS AND FUTURE WORK.....		111
7.1	Summary of Chapters.....	111
7.2	Suggestions for Future Work	112
7.2.1	Broader Application of Fusion Algorithm.....	112

7.2.2	Determination of Elastic Properties of Human Upper Airway.....	113
7.2.3	Improve Computational Time.....	113
7.2.4	Pulmonary Fibrosis.....	114
7.2.5	Modeling Airflow in Human Lung.....	114
7.2.6	Effect of ribcage on Heterogeneous Model of Human Lung.....	115
APPENDIX A: COPYRIGHT PERMISSION.....		116
APPENDIX B: AUTHOR’S BIOGRAPHY.....		118
REFERENCES.....		120

LIST OF FIGURES

Figure 2-1: The primary components of the chest wall adapted from Ref. [9]	6
Figure 2-2: Illustration of the contact–impact analysis approach. The lung is expanded starting from the initial geometry and restricted by the limiting geometry. The expansion occurs due to the negative pressure applied to the lung surface.	21
Figure 3-1: Lung shapes derived from 4D-CT scans: (a) a section of the lung surface meshed with shell elements; (b) a section of the solid model meshed with tetrahedral elements	31
Figure 3-2: Prescribed inlet pressure profile, pressure condition is imposed at inlet locations of the fluid mesh.....	32
Figure 3-3: Schematic of repartitioning of the voxel points to match the 3D lung geometry derived from 4DCT scans used in simulation (a) front view (b) top view. Each element used in the computation is associated with the closest voxel point.	34
Figure 3-4: Schematic illustrating implementation of patient-specific elastic property data.	35
Figure 3-5: Predicted amplitude map of displacement magnitude in (mm) at the end of inhalation: (a) heterogeneous model, (b) homogenous model.....	37
Figure 3-6: Displacements of nodes (a) P1 and (b) P2 in the vertical (SI) direction at end inhalation (dotted lines represent the spatially-dependent material model, dashed lines represent the linear model with $E = 80,000$ Pa and 8000 and solid lines represent the linear model with $E = 800$ Pa).	39
Figure 4-1: Processing pipeline diagram illustrating various steps involved in the determination of the image-based and model-based displacements.....	43

Figure 4-2: Three-dimensional volume rendering of the Young’s modulus values for (a) Patient 1 (b) Patient 2.....	47
Figure 4-3: Prescribed boundary pressure profile.....	51
Figure 4-4: Predicted amplitude map of displacement magnitude in (mm) at the end of inhalation for (a) Patient 1 (b) Patient 2.....	53
Figure 4-5: Average absolute error and standard deviation for four regions of the left and right lungs for (a) Patient 1 (b) Patient 2.....	55
Figure 4-6: Comparison of prediction displacement for monitored landmarks located at the (a) top (b) middle and (c) bottom of the left lung over the inhalation phase	58
Figure 4-7: Comparison of prediction displacement for monitored landmarks located at the (a) top (b) middle and (c) bottom of the right lung over the inhalation phase	59
Figure 5-1: Three dimensional lung shapes generated from 4D-CT scan; (a) surface meshes (b) cutout of a section of reconstructed lungs, typical computational volume meshes generated and applied in the finite element model.....	69
Figure 5-2: Prescribe inlet pressure	72
Figure 5-3: 3DCT lung anatomy used as the reference geometry for the CFD analysis	73
Figure 5-4: Lung deformation along the (i) x axis, (ii) y axis, and (iii) z axis computed for the (a) left lung and (b) right lung using a multi-resolution optical flow algorithm.....	74
Figure 5-5: Three-dimensional volume rendering of the Young’s modulus values for the (a) right and (b) left lung obtained from the 4DCT lung registration and a linear deformation model.....	75
Figure 5-6: Lung deformation along the (i) x axis, (ii) y axis, and (iii) z axis computed for the (a) left lung and (b) right lung using CFD model.....	76

Figure 5-7: Optimal lung deformation along the (i) x axis, (ii) y axis, and (iii) z axis computed for the (a) left lung and (b) right lung.....	77
Figure 5-8: Differences in the displacement observed between the optimal lung deformation and the deformation observed in the 4D-CT DIR shown for (a) left and (b) right lungs.....	78
Figure 5-9: Location of selected landmarks in (a) left and (b) right lung.....	81
Figure 6-1: Images of human lungs in (a) frontal (b) horizontal(c) lateral, and (d) 3D views.....	93
Figure 6-2: Three-dimensional geometry of human lung reconstructed from 4DCT scans.....	93
Figure 6-3: Gravity direction assumed in the model.....	99
Figure 6-4: Time functions used in the simulation.....	100
Figure 6-5: Predicted magnitude of deformation (in mm) due to the weight of the lung (gravity-induced deformation) in (a) left lung, (b) right lung.....	101
Figure 6-6: Predicted displacement in x, y, and z direction (in mm) due to (a) pressure loading only, and (b) both maximum gravity loading and pressure loading.....	103
Figure 6-7: Comparison between magnitude of displacement obtained by the model (a) without gravity and (b) with gravity for selected slices in the lung.....	105
Figure 6-8: Location of monitored landmarks A, B, and C.....	106
Figure 6-9: Predicted displacements over one breathing cycle for monitored landmarks A, B and, C with and without gravity.....	108
Figure A-1: ASME permission to reuse the published paper in Chapter 5 of this Dissertation.	117

LIST OF TABLES

Table 2-1: Strain energy density functions of lung parenchyma proposed in previous studies ...	11
Table 2-2: Young modulus values and Poison ratio applied in linear finite element model of lungs	16
Table 4-1: Number of computational elements and nodes used in the biomechanical model.....	52
Table 4-2: Average absolute error of homogenous and heterogeneous models for landmarks at the bifurcation of airway.....	56
Table 5-1: Discrepancy observed between the CFD (deformation) results using initial YM values and CFD (deformation) results using optimal YM values (mm) and the deformation observed in 4DCT DIR.....	80
Table 6-1: Average absolute error of models without and with gravity for 3 layers in Figure 6-7	105

CHAPTER 1: INTRODUCTION

1.1 Problem Statement

This study aims to develop and apply biomechanical model to accurately predict respiration induced lung deformation. External beam radiotherapy is a local treatment technique which aims to expose cancerous tumor from several directions while minimizing exposure to the surrounding tissue [1]. However, respiration-induced tumor motion constitute potential source of error in tumor localization for optimum radiotherapy [2, 3] lead to an under-treatment of the tumor and overexposure of the surrounding healthy lung tissues to unnecessary ionizing radiation [2]. Precise estimation of lung tumor position can be facilitated by means of biomechanical modeling, based on physics and physiology.

The key steps towards the development of subject-specific three dimensional (3D) volumetric lung models is the estimation of the appropriate elastic property of human lung. This study present a novel method to fuse biomechanical modeling with imaging data to establish for the first time consistent patient-specific Young's modulus of human lung. Specifically, the approach utilizes a mathematical formulation that fuses the deformation results from a deformable image registration (DIR) and physics-based modeling using the theory of Tikhonov regularization. The fused displacement result is then used to establish consistent elastic property of human lung.

Recent advances in Computed Tomography (CT) [4] and Magnetic Resonance (MR) [5] acquisition techniques have enabled direct dynamic imaging of respiratory motion. In addition, deformable image registration (DIR) methods [1] coupled with biomechanical modeling of the lung facilitates precise estimation of respiration-induced lung tumor motion. However, biomechanical modeling is challenging due to the lack of information on lung elastic behavior, complexity of lung geometry, structural heterogeneity, fluid–structure interaction between air and the tissue, and boundary constraints. The following summarizes the major deficiencies in the current status of lung biomechanical modeling studies which are addressed in this dissertation:

- Human lung is heterogeneous with a wide spatial variation of elastic property [6]. This situation is further exacerbated by the presence of tumors, which significantly increase the local elastic modulus due to stiffness. Most previous modeling studies have ignored this inherent heterogeneity of lung tissue. In addition, the reproducibility and accuracy of the existing simulation studies could not be ascertained when applied to different patients, since all patients were modelled with the same tissue properties.
- There is considerable physiological and experimental evidence of the significant effect of gravity on lung dynamics. Yet existing models have largely ignored gravity. The effect of gravity on lung deformation is considered in this dissertation.
- In spite of the growing number of studies on the dynamics of human lung, a systematic comparison of imaging data and computational results has not been undertaken. This deficiency is addressed here through direct validation of predicted lung deformation using the results of image registration.

- Errors and uncertainty are inevitable even in advanced biomechanical modeling due to model approximations. The present study introduces a fusion algorithm that integrates the displacement data from image registration with numerical simulation to obtain the optimal deformation of human lung. The algorithm uses the theory of Tikhonov regularization [7]. The optimal results are then used to establish unique and consistent patient-specific Young's modulus of human lung.

1.2 Research Objectives

The ultimate goal of this research is to establish consistent elastic property (effective Young's modulus) of human lung which does not currently exist. This will improve the accuracy of predicted lung deformation for radiotherapy application. In order to achieve the stated goal, we propose to develop a mathematical method to fuse the deformation data from tomography with biomechanical modeling using the theory of Tikhonov regularization.

The specific objectives of the study are:

- To develop biomechanical model for computation of the flow and deformation characteristics utilizing subject-specific, spatially-dependent lung material property and three dimensional (3D) geometry of real human lung.
- To develop a methodology (fusion algorithm) using the theory of Tikhonov regularization, integrating simulation and radiotherapy data for optimal solution.
- To use the fused data to establish unique and consistent patient-specific Young's modulus.

- To assess the significance of heterogeneous and subject-specific tissue elasticity on lung deformation.
- To validate the biomechanical model with image-based experimental data. Model predictions of displacement of arbitrarily chosen land marks are compared and validated with the displacement data obtained from 4D-CT registration.
- To assess the effect of gravity on lung deformation.

1.3 Organization of the Dissertation

The following Chapters of this Dissertation are shaped around the concepts, details, and implementation of the research tasks listed above. The Dissertation is divided into seven Chapters, as described below.

- Chapter 1: Introduction – This Chapter presents the problem statement, objectives of the research, and contributions made to the body of knowledge.
- Chapter 2: Literature Review – This chapter provides an overview of the state of the art on the modeling of human lung. Specifically, it describes the methods used for identification of material properties, the current knowledge of material models, and the different approaches used in biomechanical modeling.
- Chapter 3: Patient-Specific Model of Lung Deformation Using Spatially Dependent Constitutive Parameters – This Chapter presents the simulation of the breathing-induced lung deformation utilizing local elastic properties of subject-specific human lungs. The simulation uses finite element numerical model on 3D lung geometry reconstructed from

4D-CT scans. The results are compared with predictions of lung deformation assuming homogenous elastic property in order to assess the significance of inhomogeneity on lung deformation.

- Chapter 4: Modeling and Validation of Human Lung Deformation – A biomechanical model is developed and validated for breathing-induced deformation of human lung. Specifically, a subject-specific poro-elastic lung model is used to predict the displacement over the breathing cycle and compared with displacement derived from high resolution image registration.
- Chapter 5: Analytic Intermodel Consistent Modeling of Volumetric Human Lung Dynamics – In this Chapter, a mathematical method is developed to integrate deformation data from deformable image registration (DIR) and physics-based modeling to represent consistent volumetric lung dynamics. Most of the materials presented in this Chapter are previously published as a technical paper in the American Society of Mechanical Engineers (ASME) Journal of Biomechanical Engineering. The paper is reused in this Dissertation with permission from the ASME (see Appendix A).
- Chapter 6: Effect Of Gravity on Subject-Specific Human Lung Deformation – The effect of gravity is considered on biomechanical modeling of human lung deformation. The predicted deformation of selected landmarks are monitored with and without gravity, and compared with data obtained from 4DCT registration.
- Chapter 7: Conclusions – This Chapter concludes the dissertation by providing a summary of the problem statement and key findings of the research.

CHAPTER 2: LITERATURE REVIEW

2.1 Physiology of the Respiratory System

Lungs are the vital breathing organs. The right lung consists of three parts- the upper, middle and lower lobes, while the left lung has two- the upper and lower lobes because of the presence of the heart. The space between the left and right lungs is called the Mediastinum [8]. Different muscles are involved in respiration to assist the breathing process. The essential respiration muscles are the diaphragm and the intercostal muscle with the latter helping to elevate the ribcage. Figure 2-1 illustrates the lung and the associated components of the respiratory system [9].

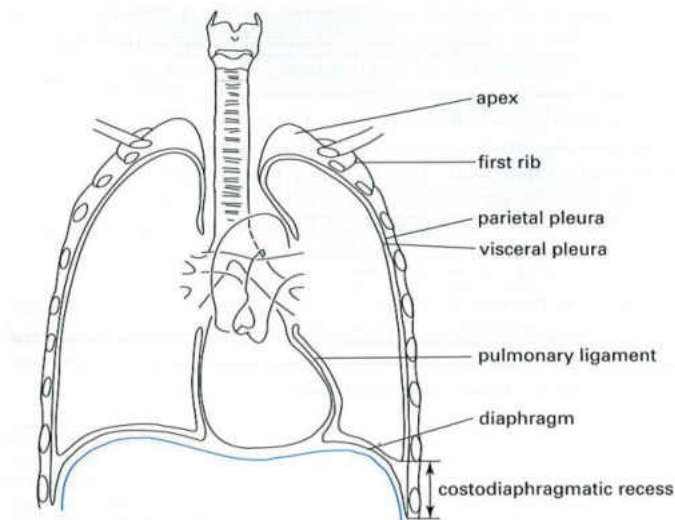


Figure 2-1: The primary components of the chest wall adapted from Ref. [9]

The interaction of the lungs with the diaphragm and the rib cage is maintained by the pleura, a two-layered membrane structure. The inner pleura called visceral pleura covers the surface of the lung and the outer pleura called parietal pleura is attached to the chest wall. The space between the two pleura structures is called the pleural space and filled with the lubricant fluid called pleura fluid. The pleura fluid makes it possible for the lung to slide against the chest cavity during the breathing process [10].

Lung inflation is due to pressure induced by the respiratory muscles of the diaphragm and rib cages. Taking the initial state of breathing to be the end of expiration with zero pressure as a reference, the contraction of the respiratory muscles causes pressure to become negative and its magnitude increases gradually during inspiration and air enters the lungs. The lungs are thus pulled open. When the respiratory muscles relax, the magnitude of pressure decreases, the lung volume decreases and air is expelled. This principle is considered in order to simulate the breathing mechanism in the current study.

2.2 Mechanical Properties of Lung Parenchyma

Like other biological tissues, the lung has a complex structure. Collagen and elastin fibers are the major components of the lung connective tissue networks and together provide the lung with its elasticity and tensile strength [11]. A lot of effort has been undertaken to develop constitutive models of the lung parenchyma as well as experimental methods to identify these models. Studies to investigate the material model of the lung have been ranged from microscopic [12] to global [13]. Some studies have also explored the connection between the global deformation of a tissue strip or the whole organ and the strains reaching the single cells lining the alveolar walls [14, 15].

Rausch et al. [15] determined that the local strain in the alveolar wall can reach a multiple of the value of the global strain.

2.2.1 Tensile Tests

Quantification of the local material property usually requires tensile tests on the tissue slices. Such experiments have been done since the late 1960s [16]. These studies usually perform uni-axial [17], bi-axial [18] and tri-axial [19] tension tests on the tissue slices. Vawter et al. (1978) [20] studied uni-axial and bi-axial loading on dog lungs and investigated the difference between tissue stiffness. The results indicate that up to a limit of stress the tissue was stiffer for bi-axial than for uni-axial loading. This behavior becomes reversed beyond the limit point.

2.2.2 Elastography

Elastography have defined as image-based estimation of biological tissue elasticity [21]. This method is usually applied to estimate the elastic parameters of the tissue. Ultrasound-based and MRI-based are two kinds of elastography. Ultrasound-based elastography is not currently used for determination of lung elastic parameters because of the high air content of lungs [22]. A wide range of values of Young's modulus of the lung tissue has been reported in the literature using elastography methods. For instance, using MRI elastography, Goss et al.[23] estimated the value of Young' modulus for human lung to be 1.53 kPa. Using in-vitro elastography, Ebihara et al. estimated the value of Young's modulus to be 10 kPa [24] and Liu et al. reported this value to be 3kPa [25] for fibrotic lungs.

Identification of the mechanical properties of the lung parenchyma is currently limited to the aforementioned methods. It is not possible for these methods to measure the heterogeneity of the lung tissue elasticity in the case of diseased lungs. Considering the heterogeneity of the tissue elasticity is important for modeling the motion of the lung tumor and its surrounding tissues which have significantly different elasticity values. There is clearly a need to develop methods for estimating subject-specific lung-tissue local elasticity. Such a method is used in the current study.

2.3 Constitutive Equations

2.3.1 *Solid Models*

Numerical study of human lung parenchyma requires knowledge of its accurate constitutive equations. There exist quite a number of studies [26-28] which assume lung parenchyma to be a one-phase continuum. These studies have used a generic contact load force or projected displacement on the surface of the lung to model its deformation. In the case of linear material, the Hook's law is the governing equation for the solid model. Nonlinear hyper-elastic material behavior is described by strain energy density function (SEF). Such studies investigate different forms of SEF to define the stress-strain relation in the lung. Table 2-1 shows some of the strain energy density functions which have been used in various studies. The first full form was developed by Lee and Franchus [29] using experimental results obtained by Hoppin et al. [19] to propose a polynomial form of the strain energy function of lung parenchyma. A considerable amount of work has been done by Fung et al. to study the stress-strain relation for soft biological tissue including the lung. A theoretical based formulation was derived for lung in 1974 [30]. Later Fung investigated the material behavior for soft biological tissue [31] and used it to derive the

strain density function in lung parenchyma. A polynomial form of SEF was proposed [32] which was simpler than the formulation of Lee et al [29]. Fung later provided further simplification, for instance, assuming isotropic alveolar structure and even a simpler form of SEF was derived for lung parenchyma [26]. Zeng et al. [33] used the proposed SEF function by Fung et al. [32] and measured the associated mechanical properties of dead human parenchyma in a state of biaxial tension. In another study Gao et al. [18] used the known form of SEF previously investigated by Fung et al. [26] and performed biaxial experiment on cadaver specimens of lung parenchyma to find the accompanying material constants.

In a recent study Rausch et al. [34] have done a comparative analysis of some SEF (foam-like, compressible Neo-Hookean, Ogden, Sussman and Bathe) as well as recombination of their summands. The particular material parameters for each SEF were optimized and the overall best fit was identified for the lung parenchyma tissue which can be used in simulations. The optimal model was established based on uni-axial tension tests on living precision-cut rat lung slices and the nonlinear material parameters of rat lung were determined. An inverse analysis method was used to iteratively estimate the material parameters for the different proposed strain energy functions.

Table 2-1: Strain energy density functions of lung parenchyma proposed in previous studies

Study	Strain energy density function (SEF) and associated material parameters
Fung 1975 [32] Zeng et al. 1987 [33] Eom et al. 2010 [35]	$\rho_0 w = \frac{1}{2} c \exp(a_1 E_{xx}^2 + a_2 E_{yy}^2 + 2a_4 E_{xx} E_{yy})$ $+ \frac{1}{2} c \exp(a_1 E_{xx}^2 + a_2 E_{zz}^2 + 2a_4 E_{xx} E_{zz})$ $+ \frac{1}{2} c \exp(a_1 E_{zz}^2 + a_2 E_{yy}^2 + 2a_4 E_{zz} E_{yy})$ <hr/> $c = 11.8 \frac{g}{cm}, a_1 = 0.43, a_2 = 0.56, a_4 = 0.32$
Fung et al. 1978 [26] Gao et al. 2006 [18]	$\rho_0 w = \frac{C}{2\Delta} \exp(\alpha I_1^2 + \beta I_2)$ <hr/> $\frac{C}{\Delta} = 3.06 \pm 0.84 K. \frac{dyn}{cm^2}, \alpha = 4.47 \pm 1.94, \beta$ $= -4.20 \pm 2.55$
Rausch et al. 2011 [15] (microscopic analysis)	$\psi(C) = \frac{E(1-2\nu)}{4\nu + 4\nu^2} \left(I_3^{-\frac{\nu}{1-2\nu}} - 1 \right) + \frac{E}{4-4\nu} (I_1 - 3)$ <hr/> $E \sim 6.75 \text{ kPa}, \nu = 0.49$
Rausch et al. 2011 [34]	$w_{par} = 4.1 \text{ kPa} (\bar{I}_1 - 3)^2 + 20.7 \text{ kPa} (\bar{I}_1 - 3)^3$ $+ 4.1 \text{ kPa} (-2 \ln J + J^2 - 1)$
E_{xx}, E_{yy}, \dots are strain components and I_1, I_2 and I_3 are invariant of the right Cauchy-Green deformation tensor	

2.3.2 *Two Phase Models*

A number of studies consider the air flow inside the lung and the mechanical couplings between the deformation of the solid tissue skeleton and the airflow. These studies use the laminar fluid force that causes the alveoli to expand during breathing. In principle, the mathematical description of air flow through lung tissue- the governing equations of the airflow dynamics, the mechanics of lung tissue, and the coupling between these motions- is considered. For instance Kowalczyk [36] studied the mechanical behavior of lung parenchyma as a two-phase porous medium. The motion of the fluid phase is assumed to satisfy the Darcy law and the solid phase is considered as a porous nonlinear elastic model. Owen et al. [37] investigated the mechanical behavior of lung tissue under high frequency ventilation by studying the air flow inside the lung. Linearized Navier–Stokes equations were solved for the flow of air, and linear viscoelasticity for the solid tissue. Ilegbusi et al. [38] studied the deformation of the human lung using a fluid-poroelastic model. A flow-structure interaction model was used to simultaneously solve the airflow equations- governed by the Darcy law - and structural dynamics of the lung tissue -governed by the Navier’s equation. Considering the sponge-like nature of the lung enables to account for the anatomic complexity of the lung parenchyma in a computationally cost-effective manner. Thus, in the current study the lung is considered a two-phase poro-elastic medium where fluid and solid domains coexist and share space.

2.4 Biomechanical Modeling of Human Lung

Theoretical models have the ability to allow investigation of complex biological systems and avoid costly experimental studies. Biomechanical modeling of lung deformation is a challenging multidisciplinary task. Efforts to model the respiratory motion started as early as the 1940s [39]. The first modeling of the lung dynamics was presented by Mead et al. [40], studying a model of pulmonary elasticity by considering the lung as a network of nonlinear springs. West and Matthews proposed the first finite element model of the lung in 1972 [41].

The finite element method allows us to define the lung precisely by the geometry and the boundary conditions. In recent years advances in computer and imaging experimental methods have enabled improvement in numerical modeling. Many factors need to be considered for a reliable analysis of lung motion; some of which are listed below:

- Structural complexity,
- Nonlinear elasticity of the lung tissue,
- Geometry complexity,
- Boundary condition and motion of the neighboring organ such as heart [42],
- Subject-specific breathing cycle and lung motion [43].

A large number of biomechanical models have been reported in the literature. These models have tried to address not all but some of the aforementioned issues. Some of these studies are previewed in this section.

2.4.1 Material Models

2.4.1.1 Overview

Lung motion can be analyzed by finite and infinite deformations approaches. The finite deformation analysis is required for large and the infinite deformation is required for small deformations. In infinitesimal deformation analysis a linear relationship between the reference and deformed geometry can be applied and parenchymal properties are linear isotropic and are described by two elastic moduli. In contrast, finite deformation analysis requires a nonlinear stress–strain law and the parenchyma has anisotropic non-linear elastic properties.

Most of soft tissues under loading exhibit nonlinear stress–strain relationship, which involves the application of finite elasticity [44]. However, the linear elasticity has been extensively used for modeling of soft tissues because of its simplicity. In the context of radiotherapy, number of studies have shown that the simple linear material model is sufficient for simulating lung deformation as an alternative to the hyper elastic model. For instance, Liu et al. [45] performed a comprehensive study on 152 lung cancer patients and have showed that during the normal breathing tumors displacement is small and unlikely to exceed 1 cm except for the small regions in the lower lobes of the lungs. In addition, this motion is primarily in the SI direction and is mainly driven by diaphragm motion. A similar behavior has been observed in the study of Al-Mayah et al. [46] on 14 lung cancer patients. The study showed that for a patient that experience the largest diaphragm motion, most of the deformation is concentrated in the lower lobes of the lungs and absorbed fast within a small distance from the diaphragm–lung interface. Therefore it was concluded that even if a large deformation is applied to the lung, most of the lung experiences little deformation

implying that linear isotropic material properties can provide results comparable to nonlinear anisotropic material properties. Besides, Carter et al. [47] showed that constitutive modeling of soft tissues has little effect on the accuracy of deformable image registration. This fact has been confirmed in the study of Al-Mayah et al. [46] by comparing the accuracy of the hyperelastic material properties of the lung to a simple linear elastic model and finding no significant differences between the two models.

Therefore in the current study it is assumed that the lung tissue is linear isotropic elastic. Our results show that this assumption is sufficient for most of the lung except near the diaphragm. It should be noted that the above assumption represents a compromise between complexity and computational cost. Besides, the effect of any error caused by this assumption can be compensated for by the dominant diaphragm pressure.

2.4.1.2 Elastic Models

Various biomechanical models consider the lung as a linearly elastic material defined by the Young's modulus and the Poisson's ratio. In the first finite element model of the lung a 'lung-shaped elastic structure' was modeled by West and Matthews [41], by investigating the behavior of a lung shaped body under its own weight. Due to the lack of data on human lung tissues, the mechanical parameters of dog were measured. In 1977 Sundaram and Feng [48] proposed a finite element model of the human thorax. Linear elastic behavior was considered for the entire thorax including lungs using the same material properties of dog lungs. However, Zeng et al. [33] explored the differences in the material properties of the human and dog lungs, and the fact that human parenchyma is stiffer than dog parenchyma. Owen et al. [37] used linear material for a

study of high-frequency ventilation influence on lung tissue. Brock et al. [49] performed a multi-organ 3D finite element model (FEM) based platform to simulate different organs assuming linear material parameters for each organ including the lungs.

Finally, different values of Poisson's ratio (ν) and Young's modulus (YM) have been applied in various studies. Table 2-2 summarizes the different values used for finite element modeling of the lung. Villard et al. [50] measured the influence and the relevance of these mechanical parameters by numerical simulations using 3D finite element model. The study used three values of Poisson's ratio, 0.25, 0.3 and 0.35 and found that as Poisson's ratio increased, the difference in displacements between the nodes at the surface and the solid body increased.

Table 2-2: Young modulus values and Poison ratio applied in linear finite element model of lungs

Material properties		Source
YM	ν	
~0.04-2.0 kPa	0.3	West and Matthews [41]
1.7 kPa	0.45	Sundaram and Feng [48]
0.25- 1.0 kPa	0.1- 0.4	Werner et al.[51]
5.0 kPa	0.45	Brock et al. [49]
4.0 kPa	0.35	Zhang et al.[27]

2.4.1.3 Heterogeneous Elastic Models

All the aforementioned studies consider lung tissue to be homogenous and the material properties to be the same for the whole lung. However, the material properties are typically not the same for

the whole lung and are spatially dependent especially for diseased and cancerous lungs. From FE point of view each volumetric element in the model has its own specific YM values which are different from other elements. In this case the FE model becomes more complicated. Because of the limitation of the experimental methods only limited numbers of studies have considered the heterogeneity of the lung tissue. Santhanam et al.[22] has proposed the hyper-spherical coordinate transformation method accounting for the heterogeneity of the lung tissue. The lung is divided into voxel points and the material properties for each voxel point are obtained using an inverse method. The method takes as input the subject-specific airflow and lung displacement during the breathing estimated from 4D-CT imaging data coupled with spirometry.

Some finite element modeling studies have utilized the results based on this experimental method [28, 38]. By monitoring different landmarks, the trend of deformation results over the breathing cycle is investigated for the inhomogeneous model and found to be different from the homogenous model. The deformation error is found to decrease by using spatially varying material properties. Min et al. [52] proposed a method linking a varying intensity flow (VF) block-matching algorithm with the FEM for modeling lung deformation. It is shown that using spatially dependent Young's modulus improves registration accuracy compared to the uniform model and is therefore a more proper model of lung deformation.

2.4.1.4 Hyper-Elastic Models

Nonlinear hyper-elastic material behavior is described by strain energy density function. Only a few studies address the issue of finding the material parameters for strain energy density function. A few biomechanical models have been developed based on these experimental studies. For

instance, Zeng et al. [33] used the SEF function proposed by Fung et al. [32] to measure the associated mechanical properties of cadaver in a state of biaxial tension. Later, Eom et al.[35] and Al-Mahya et al. [53] used this hyper-elastic model to create finite element modeling of human lung motion. Al-Mayha et al. used test data presented by Zeng et al. and found the optimum SEF using FE package. The study showed that using hyper-elastic model of material improved the accuracy of predicted lung displacement compared to the elastic model.

As explained in a previous section 2.4.1.1, although hyper-elastic material property may be considered more accurate for modeling the behavior of soft tissues, the non-linear analysis is more complicated and time-consuming than linear-elastic models [46]. Therefore, using elastic property for modeling the breathing motion of lungs is considered more efficient while minimally affecting the accuracy [46].

2.4.2 *Effect of Gravity*

There is considerable physiological and experimental evidence of the effect of gravity on lung dynamics [54-57]. Specifically, it has been shown that regional lung expansion and variation in pleural pressure is largely determined by gravity [58, 59]. Matthews and West [41, 60] developed the first finite element model to study the deformation of the lung due to its weight. A lung-shaped elastic structure was used to explain the regional difference in deformation. The results showed that gravity caused the lung tissue to sag downward and induced a vertical pressure gradient of as much as 0.2 cmH₂O/cm in the lung. This model has been improved in subsequent studies [61-63] and the same results have been confirmed. For instance, Ganesan et al. [58] developed a finite element model of the dog lung, heart and abdomen, consisting of three solid linearly elastic bodies,

to study the effects of gravity on the vertical stress distribution and lung volume at different body positions. The results showed that in all body positions, gravitational forces acting only on the lung contributed a vertical gradient of 0.2 cmH₂O/cm in transpulmonary pressure (P_{tp}). Gravity was observed to cause significant changes in lung volume that were body position-dependent. In particular, gravity caused a reduction in overall lung volume in the supine and head-down body positions, and an expansion in the head-up position.

These initial studies were instrumental in demonstrating the importance of gravity on lung deformation. However, most of the models were based on simplified geometry and computational techniques. Specifically, the “lung shaped structure” used in Matthew and West [41] was modeled as a solid of revolution with circular horizontal cross-section and a 30° vertical segment was used in the analysis. The same geometry was used for the analysis in [62]. The physical model in Liu and Lee [61] was represented by the integral of semi-cylindroids. Ganesan et al. [58] used nine cross-sectional areas of the left lung to construct the finite element model. The number of computational nodes and grids were also quite limited. The total numbers of nodes used in the lung models of Mathew and West [41], Liu and Lee [61], and Ganesan [58] were 41, 86, and 280, respectively. In addition, the studies assumed the material properties of dog due to the limited knowledge on the material behavior of human lungs. However the material properties of human lung are known to be quite different from those of dogs [33]. The results were thus not readily suitable for radiotherapy application. Recent advances in imaging methods and computer aided modeling have enabled the development of more accurate and subject-specific finite element models. However, most of the recent biomechanical models motivated by radiotherapy application

have not considered the effect of gravity [51, 53]. In this study effect of gravity in biomechanical modeling of human lung for radiotherapy application is quantified.

2.4.3 *Boundary Conditions*

Lung inflation is due to forces induced by the respiratory muscles of the diaphragm and rib cages. Lungs are in contact with the chest cavity through the pleura space. The lubricant fluid within the pleura space makes it possible for the lung to slide easily relative to the chest wall and the diaphragm [64]. Some studies have been done to model the contact performance of the lungs. Didier et al. [65] proposed a model based on the rib kinematics. The proposed model consists of ribcage model, diaphragm model and lung model. They deduced the ribcage and diaphragm motion and computed the lung deformation induced by the motion of the ribcage and diaphragm.

Contact-impact analysis (CIA) [28, 66] is one of the methods which have been applied to simulate the interaction between the lung and the surrounding body. In this approach, the surface of the lung at the end inhalation and end expiration phase are obtained from the CT images. The latter surface is used to create the volumetric lung meshes. The lung expands during the inhalation and reaches the target surface at the end of inhalation phase.

In some studies [27, 28, 51] the CIA approach involves applying a pressure, representing the effect of the diaphragm and rib cage contraction, on the lung surface at the expiration phase until the lung expands at its maximal capacity: the inspiration phase. Figure 2-2 illustrates such a modelling approach. In some others [49, 67] the projected displacement boundary condition on the surface of the lung is used instead of the pleural pressure.

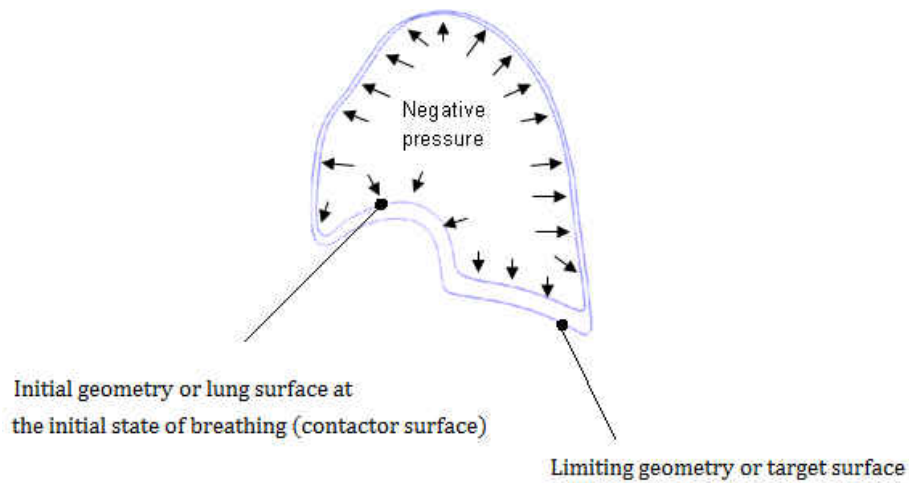


Figure 2-2: Illustration of the contact–impact analysis approach. The lung is expanded starting from the initial geometry and restricted by the limiting geometry. The expansion occurs due to the negative pressure applied to the lung surface.

The CIA method is limited by the fact that it is not able to show the intrafraction variation (patient motion during treatment) and interfraction variation (daily set-up errors) during radiation treatment [68]. As a result the contact-surface approach was introduced to directly simulate the condition of the breathing muscles. Previous studies usually considered ribcage and chest cavity as an elastic body but there is no consensus on the values of the elasticity constants used [53, 69, 70].

Al-Mayah et al. [53] used finite element model to simulate the interaction between the lung and chest wall using frictionless surface-based contact. They used projected displacement boundary condition on the surface of the lung and investigated the effect of contact surface and hyper-elastic

material model on the mechanical behavior of the human lungs. The study shows that the average error decreases from elastic model to the hyper-elastic and reaches its lowest value when contact surfaces and hyper-elastic material properties are combined.

Eom et al. [35] proposed finite element model of the lung by considering the pleural sliding on the inside of the ribcage. They FE models of the lung and associated organs were developed from 4D-CT data. The surface of the lung obtained from CT images at the end of expiration was considered as the inner pleural surface and that at the end of expiration was considered as outer pleural surface. The ribcage was modeled as a homogenous isotropic elastic model while the lung tissue assumed homogenous isotropic hyper-elastic model. A frictionless contact condition assumed between the lung and chest wall. The FEA displacement results were compared using landmarks from the CT data and the average error of less than 3 mm was obtained over multiple breathing phases in the superior-inferior direction.

2.4.4 Accuracy of Biomechanical Models

A number of studies have considered the accuracy of deformation predicted by biomechanical model. Al-Mahya et al. [53] reported the average displacement errors of tumor location in the superior-inferior (SI) direction measured by landmarks to be 7.1 mm for linear elastic model without contact and -0.3 mm for hyper-elastic model with contact. Brock et al. [49] reported an average displacement error of 1.7 mm in the SI direction. Werner et al. [51] predicted the average displacement error between 2 and 7 mm for landmarks at the trachea bifurcation, and between 1.1 mm and 4 mm for landmarks at the tumor location. Eom et al. [35] used a hyper-elastic model to predict average displacement errors of 0.45 cm, 0.387 cm, 0.319 cm, and 0.204 cm at landmark

locations for four different patients. Although the errors reported in these studies could be considered quite reasonable, the models utilized material constants obtained from experiments on animal tissue or cadaver, which are considered inadequate for human radiotherapy. Such an approach severely limits the ability to take into account the patient physiological and pathological conditions. In this study we use the subject-specific material constants derived from real human patients and obtained an accuracy of about 3 mm for the selected landmarks in the lung. This value compares favorably with the desired accuracy of ± 3 mm based on lung radiotherapy application [71].

2.4.5 Efficiency of Biomechanical Models

Both accuracy and efficiency need to be considered, for a biomechanical model-based deformable registration to be clinically useful. Simulation accuracy can be affected by several factors including geometry, material property, and boundary condition. Specifically, it is well-known that most biological soft tissues exhibit nonlinear elastic behavior [44]. Furthermore, the uneven complex geometry of lungs requires computational elements that can adequately represent the complex boundaries. Tetrahedral finite elements are generally considered to be more adequate in this regard than higher-order elements such as hexahedral elements [47, 72].

Al-Mahya et al. [46] assessed the effect of type of elements, linear material properties, and geometry on the modeling of lung motion. It is shown that the 95 percentile of displacement differences between linear and nonlinear analyses range between 0.4 and 0.8 mm. However, the time required for the analyses is increased from 3.4 min in the linear element with linear geometry model, to 95 min in the quadratic elements with nonlinear geometry model. Therefore, linear

tetrahedral elements coupled with linear elastic materials and linear geometry, is superior for modeling the breathing-induced lung motion for radiotherapy applications.

2.5 Integration of Experimental and Simulation Methods

Experimental measurements and numerical analysis are two common methods used to solve engineering problems. Experiments provide a direct way help to obtain the behavior of the actual system but usually the experimental results are scattered and involve errors and uncertainty. On the other hand numerical analysis helps to develop broadly comprehensive information on the computational domain but usually involves approximations. The simulation of biological systems is particularly complicated and typically involves many simulation assumptions due to geometry and structural complexity. In addition, uncertainty in the initial condition and boundary constrains make numerical modeling a challenging task. Due to the limitation of each method the integration of experiment and computational modeling has been offered as a solution to obtain the comprehensive and reliable information on the chosen system. For instance Nisugi et al. [73] proposed a new fusion method called hybrid wind tunnel which fuses the experimental results with the wind tunnel and associated numerical simulation. This new methodology enhances the accuracy of numerical results and provides more detailed behavior of the flow than the experiment. A method to integrate experimental data and computational databases has also been proposed [74]. The method utilizes the sparse experimental data points to calibrate computational database used in flight simulation. In another study, Hayase et al. [75] shows that feedback of the experimental measurement significantly reduces the error due to insufficient grid resolution and decreases the error due to inappropriate model.

In the field of biomechanics the integration of simulated blood flow and Ultrasonic-measurement in the human aorta has been investigated to reduce the error of the calculated flow in order to realize advance accurate diagnosis and treatment [76]. The effectiveness of this integration method has been further investigated [77]. In another study, Schmidt-Richberg et al. [78] introduced decoupled diffusion-based regularization in normal and tangential direction to enable slipping motion at the lung and liver borders. This model enables incorporating of physiological knowledge in image registration thus, improves the registration accuracy significantly.

In the present study, the Tikhonov regularization [7] method is used to integrate image registration and biomechanical modeling results. Tikhonov regularization is a commonly used method in inverse problems. This method previously has been applied to aerospace problems [79-81]. For instance, Wang et al. [80] have used it to fuse the experimental surface pressure and boundary layer profile with the numerical solutions obtained from the computational fluid dynamics (CFD) solver. The study shows that the fused results compare well with the experimental data and as expected, the interpolated results filter out the noise of the experimental data.

CHAPTER 3: PATIENT- SPECIFIC MODEL OF LUNG DEFORMATION USING SPATIALLY DEPENDENT CONSTITUTIVE PARAMETERS

3.1 Introduction

External beam radiotherapy (EBRT) is widely applied to local cancerous tumors. Such a technique is aimed at maximizing dosage to the target tumor while limiting exposure to neighboring healthy organs, thus improving control of tumor growth and limiting side effects [1]. EBRT techniques include computed tomography (CT), magnetic resonance imaging (MRI), single-photon emission tomography (SPET), and photon emission tomography (PET). These methods provide only static snapshots of the patient's anatomy and are thus inadequate for targeting tumor in a moving organ in order to limit exposure to surrounding healthy tissues. This performance limitation has led to the development of image-guided radiotherapy (IGRT) and particularly deformable image registration (DIR).

Although IGRT provides an efficient means of tracking a tumor, it is difficult to control due to the respiratory dynamics. One approach to improve the technique is through integration with bio-mechanical modeling of lung dynamics for direct prediction of lung deformation and tumor motion. This study describes such an approach, involving the rendering of the three-dimensional (3D) lung geometry from 4DCT scans obtained from real patients, and using finite element analysis based on a porous fluid-structure interaction technique. The uniqueness of the study is the use of spatially dependent patient-specific elastic properties in the simulation, and an assessment of the impact of lung heterogeneity on the predicted deformation.

The integration of bio-mechanical modeling to DIR and simulation using the finite element analysis (FEA) has been a subject of recent investigation [49, 67, 82-84]. The FEA allows us to take into account the variation in the material properties, geometry and loading of the moving organ. It also tracks in real time the movement of the lung and the associated tumor. The ease with which accuracy of simulation is controlled might be affected by size, shape, and constitutive properties. Various studies consider the lung as a linearly elastic material defined by the Young's modulus and the Poisson's ratio [27, 51, 85]. Other studies consider the lung as a non-linear hyperelastic material described by strain energy potential law [53]. These studies typically estimate lung elasticity from pressure-volume curves [86] or from in-vitro methods [87]. However, all these approaches ignore the inherent heterogeneity of the lung tissue, a particularly important feature for diseased lungs. In addition, the reproducibility and accuracy of the simulation in these studies could not be ascertained when applied to different patients, since all patients were modeled with the same mechanical properties.

The aim of this study is to simulate the breathing-induced lung deformation based on a 3D finite element lung model utilizing local elastic properties of subject-specific lungs obtained in a previous complementary study [22]. This approach allows us to define the lung as a combination of different volumetric elements each one with its own elastic material properties. The elastic properties were estimated in the previous study from a deformation operator that takes into account the physics of the elastic interaction and the physiology induced by the rib cage and the diaphragm motion. This method provides non-invasive subject-specific volumetric elastic properties and consequently permits a more accurate prediction of lung dynamics for patient radiotherapy. The spatially-dependent lung properties are first processed using an in-house-developed computer

code. The processed properties are then implemented in the finite element model to predict spatially-dependent lung deformation. The results are compared with predictions of lung deformation based on homogenous elastic property in order to assess the impact of heterogeneity on lung deformation.

3.2 Materials and Methods

3.2.1 Principle

Human lung has a complex structure. There are 23 generations of airways in the lung ending up in about 300 million alveoli. The alveoli as well as alveolar ducts and respiratory bronchioles shape the functional part of the lung (lung parenchyma) and fill most of the lung volume. This part also includes a rich network of blood capillaries [61]. On the macro scale lung parenchyma can be modeled as a saturated porous medium with the thin-walled tissue structure as the solid phase and the air in the alveoli and ducts as the fluid phase. Taking into account this sponge-like nature of the lung enables us to model the anatomic complexity of the lung parenchyma in a computationally cost-effective manner. Thus, the human lung is considered here to be a poro-elastic medium where fluid and solid domains coexist within the whole lung volume. The airways are not segmented separately in this study. However, the presence of the large airways and ducts as well as blood vessels in the lung is represented as local inhomogeneity through allowance for the heterogeneous material property in the structural model. The model is implemented by the poro-elastic fluid-structure interaction technique in which the fluid and structural variables are coupled.

3.2.2 Governing Equations

The biomechanical model involves solution of the coupled poro-elastic flow-structure interaction sets of equations within the lung. The microscopic fluid stress is added to the structural model as internal stress and displacement compatibility must be satisfied throughout the porous medium[88].

The pore fluid flows through the porous solid according to the Darcy's law [88], thus:

$$\frac{\mu_f}{\mathbf{K}} \cdot (\mathbf{v} - \mathbf{w}) + \nabla P_f + \rho_f \mathbf{g} = \mathbf{0} \quad (3-1)$$

where \mathbf{K} , μ_f and ρ_f represent the permeability tensor, viscosity and density of air respectively, p_f is the local (pore) pressure, \mathbf{v} is the air velocity vector and \mathbf{w} represents the moving mesh velocity vector. The displacement compatibility indicates that the moving mesh velocity is equal to the solid velocity ($\mathbf{w} = \dot{\mathbf{u}}$) throughout the porous medium. In the solid domain the lung tissue is assumed to be linear isotropic elastic [89, 90]. Note that the isentropic assumption is considered within each element and the Young's modulus varies from one element to another. The solid displacement is obtained by solving for the displacement field, \mathbf{u} , from the Navier's equation:

$$G \nabla^2 \mathbf{u} + \frac{G}{1-2\nu} \nabla(\nabla \cdot \mathbf{u}) = \nabla p_f - \mathbf{b} \quad (3-2)$$

where G and ν are the tissue Shear modulus and Poisson ratio, respectively, and \mathbf{b} is body force.

The Shear modulus is related to the Young's modulus (E) through the relation $G = \frac{E}{2(1+\nu)}$.

Equations (3-1) and (3-2) are solved for the individual, specific patient lung geometry using the ADINA computational code [91] to predict spatial distribution of the lung displacement.

3.2.3 Lung Geometry

Four dimensional (4D)-CT scans of the lung are obtained from specific patients at the UCLA Department of Radiation Oncology, Los Angeles, California. The dataset constitutes a sequence of 3DCT scans representing the volumetric lung anatomy at different air volumes and pressure-volume curves, which closely represents the patient breathing process [22]. The 4DCT scan dataset provides roughly 255 slices of images of the lung. The sets of images at the end-exhalation phase are obtained and processed using the MIMICS software [92] to reconstruct the surface of the lung. The surface is meshed with three-node triangular computational elements. The surface of the lung is used to produce a finite element discretization of the interior of the lung using 3-matic software [93]. Four-node-tetrahedral elements are used for volume discretization. 3-matic software is used to filter out most of the typical errors associated with data transfer from a 3D digitization session. For the right lung a total of 38,298 three-node triangular elements are obtained for the surface and 279,181 four-node tetrahedral elements for the volume. A total of 37,752 surface meshes and 140,164 volume meshes are used in the left lung. Figure 3-1 shows the 3D lung shapes derived from the 4D-CT scans, including the meshes generated.

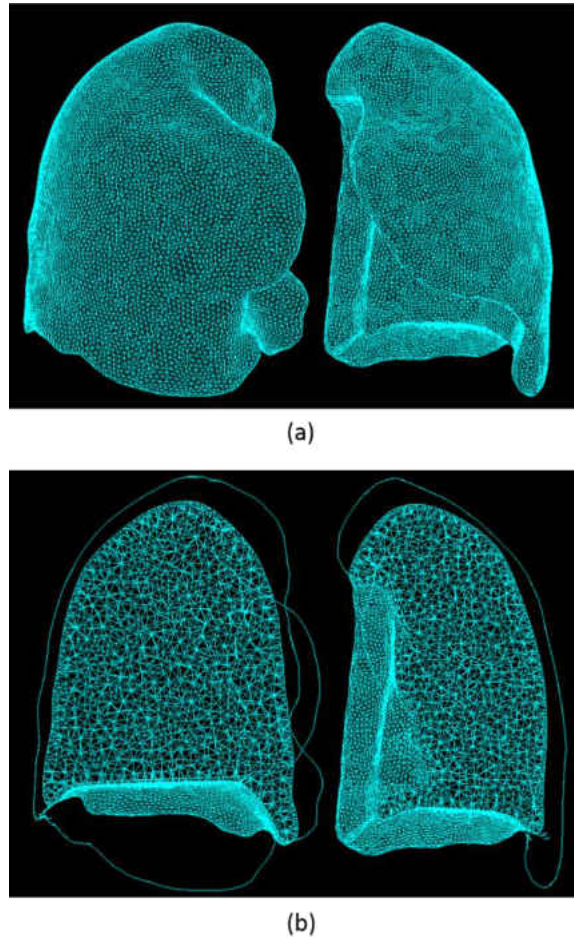


Figure 3-1: Lung shapes derived from 4D-CT scans: (a) a section of the lung surface meshed with shell elements; (b) a section of the solid model meshed with tetrahedral elements

3.2.4 Analysis and Boundary Condition

The lung is assumed to be a porous medium with fluid and solid domains coexisting. Thus, the fluid geometry (which is the same as the solid geometry) is considered to be the whole volume of the lung. Tetrahedral grids are used for discretization of the fluid volume. The meshing process is similar to that described for the solid domain in a previous Section 3.2.3. The inlet is assumed to

be at the hilum where the airway enters the lung. The exact location of the hilum is determined by the intersection of the trachea with the lung. Figure 3-2 illustrates the location of the inlet of the lung and the periodic pressure prescribed over one breathing cycle at the inlet. The amplitude of the pressure is prescribed based on results of spirometry study at UCLA Department of Radiation Oncology. The inlet pressure is assumed to reach its maximum value at the end of the inhalation phase ($t=2$ sec). The flow is assumed unsteady and laminar. The fluid is assumed to be Newtonian and incompressible with density and viscosity being $\rho_f = 1.205 \text{ kgm}^{-3}$ and $\mu_f = 1.83 \times 10^{-5} \text{ kgm}^{-1}\text{s}^{-1}$ respectively.

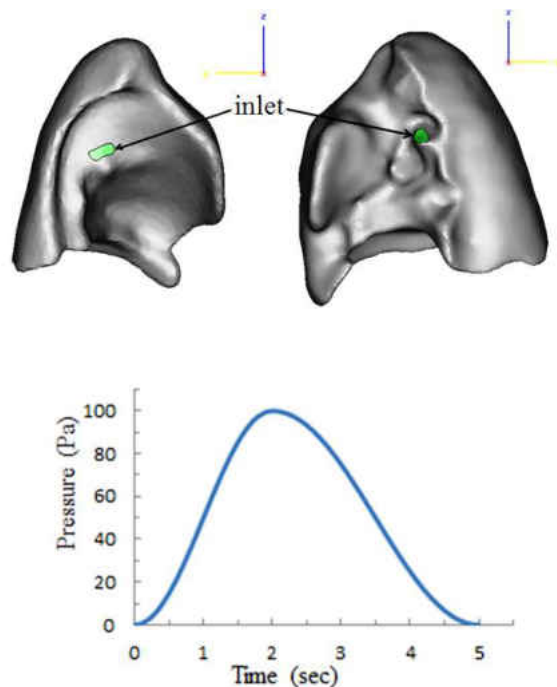
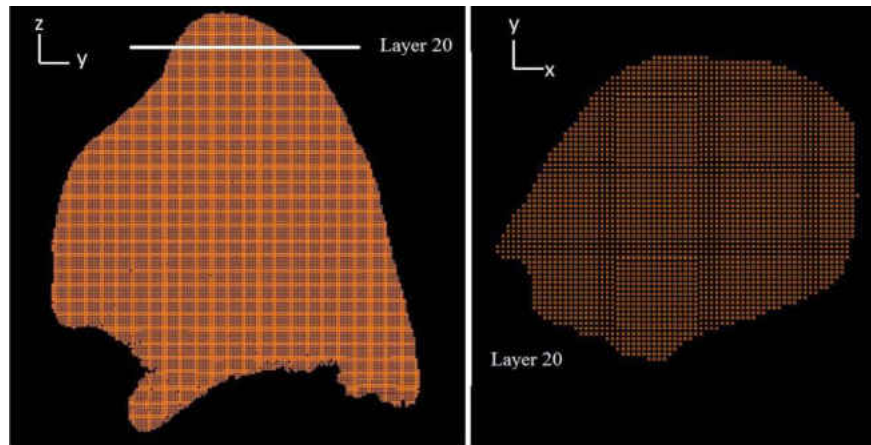


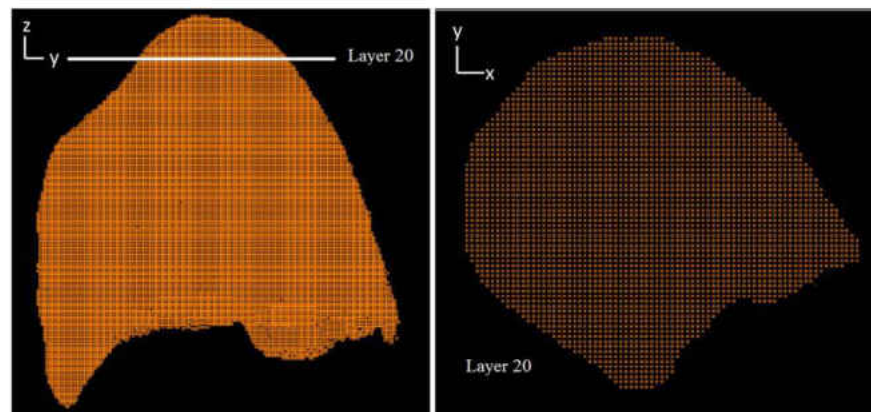
Figure 3-2: Prescribed inlet pressure profile, pressure condition is imposed at inlet locations of the fluid mesh

3.2.5 Material Properties

The Finite Element Method allows us to define precisely the lung by the geometry and the boundary conditions. However, a major requirement for accurate prediction of lung deformation is a reliable estimate of the lung elastic properties. In this study we used local elastic properties of the subject-specific lung obtained in a complementary study [94]. The study developed an inverse non-invasive methodology to estimate the elastic properties of 3D volumetric lung. The method takes as input the subject-specific airflow and lung displacement during the breathing estimated from 4DCT imaging data coupled with spirometry. Basically, the lung is decomposed into voxel points and a correlation is defined to estimate the deformation operator of each voxel point for known values of the applied force and the displacement during the breathing. Each voxel point is then associated with a single Young's modulus (E) and a common Poisson's ratio of 0.35 [94]. Figure 3-3 shows the repartitioning of the 3D lobe shape into layers and the voxel points that populate those layers. The estimated values of the deformation operator and consequently the elastic properties are specific to the human subject. The result of the inverse methodology indicates that the estimated Young's modulus of each voxel is within a 2% error level. The maximum Young's modulus obtained for a single voxel point at the bottom part of the lobe is 4.03 kPa for the left lung, and 4.05 kPa for the right lung. The minimum value obtained at the top is 0.01 kPa for both lungs. These values fall within the range of values used in other studies [50, 51].



(a)



(b)

Figure 3-3: Schematic of repartitioning of the voxel points to match the 3D lung geometry derived from 4DCT scans used in simulation (a) front view (b) top view. Each element used in the computation is associated with the closest voxel point.

3.2.6 Implementation

A software code was developed in-house to properly introduce the elastic properties in the finite element model. The code uses as input model geometries from a NASTRAN file and the elastic property data (voxel points) from a text file. The transformation matrix between the image coordinates of YM values and the coordinates of model geometry is used to align the coordinates between the two files. Having the same coordinates for each tetrahedral element in the FE model the material property corresponding to the closest voxel point is assigned. The software generates a NASTRAN file recomposed with material properties assigned for each tetrahedral element. The implementation process is illustrated in Figure 3-4.

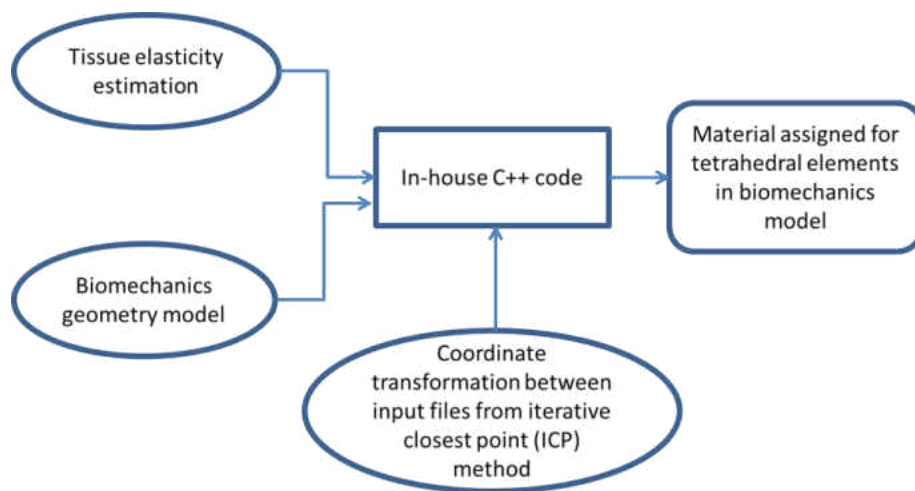


Figure 3-4: Schematic illustrating implementation of patient-specific elastic property data.

3.3 Results and Discussion

Figure 3-5 (a) shows the predicted map of the magnitude of displacement (in mm) at the end of inspiration. The maximum and minimum displacements are presented for both the right and left lungs with variations between the two extremes. In order to facilitate visualization of the displacement profile, cut-out views of the specific slices in the transverse and coronal planes are also presented in Figure 3-5 (a). The Figure shows that the magnitude of displacement generally increases from the interior to the outer surface and from the top to the bottom of the lung. This trend is consistent with the distribution of the intrapleural pressure that originates from the ribcage and diaphragm and gradually attenuates towards the top and interior parts of the lobe. However, in the SI vertical direction the variation of the displacement is highest at the top and bottom and smallest in the middle part of the lung.

Figure 3-5(b) shows the predicted displacement for the model based on spatially constant Young's modulus (YM) for comparison purpose. The YM is set to be the average of the values for the whole lung (~ 0.8 kPa). The two sets of results in Figure 3-5 (a) and Figure 3-5(b) are qualitatively similar, with the highest lung displacement occurring at the bottom of the lung and near the ribcage while the lowest deformation is at the top and interior part of the lung. However, there is a significant quantitative difference in the results between the two models. The magnitude of displacement is observed to be smaller in the homogenous model. Specifically the maximum magnitude of displacement is 10 mm for the homogenous model and 28 mm in the heterogeneous model. In addition, there is a significant difference in the displacement pattern between the two models. The results in Figure 3-5(a) and Figure 3-5(b) clearly illustrate the role of tissue structure

and its associated material property in transmitting the intrapleural pressure to lung. Such results could be utilized within the deformable image registration process for accurate prediction of tumor motion throughout the breathing cycle.

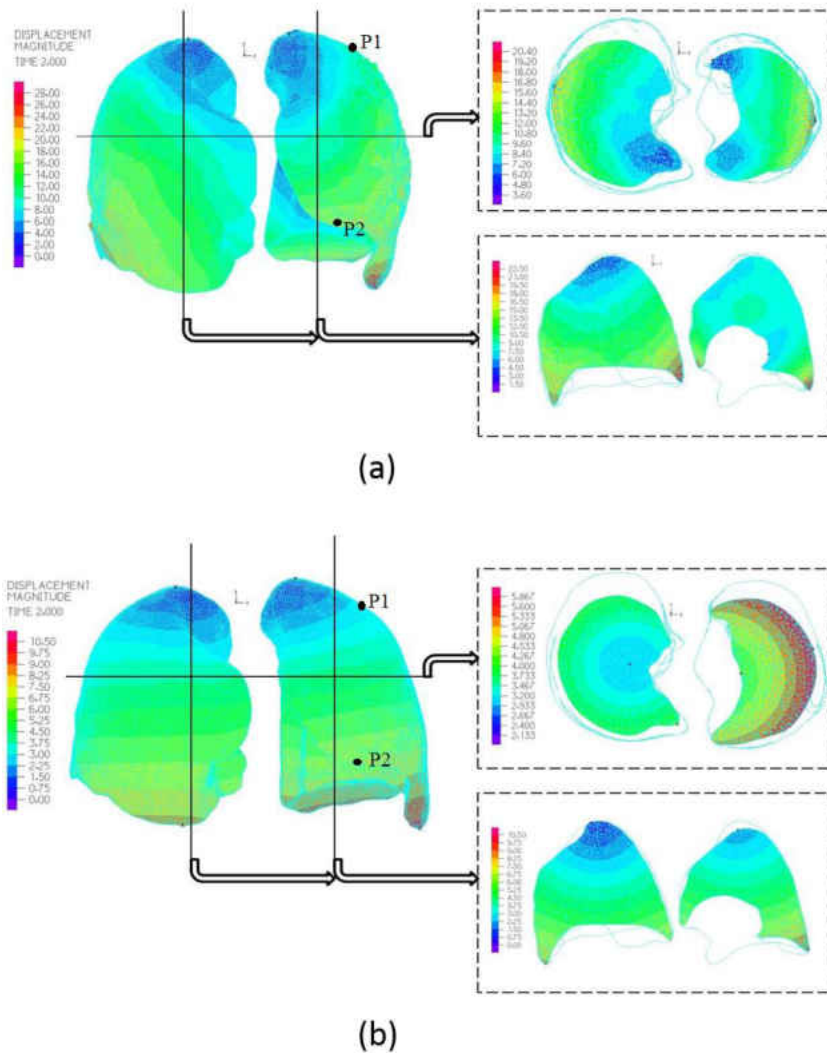
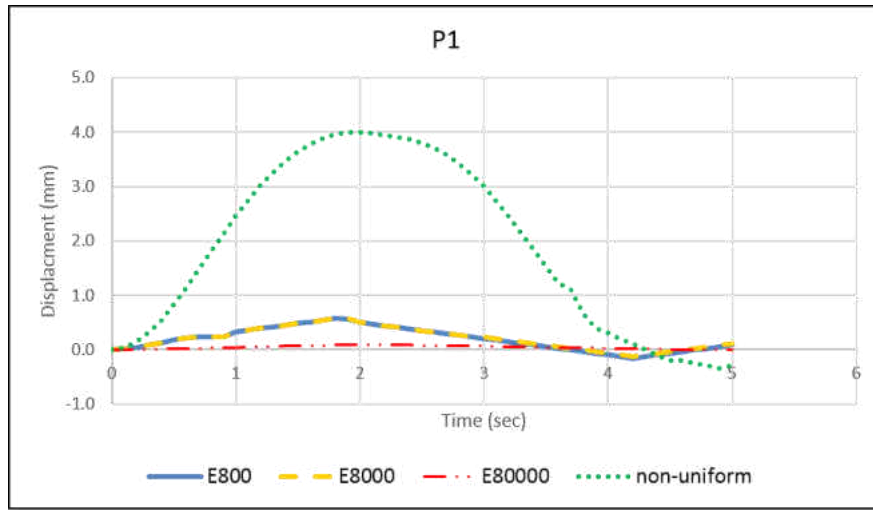
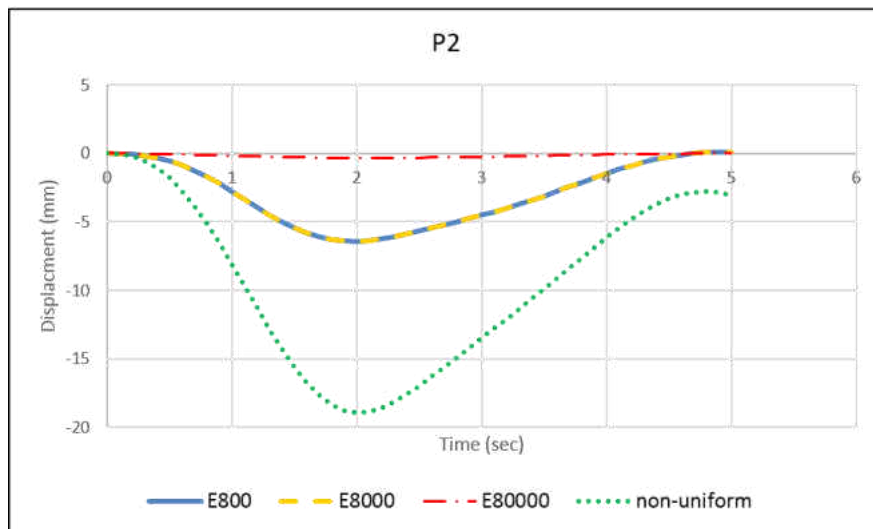


Figure 3-5: Predicted amplitude map of displacement magnitude in (mm) at the end of inhalation: (a) heterogeneous model, (b) homogenous model

The effect of material properties of the lungs can be further quantified by monitoring deformation at specific landmarks or locations on the lobe over time. Figure 3-6 shows the predicted displacements monitored in the SI direction at two nodes P1 and P2 (in Figure 3-5), located at the top and the bottom of the lobe, respectively. The four cases considered are one non-uniform elastic property, and three uniform properties with Young moduli of 80,000 Pa, 8000 Pa and 800 Pa. The computations cover a duration of one breathing cycle. The predicted deformations at P2 (near the bottom of the lobe) are larger than those at P1 (top of the lobe) in all cases. There is no discernible difference in the predicted deformation at P1 and P2 between the two uniform elastic cases with Young moduli of 8000 and 800 Pa in spite of the large difference in the values of the elastic modulus. However, increasing the YM to 80,000 dramatically decrease the displacement and lung is almost static. The effect of heterogeneity is significant at both landmarks, showing a distinct difference in both the magnitude and trend of the predicted deformation between the models with uniform and non-uniform elastic property. Specifically, while the heterogeneous model exhibits a sinusoidal pattern mirroring the breathing pattern (Figure 3-6), the uniform model gradually approaches a smaller peak value. These results clearly underscore the significance of lung non-homogeneity and the fact that lung deformation cannot be adequately represented with the conventional single-value uniform models.



(a)



(b)

Figure 3-6: Displacements of nodes (a) P1 and (b) P2 in the vertical (SI) direction at end inhalation (dotted lines represent the spatially-dependent material model, dashed lines represent the linear model with $E = 80,000$ Pa and 8000 and solid lines represent the linear model with $E = 800$ Pa).

3.4 Summary

The effect of using subject-specific heterogeneous lung elasticity for modeling breathing-induced deformation during radiotherapy has been investigated. The lung was modeled as a heterogeneous poroelastic medium. The lung geometry at the end-expiration was reconstructed from 4DCT dataset of one patient.

The subject-specific tissue elasticity was obtained using an inverse deformation analysis. The airflow-tissue interaction model involved solving the coupled equations governing fluid dynamics of airflow inside the lungs and the associated structural deformation of the lung, subject to appropriate boundary conditions.

The major findings of the study can be summarized thus:

- Patient-specific elastic properties can be readily implemented in the finite element model.
- Predicted lung deformation is significantly larger close to the diaphragm.
- The local heterogeneity in the elasticity of the lung substructures has a significant impact on the displacement inside lungs.

The above findings have profound implication in the optimization and targeting of radiation to tumor in radiotherapy. The presence of tumor (focal or distributed) in the lung substructures significantly affects the resulting spatiotemporal displacement and deformation of the lung. The model presented here has demonstrated the capacity to fully represent and quantify such detailed motion of any location in the lung utilizing subject-specific tissue elasticity for lung substructures. Validating the deformation inside the lungs and the subsequent interaction studies will be discussed in chapter 5 of this dissertation.

CHAPTER 4: MODELING AND VALIDATION OF HUMAN LUNG DEFORMATION

4.1 Introduction

Accurate prediction of respiratory lung deformation is crucial for tumor localization and targeted radiotherapy in patients with lung cancer [95]. Image-based methods have been used extensively for quantification of such lung motion. However, imaging methods do not account for the physiological properties of the lung. Biomechanical models have recently become popular for representation of lung motion. These models often rely on simplified property data derived from animal studies. In addition, the accuracy of such models have not been systematically assessed. The present study applies a biomechanical model utilizing human subject-specific lung properties and assess model accuracy by comparison of prediction with those derived from image registration.

The spatio-temporal lung deformation is predicted in patients with lung cancer undergoing radiation therapy. The simulation is performed on three-dimensional (3D) lung geometries reconstructed from 4DCT scan dataset of two human patients. The numerical simulation utilizes a porous flow-structure interaction technique to simultaneously solve the coupled airflow equations and structural dynamics of the lung tissue.

Four-dimensional computed tomography (4DCT) registration and dynamic magnetic resonance imaging has been widely used for identification of the lung and tumor movements [5, 96]. Although imaged-based methods provide direct means to obtain the displacement, they are limited

by the lack of breathing physiology and physical properties of the lung. Biomechanical modeling that enables simulation of physics and physiology-based lung deformation has therefore been generating interest of recent.

Biomechanical modeling to predict lung deformation has been studied extensively to complement imaging [97, 98]. Numerical modeling of lung deformation is however challenging due to structural complexity, heterogeneity of lung parenchyma, boundary conditions and subject-specific breathing pattern [99]. A number of studies have considered the lung as linearly elastic [85, 100] and nonlinear hyper-elastic [101, 102], with the lung generally considered as a one-phase continuum [103, 104].

In spite of the growing number of studies on the dynamics of human lung, a systematic comparison of imaging and computational methods has not been undertaken. This deficiency is addressed in this chapter through direct validation of predicted lung deformation using the results of image registration. The biomechanical model uses the geometry and spatially-dependent elastic properties obtained for two specific patients.

4.2 Materials and Methods

This section describes the method used to estimate lung deformation from integration of image registration and numerical simulation using finite element model. A schematic of the integrated approach is presented in Figure 4-1.

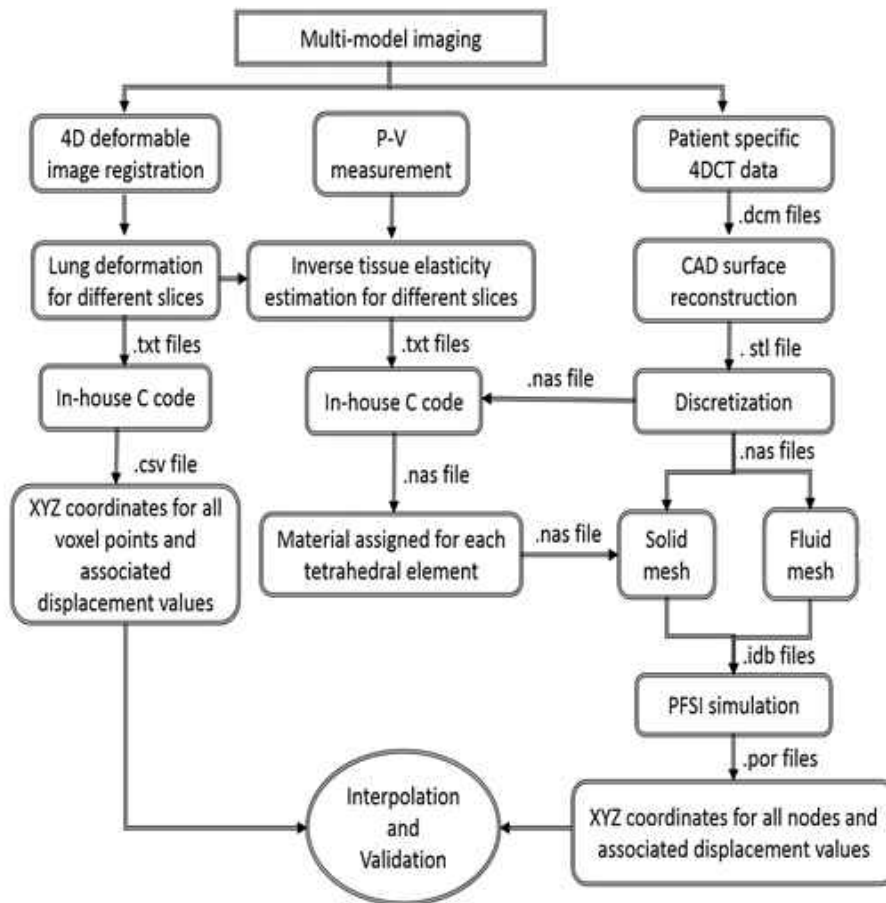


Figure 4-1: Processing pipeline diagram illustrating various steps involved in the determination of the image-based and model-based displacements

4.2.1 Image Registration

The 4DCT scans used were acquired from in vivo experiments on two human male adult patients at different stages of the breathing cycle. The 4DCT datasets at 10% tidal volume intervals were acquired using Siemens Biograph strain-gauge 64 slices CT. The 3D volumetric lung were

segmented using Pinnacle MBS and OSIRIX software. A 4DCT data registration algorithm was used to estimate the motion of each 3D voxel at end-expiration 3D volume data by searching for and locating a corresponding voxel in another 3D volume at a different breathing phase.

An optical flow-based motion estimation method was used for the registration [105]. The method is based on local Taylor series approximation. One of the limitations of the method as applied to estimating 3D organ motion is the low sensitivity to variations in regional motion. To improve accuracy, a multi-level, multi-resolution method [4] was used, which computed optical flow between two 3D volumes at lower resolution, propagated the result to the higher resolution volume, and subsequently to the original resolution volume data. In this approach, the organ anatomy was divided into four parts: (i) lung outline, (ii) large capillaries, (iii) small capillaries, and (iv) parenchyma region. At each level of anatomy, a multilevel, multi-resolution optical flow registration was used for computing the 4D organ motion of that anatomy and integrated into the next level. The 4DCT images had no visible artifacts as they were acquired using a well calibrated 5D imaging protocol [106]. The images had slice increment of 1.0 mm in the superior-inferior (SI) direction.

4.2.2 Biomechanical Modeling

4.2.2.1 Overview

Human lung has a complex structure. On the macro scale the lung parenchyma can be modeled as a saturated porous medium with the thin-walled tissue structure as the solid phase and air in the alveoli and ducts as the fluid phase. Considering this sponge-like nature enables us to model the anatomic complexity of the lung parenchyma in a computationally cost-effective manner. Thus,

the lung is considered a poro-elastic medium where fluid and solid domains coexist and share space. Although the airways are not segmented separately the presence of large airways and ducts as well as blood vessels is represented as local inhomogeneity.

4.2.2.2 Solid Structure

An inverse non-invasive methodology is used to estimate the elastic properties of the 3D volumetric lung [22]. Basically, the lung is decomposed into voxel points and a correlation is defined to estimate the deformation operator of each voxel point for known values of the applied force and the displacement during breathing. The values of airflow and volumetric displacement are used as input to estimate the deformation operator in terms of Green's function (GF). A heterogeneous GF based formulation is considered for both the surface and volumetric deformation. The structural and functional constants estimated for the surface lung dynamics are also used for the volumetric dynamics. The GF for the volumetric lung is reformulated in the spectral domain using Hyper-Spherical Harmonic (HSH) transformation, which is the 3D extension of Spherical Harmonic (SH). Upon simplification, the HSH coefficients of the displacement (d) are represented as a product of the HSH coefficients of the applied force and the deformation operator thus:

$$d_{\lambda_1 l_1 m_1 \lambda_2 l_2 m_2} = \left(\frac{8\pi^2}{2\lambda_1 + 1} \right) f_{\lambda_1 l_1 m_1} \gamma_{\lambda_2 l_2 m_2} \quad (4-1)$$

where $\gamma_{\lambda_2 l_2 m_2}$ and $f_{\lambda_1 l_1 m_1}$ represent the value of displacement and applied force respectively, which are represented by their HSH coefficients. The deformation operator can be estimated from

Equation (4-1) in terms of their spherical harmonic coefficients. The term $\frac{8\pi^2}{2\lambda_1+1}$ refers to the normalization factor of the SO(3) rotation group.

The applied force is computed using pulmonary function test [107] which provides the pressure corresponding to the various lung volumes during breathing. The volumetric lung displacement is estimated using 4DCT registration as described in Section 4.2.1. Each voxel point is then associated with a single Young's modulus and a common Poisson's ratio of 0.35. The average values of Young's modulus obtained for the two patients used for this study were 1 kPa (Patient 1) and 5 kPa (Patient 2). Figure 4-2 illustrates the 3D volume-rendering representation of the Young's modulus obtained for the two patients.

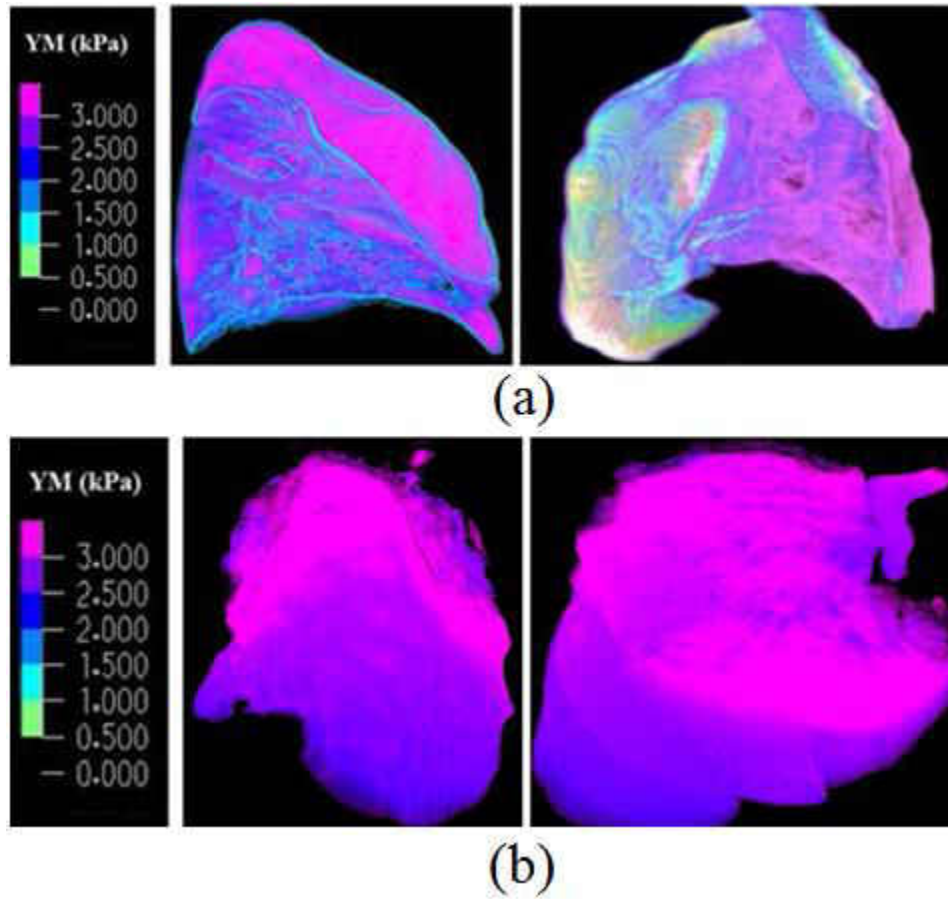


Figure 4-2: Three-dimensional volume rendering of the Young's modulus values for (a) Patient 1
 (b) Patient 2

4.2.2.3 Fluid Domain

The lung airway is like a multilevel branching tree. Based on this airway structure of the lung, the permeability ($k = \frac{\phi R^2}{8}$, in which R is the branch radius) should decrease significantly from the main central branches to the tip branches as the branch diameter progressively decreases [38]. Correspondingly, the airflow velocity in the primary central branches is significantly higher than

that in the peripheral branches. For accurate estimation of airflow a multibranching lung structure is required that permits application of different permeability values. However Preliminary studies [38] indicated that the deformation is little affected by the permeability. Therefore we used a constant permeability of 10^{-5} m^2 for the whole lung in this study [37, 108].

The value of porosity used for the study is 0.99 [37, 108]. The flow is assumed unsteady and laminar. The fluid is assumed to be Newtonian and incompressible with density $\rho_f = 1.205 \text{ kgm}^{-3}$ and viscosity $\mu_f = 1.83 \times 10^{-5} \text{ kgm}^{-1}\text{s}^{-1}$.

4.2.2.4 Porous Fluid-Structure Interaction

The Arbitrary Lagrange-Euler (ALE) formulation is applied to the fluid domain since it is deformable. The pore fluid flows through the porous solid structure according to the Darcy's law [88], thus:

$$\frac{\mu_f}{\mathbf{k}} \cdot (\mathbf{v} - \mathbf{w}) + \nabla P_f + \rho_f \mathbf{g} = \mathbf{0} \quad (4-2)$$

where \mathbf{k} , μ_f and ρ_f represent the permeability tensor, viscosity and density of air respectively, \mathbf{v} is the air velocity vector, \mathbf{w} is the moving mesh velocity vector, P_f is the pore pressure and \mathbf{g} is the gravity vector. In this study the 4DCT scans are acquired when the patient lies in the supine body position during radiotherapy. Therefore our calculation assumes this supine body position and gravity is applied in the posterior direction. In the coupled porous media, the porosity and permeability are defined as [88]:

$$\emptyset = 1 - \frac{J^0}{J} (1 - \emptyset^0) \quad (4-3)$$

$$\mathbf{k} = \frac{\phi}{\phi_0} \mathbf{k}_0 \quad (4-4)$$

where J is the geometric element Jacobian and the superscript “0” indicates the quantities at initial reference configuration. In the current model the reference state is considered to be at the end of exhalation when the lung is at rest.

A Lagrangian formulation is used for the solid domain. The lung tissue is assumed to be linear elastic and isotropic [11]. Note that isotropic assumption is considered only at the elemental level and the Young’s modulus is allowed to change from one element to another. Allowance is made for geometric nonlinearities by assuming the deformation to be large. Fluid and structural variables are coupled in the whole porous medium through displacement and traction conditions [88]. The microscopic fluid stress is added to the structural model as an internal stress. The stresses in the porous medium are thus expressed as:

$$\boldsymbol{\sigma}_s^t = \boldsymbol{\sigma}_s - P_f \mathbf{I} \quad (4-5)$$

where P_f and $\boldsymbol{\sigma}_s$ represent respectively the pressure of the pore fluid and Cauchy stress tensors of the skeleton, $\boldsymbol{\sigma}_s^t$ is the total Cauchy stress in the solid model and \mathbf{I} is the identity matrix.

The total Cauchy stress tensor in the solid model is transformed to the second Piola-Kirchhoff.

The governing equation for the total stress in the solid model is the momentum equation given by:

$$\rho_s \frac{D^2(\mathbf{u}_s)}{Dt^2} = \nabla \cdot (\mathbf{F} \cdot \mathbf{S}_s^t) + \rho_s \mathbf{b} \quad (4-6)$$

where \mathbf{u}_s represents the displacement vector in the solid domain and ρ_s represents the density of the tissue. $\mathbf{F} = \mathbf{I} - \nabla_0 \mathbf{u}$ is the deformation gradient tensor, \mathbf{S}_s^t is the total second Piola-Kirchhoff

stress tensor in the porous medium and \mathbf{b} is body force. Displacement is interpreted to be an estimate of the lung motion field during breathing, from end of expiration to end of inhalation. The compatibility of displacement/velocity must be satisfied in the whole porous medium, thus;

$$\mathbf{u}_s = \mathbf{u}_f \quad (x, y, z) \in \Omega_p \quad (4-7)$$

where \mathbf{u}_f is the fluid displacement and Ω_p represents the porous domain. This condition also ensures that the moving mesh velocity in a previous Equation (4-2) is identical to the solid velocity ($\mathbf{w} = \mathbf{u}_s$) in the porous medium. The above equations are solved in ADINA [109] commercial code subject to the boundary conditions described below.

4.2.2.5 Boundary Conditions

Normal respiration involves a process often termed negative pressure breathing. During each breath changes in the intrapleural pressure acts upon the lung surface and establishes a sub-ambient pressure within the lungs. The pressure applied on lung for a given change in volume is computed using the pressure-volume curve measurement [107]. Here, periodic pressure boundary condition is assumed on the lung surface over the breathing cycle as shown in Figure 4-3. In a normal breathing process, air flow is generated by the pressure applied to the tissue. Thus, for realistic simulation of breathing mechanics a stress-free boundary condition is specified at the flow inlet to the lung assumed to be at the hilum. The lung is anchored both at the top and at hilum to be consistent with the imaging experimental results.

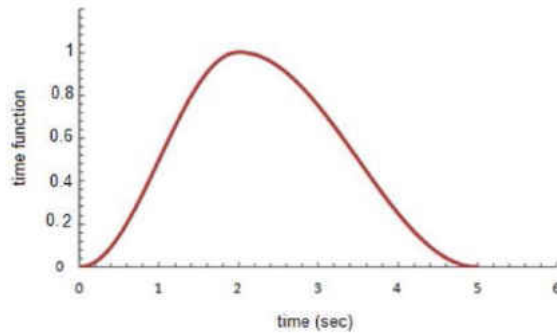


Figure 4-3: Prescribed boundary pressure profile

4.3 Computational Details

The 3D lung geometry is first reconstructed from the 4DCT dataset of patients using the Mimics commercial code [110] and used to construct the computational grid by means of 3-matic commercial code [93]. A 4-node tetrahedral and a 3-node triangular element are used respectively for volume and surface discretization. Both solid and the fluid geometries are comprised of the whole volume of the lung and are similarly meshed.

The fluid and the solid equations are solved by the iterative two-way coupling or partitioned method embodied in ADINA computational code [110]. In this approach, the fluid and solid equations are solved independently in sequence, using the most recent information from another part of the coupled system. This iteration is continued until convergence is reached in the solution of the coupled equations. A mesh-independence study is performed to ensure numerical accuracy. The final meshes chosen from the mesh-independence test and used for the computations are summarized in Table 4-1.

Table 4-1: Number of computational elements and nodes used in the biomechanical model

		Volume elements	Surface elements	Nodes
Patient 1	Right lung	303,933	34,314	43,608
	Left lung	290,164	37,752	42,305
Patient 2	Right lung	327,736	39,836	46,459
	Left lung	308,218	53,486	47,626

4.4 Results

Figure 4-4 (a) and Figure 4-4 (b) show the predicted map of the absolute displacement (in mm) at the end of inspiration for Patients 1 and 2, respectively. The maximum and minimum displacements are shown with variations between the two extremes. The figures show that the absolute displacement generally increases from the interior to the outer surface and from the top to the bottom of the lung. This trend is consistent with the distribution of the intrapleural pressure that originates from the ribcage and diaphragm and gradually attenuates towards the top and interior parts of the lobe. However, the local displacement pattern depends on the shape of the lung and the distribution of the elastic properties. In addition, Patient 1 has a larger absolute displacement than Patient 2 due primarily to the difference in breathing pattern and Young's modulus. Specifically, the maximum pressure boundary condition is 100 Pa for Patient 1 and 40 Pa for Patient 2 with the corresponding average Young's modulus of 1 kPa and 5 kPa, respectively.

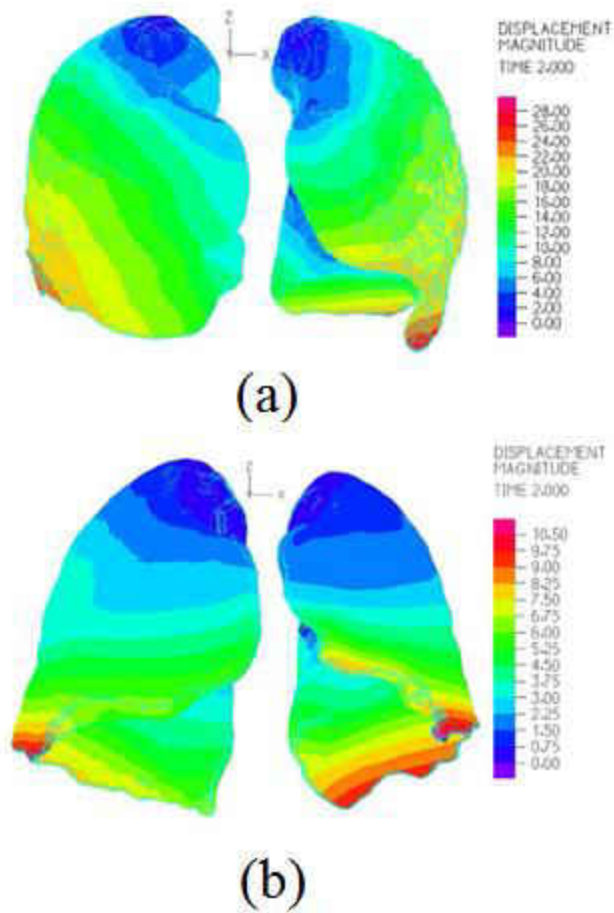
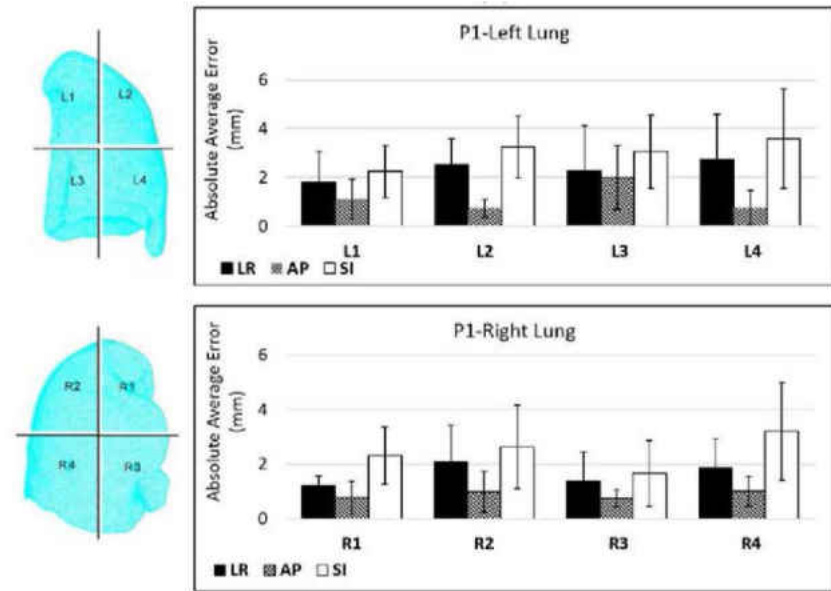


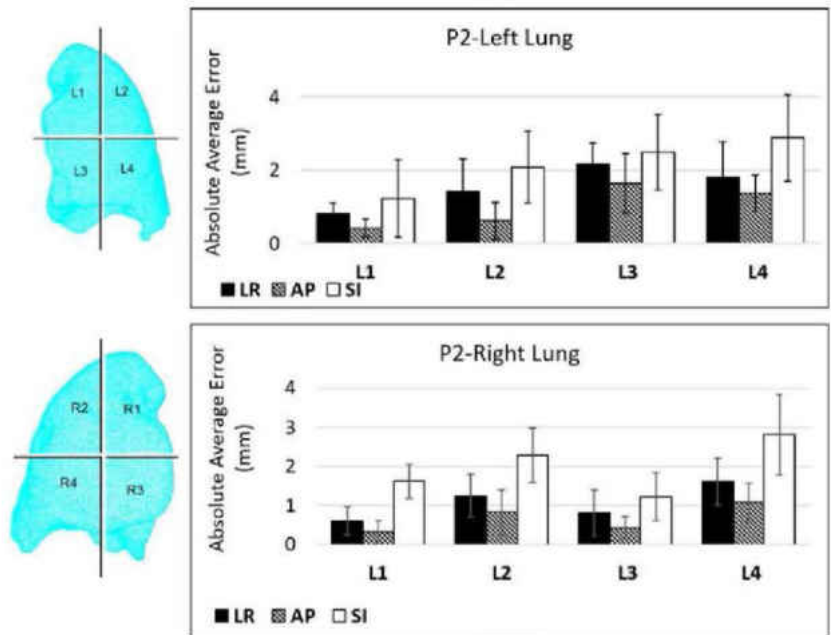
Figure 4-4: Predicted amplitude map of displacement magnitude in (mm) at the end of inhalation for (a) Patient 1 (b) Patient 2

In order to check the accuracy of the model, the left and right lungs of each patient are divided into four regions at the midpoint in the superior–inferior (SI) and left–right (LR) directions as shown in Figure 4-5. Fifty landmarks are selected in each region and the absolute average error and standard deviation in the LR, anterior–posterior (AP), and SI directions are plotted for each region as shown in Figure 4-5. The predicted error typically ranges from 0.73 mm to 3.6 mm in the left lung and

0.72 mm to 3.2 mm in the right lung for Patient 1. The corresponding values for Patient 2 are 0.41 mm to 2.9 for left lung and 0.32 mm to 2.8 mm for right lung. The displacement error is generally larger in the outer region (near ribcage) than the inner regions of the lungs. This result indicates that representation of the contact between the lung and chest wall will need further improvement in future study. The predicted displacement at the bottom-interior parts of the right lungs (R3) are more accurate than the bottom-interior parts of the left lungs (L3). The accuracy of the results are clearly affected in the regions near the heart as the amplitude of lung displacement induced by cardiac motion has not been considered in the present model. Although it is desirable to improve the underlying assumptions of the model, it is noteworthy that the predicted average error over most of the lung is within 3mm which is considered clinically acceptable [111].



(a)



(b)

Figure 4-5: Average absolute error and standard deviation for four regions of the left and right lungs for (a) Patient 1 (b) Patient 2

In order to compare the accuracy of the heterogeneous and homogeneous models, 50 landmarks are selected at the bifurcation of the airway where the effect of heterogeneity of the lung tissue is expected to be significant. The average YM values are used for the reference cases utilizing homogenous property. Table 4-2 summarizes the mean absolute errors and the standard deviation of the selected landmarks in the AP, LR, and SI directions for each patient. The errors are significantly lower with the heterogeneous than the homogeneous model in all cases. In particular, the reduction in the SI direction ranges from 3.2 mm to 1.03 mm for Patient 1, and 1.8 mm to 0.78 mm for Patient 2.

Table 4-2: Average absolute error of homogenous and heterogeneous models for landmarks at the bifurcation of airway

		Absolute mean error (mm)		
		AP	LR	SI
Homogenous	Patient 1	1.21 ± 0.3	2.14 ± 0.42	3.2 ± 0.5
	Patient 2	0.75 ± 0.2	1.11 ± 0.4	1.8 ± 0.66
Heterogeneous	Patient 1	0.82 ± 0.15	0.94 ± 0.32	1.03 ± 0.41
	Patient 2	0.34 ± 0.04	0.51 ± 0.2	0.78 ± 0.08

The transient displacement of 18 selected landmark locations in the lung are also monitored and compared for both the biomechanical model and image registration data. The location of the selected landmarks as well as their transient displacement profiles over the inhalation phase are plotted in the Figure 4-6 and Figure 4-7. The landmarks were selected in the periphery of the lung

(one near the ribcage and the other near the interior surface), and the third in the core region. The results obtained from the two methods are generally in good agreement.

Figure 4-6 (a) shows that the FE result is favorably matched with the imaging results at locations P1 and P2. However the discrepancy is larger for P3 which is located near the ribcage.

In Figure 4-6(b), landmark P6 which is located near the ribcage exhibits the largest discrepancy between the two sets of results, similar to location P3 in Figure 6a. However, P4 which is located near the heart on the interior surface of the lung has larger discrepancy than its corresponding node, P1 in Figure 4-6(a).

The absolute displacements for the landmarks at the bottom as presented in Figure 6c are generally higher than those in previous Figures 6a and 6b located at the top and the middle of the lung. In Figure 4-6(c), again the largest discrepancy is observed for the monitored locations near the heart (P7) and ribcage (P9).

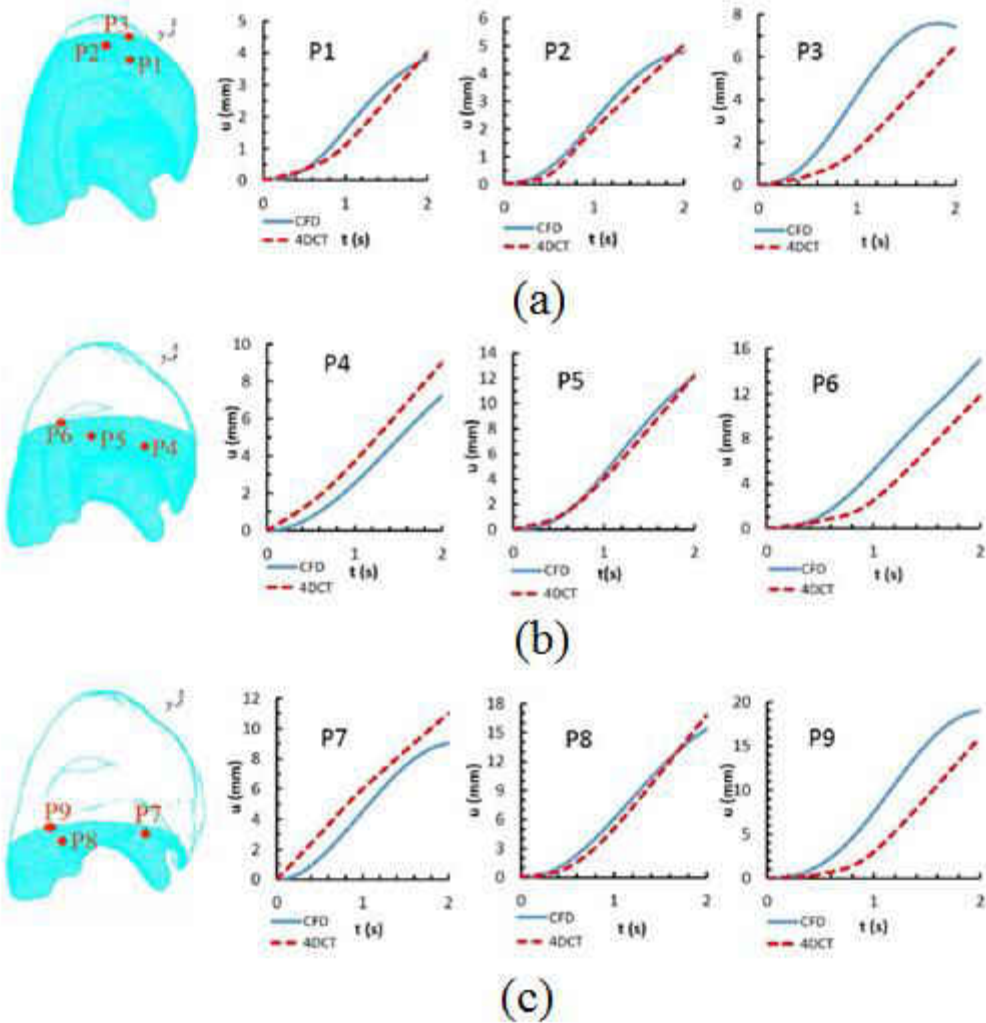


Figure 4-6: Comparison of prediction displacement for monitored landmarks located at the (a) top (b) middle and (c) bottom of the left lung over the inhalation phase

The transient displacement profiles for the landmarks in the right lung are shown in Figure 4-7(a-c), at the top, middle, and bottom of the lung, respectively. The trends of displacement profiles are generally similar to those already presented above for the left lung. Specifically, the absolute

displacement increases from top to bottom. The locations near the rib cage also exhibit similar behavior to those observed in the left lung, with larger errors at these locations than the interior surface and core of the lung.

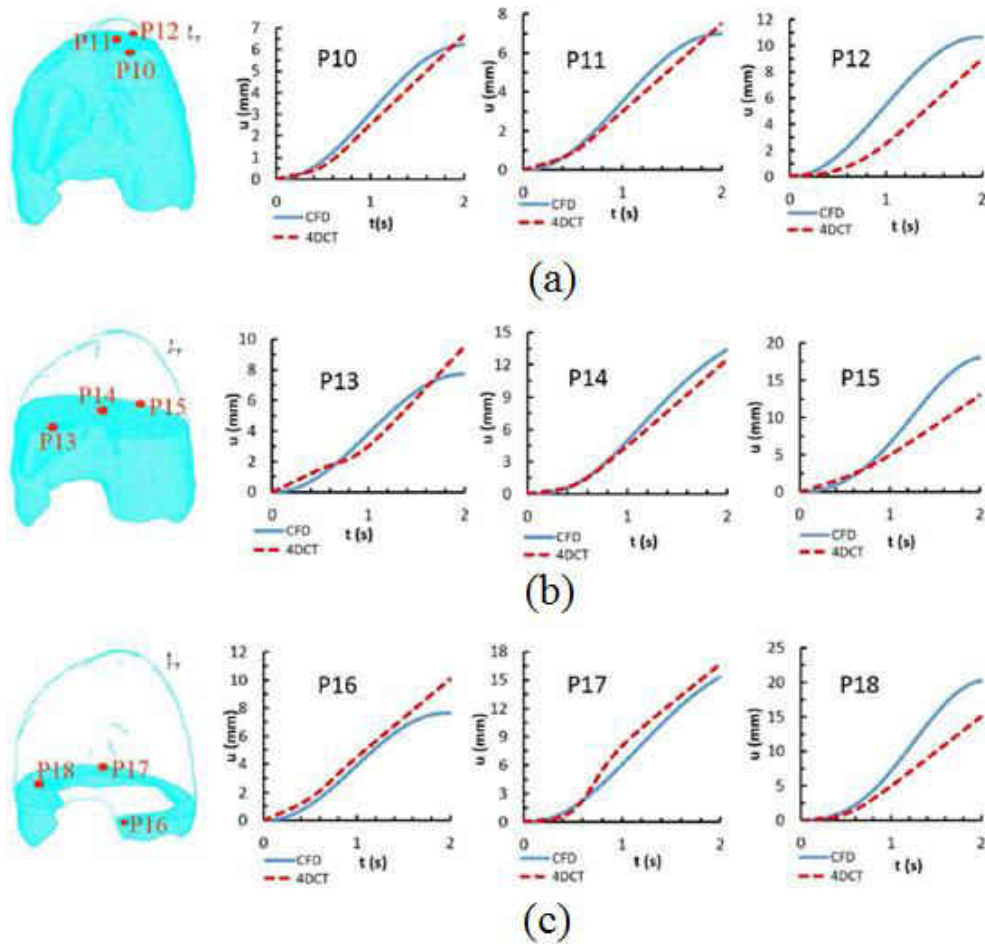


Figure 4-7: Comparison of prediction displacement for monitored landmarks located at the (a) top (b) middle and (c) bottom of the right lung over the inhalation phase

4.5 Discussion

A biomechanical model has been developed and applied to model spatial lung deformation and validated with data obtained from 4DCT registration on two human patients. The average local error and standard deviation in each direction are used as metrics to assess the accuracy of the model. The regional difference in the prediction error is also investigated. The regions near the ribcage and heart exhibit relatively larger displacement errors than the interior of the lungs. The transient absolute displacement obtained from imaging and biomechanical modeling are monitored and compared at 18 locations for both left and right lungs. The discrepancy between the methods is generally less than 3 millimeters, for most of the interior of the lung which is considered acceptable for radiotherapy. Specifically, the lung radiotherapy literature indicates that a 3 mm (or more) margin is typically associated with motion uncertainty [111]. However, the observed error for the landmarks near the outer surface and the heart is observed to be relatively large. This discrepancy suggests contact between the lung and chest wall, as well as impact of heart motion should be major areas for further investigation and model improvement.

The predicted displacement was found to be significantly improved by allowing for the heterogeneity of lung tissue. At the bifurcation of the airway, the predicted average AP, LR and SI errors are reduced by 0.39 mm, 1.2 mm, and 2.17 mm respectively for patient 1. The corresponding values for Patient 2 are 0.41 mm, 0.6 mm, and 1.02 mm.

The 4DCT registration technique provides a direct means to obtain the displacement field from a set of images, but the physiological and physical properties of the lung are not considered. On the other hand, biomechanical modeling enables consideration of the physiology of the breathing

process and the physical properties in a dynamical model through the boundary conditions and material properties. However the necessary simplifications and approximations associated with modeling could affect the accuracy of the results. Thus the need for model validation as reported here. A comparison of the results obtained from these two approaches provides a means of assessing sufficiency versus accuracy in the choice of the technique for determining lung deformation. The displacement results obtained from biomechanical modeling have the capability to provide more detailed spatio-temporal information thorough specification of the appropriate time steps than the image registration. For example, the image-based deformation assessed in this study was obtained for 10% tidal volume intervals while the biomechanical model provides deformation at 5% tidal volume intervals (time step of 0.1 sec).

The biomechanical model here extends beyond previous studies by utilizing human patient-specific and spatially distributed material properties. In contrast, most of the previous biomechanical modeling studies on human lung have used uniform material constants obtained from experiments on animal tissue or cadaver, which are inadequate for human radiotherapy.

CHAPTER 5: ANALYTIC INTERMODEL CONSISTENT MODELING OF VOLUMETRIC HUMAN LUNG DYNAMICS¹

5.1 Introduction

Respiratory motion is a potential source of error in the treatment of lung cancer using advanced therapies such as radiotherapy. Accurate prediction of lung deformation may aid targeted radiotherapy, ensuring precise tumor localization and underexposure of the surrounding healthy tissues to ionizing radiation [2]. Numerical modeling of human lung dynamics enables simulation and visualization of lung deformation based on underlying physics and physiology. However, the accuracy of numerical results may be affected by the inherent difficulties in computational modeling of a complicated system like the human lung. This chapter presents a method to couple the results of computational modeling and 4D DIR method to improve accuracy of predicted lung deformation.

Recent advances in Computed Tomography (CT) and Magnetic Resonance (MR) acquisition techniques have enabled direct dynamic imaging of respiratory motion. Four-dimensional computed tomography (4DCT) imaging [4] and dynamic magnetic resonance imaging (DMRI) [5] are used in radiation therapy to provide images of tumor and associated organ at different breathing phases. In addition, deformable image registration (DIR) methods and in particular, biomechanical modeling of the lung, facilitate precise estimation of lung tumor location during respiration.

¹ *The materials of this Chapter have been previously published in:*[112]O. Ilegbusi, B. Seyfi, J. Neylon, and A. P. Santhanam, "Analytic Intermodel Consistent Modeling of Volumetric Human Lung Dynamics," *Journal of biomechanical engineering*, vol. 137, p. 101005, 2015.

Biomechanical modeling has the advantage of being able to account for the physiology of the breathing process and the physical properties through the boundary conditions and material properties, in a dynamical model.

A number of studies have generally either considered the lung as a one-phase continuum and modeled its contact behavior [28, 53] or modeled airflow in the lung and the mechanical coupling between the deformation of the solid tissue skeleton and the airflow [38, 113]. However, even with advanced 4D imaging techniques and biomechanical modeling, errors and uncertainty in tracking lung anatomy during breathing are inevitable due to inherent limitation in imaging techniques and approximations in biomechanical modeling. The inherent difficulty in specifying exact boundary conditions, heterogeneous nature of material properties, fluid-structure interaction between air and the poro-elastic lung tissue, and complex geometry, make biomechanical modeling a challenge. As a consequence, the necessary simplification and approximations associated with modeling may affect the accuracy of the predicted results.

It should be remarked that methodology presented in this chapter is universally applicable to lungs with and without tumor. It is particularly well suited for lungs with tumor since it involves acquisition of data for the spatial material properties over the lung parenchyma with or without tumor.

We investigate the integration of CFD-based analysis and 4D DIR for consistent representation of human lung dynamics. Specifically, Tikhonov regularization (TR) [7] is used to integrate quantitative image analysis and CFD simulation results in the human lung. The 4D DIR data is obtained by 4DCT image registration algorithm to estimate lung motion. The biomechanical

modeling utilizes a flow-structure interaction model to simultaneously solve the airflow equations and structural dynamics of the lung tissue. The lung is modeled as a poro-elastic medium with subject-specific heterogeneous elastic properties on a 3D geometry, reconstructed from 4DCT scan datasets of a human patient.

The following sections describe the methodology, followed by presentation of the results and subsequently, conclusion summarizing the findings of the study.

5.2 Materials and Methods

This section describes the fusion algorithm and provides some details on the formulation of the approach including the biomechanical model and imaging technique. The displacement obtained from the 4DCT algorithm is integrated with CFD solution using a fusion algorithm. The detailed description of each step involved is detailed below.

5.2.1 Fusion Algorithm

Let $\mathbf{f}_{opt}(\mathbf{x})$, $\mathbf{f}_{4DCT}(\mathbf{x})$ and $\mathbf{f}_{CFD}(\mathbf{x})$ respectively represent optimal displacement, 4DCT (linear elastic model based) displacement, and CFD displacement vectors associated with a 3D anatomy. The optimal displacement is computed by fusing the displacement results obtained from 4DCT and biomechanical model. We now introduce the following regularization terms: (a) $\omega(\mathbf{f}_{opt}(\mathbf{x}), \mathbf{f}_{CFD}(\mathbf{x}))$ representing the discrepancy between the optimal displacement vectors and the CFD-based displacement; and (b) $\epsilon(\mathbf{f}_{opt}(\mathbf{x}), \mathbf{f}_{4DCT}(\mathbf{x}))$ representing discrepancy between the optimal displacement and the linear elasticity model based (4DCT) deformation vectors. We first

define an objective functional, $\mathbf{z}(\mathbf{f}_{opt}, \mathbf{f}_{4DCT}, \mathbf{f}_{CFD})$, which represents the discrepancy between the displacement obtained from 4DCT registration and the displacement obtained using the CFD-based flow-structure interaction modeling. The formulation is given as:

$$\mathbf{z}(\mathbf{f}_{opt}, \mathbf{f}_{4DCT}, \mathbf{f}_{CFD}) = \frac{1}{2} \alpha \boldsymbol{\varepsilon}(\mathbf{f}_{opt}(\mathbf{x}), \mathbf{f}_{4DCT}(\mathbf{x})) + \frac{1}{2} \boldsymbol{\omega}(\mathbf{f}_{opt}(\mathbf{x}), \mathbf{f}_{CFD}(\mathbf{x})) \quad (5-1)$$

where α is a regularization parameter. The regularization operator $\boldsymbol{\omega}(\mathbf{f}_{opt}(\mathbf{x}), \mathbf{f}_{CFD}(\mathbf{x}))$ is estimated by assuming that the space of functions to be Hilbert space, which has squared-integrable generalized derivative and $\boldsymbol{\varepsilon}(\mathbf{f}_{opt}(\mathbf{x}), \mathbf{f}_{4DCT}(\mathbf{x}))$ is defined as standard square error.

Substituting the definitions of $\boldsymbol{\omega}(\mathbf{f}_{opt}(\mathbf{x}), \mathbf{f}_{CFD}(\mathbf{x}))$ and $\boldsymbol{\varepsilon}(\mathbf{f}_{opt}(\mathbf{x}), \mathbf{f}_{4DCT}(\mathbf{x}))$ in Equation (5-1), the objective functional, $\mathbf{z}(\mathbf{x})$, for a 3D domain is obtained as:

$$\mathbf{z}(\mathbf{f}_{opt}, \mathbf{f}_{4DCT}, \mathbf{f}_{CFD}) = \frac{1}{2} \alpha [\mathbf{f}_{4DCT}(\mathbf{x}) - \mathbf{f}_{opt}(\mathbf{x})]^2 + \frac{1}{2} [\mathbf{f}_{opt}(\mathbf{x}) - \mathbf{f}_{CFD}(\mathbf{x})]^2 + \frac{1}{2} \{\nabla \cdot [\mathbf{f}_{opt}(\mathbf{x}) - \mathbf{f}_{CFD}(\mathbf{x})]\}^2 \quad (5-2)$$

Using results obtained from the CFD solver and the results obtained from 4DCT registration, our ultimate goal is to seek numerical solution to minimize Equation (5-2) as described below.

The computational complexity of Equation (5-2) is implicitly related to the linear deformation model parameters and the CFD porosity parameters. Solving for a uniform material distribution for both of these systems is straightforward but too simplistic for representing the lung anatomy. A heterogeneous distribution of both the elastic parameters in the linear deformation model and the porosity parameters in the CFD model is critical for predicting accurate results. However, such

a distribution of parameters will lead to a very complex system to solve. We now present a mechanism that simplifies the minimization problem in such a way that accounts for the heterogeneous nature of the lung elasticity and porosity.

Finite element analysis is used to obtain the numerical solution of the objective functional, Equation (5-2). For each element, the minimum of the objective functional can be obtained by differentiating the equation with respect to nodal values in that specific element. The numerical solution of the objective functional is detailed in the appendix.

5.2.2 4DCT Registration using Optical Flow (f_{4DCT})

As explained in the previous Section 5.2.1, the deformation values obtained from 4DCT registration (\mathbf{f}_{4DCT}) are used as the input to the fusion algorithm. This section describes the registration method used to obtain the \mathbf{f}_{4DCT} values.

Using the 4DCT data registration algorithm the motion of each 3D voxel at the end-expiration 3D volume data is estimated by searching for and locating a corresponding voxel in another 3D volume at a different breathing phase. An optical flow motion estimation algorithm, was used for the registration based on local Taylor series approximation [114].

One of the limitations of the optical flow method as applied to estimating the 3D organ motion is the low sensitivity to variations in regional motion. In order to improve the accuracy of the optical flow algorithm, a multi-level, multi-resolution optical flow method [4] was used, which computed optical flow between two 3D volumes at low resolution, propagated the result to the higher resolution volume, and subsequently to the original resolution volume data. In this approach, the

organ anatomy was divided into four parts: (1) lung outline, (2) large capillaries, (3) small capillaries, and (4) parenchyma. At each level of anatomy, a multi-level, multi-resolution optical flow registration was used to compute the 4D organ motion of that anatomy and integrated into the next level. The four anatomical parts are semi-automatically separated using a seed-based region-growth algorithm. The motion consistency during the registration process is enabled by the Thin Plate Splines applied at the anatomical boundaries [115].

5.2.3 CFD Model Analysis (f_{CFD})

This section describes the different steps involved in CFD modeling of spatial lung displacement (f_{CFD}). It considers the heterogeneity of the elasticity of lung tissue. The presence of vessels, bronchial tree and tumor (in the case of cancerous lung), creates inhomogeneity in the lung material properties. This inhomogeneity is represented by spatially distributed properties.

5.2.3.1 Reconstruct 3D Geometry of Real Human Lung from 4DCT Scan Dataset

4DCT scans of the lung are obtained from a specific patient at the UCLA Department of Radiation Oncology, Los Angeles, California. The dataset constitutes a sequence of 3DCT scans representing the volumetric lung anatomy at different air volumes and pressure–volume curves. The 4DCT scan dataset provides roughly 255 image slices (one slice per mm) of the lung. The resolution of each slice is 512×256 mm². The images are processed using the MIMICS software [116] to reconstruct the surface geometry of the lung.

5.2.3.2 Generate Computational Meshes in the Reconstructed Lung Geometry

The surface of the lung obtained after image processing is used as input to the 3-matic software [117]. This software is used to correct the typical errors associated with data transfer from a 3D digitization session, including missing data and extraneous parts. The surface of the lung is meshed with three-node triangular computational elements and used to generate a finite element discretization in the interior. Four-node-tetrahedral elements are used for volume discretization. A total of 37,752 surface meshes and 240,164 volume meshes are used for the left lung, while the corresponding values for the right lung are 38,298 and 279,181. Figure 5-1(a) and Figure 5-1(b) show the reconstructed 3D geometry for the left and right lungs respectively.

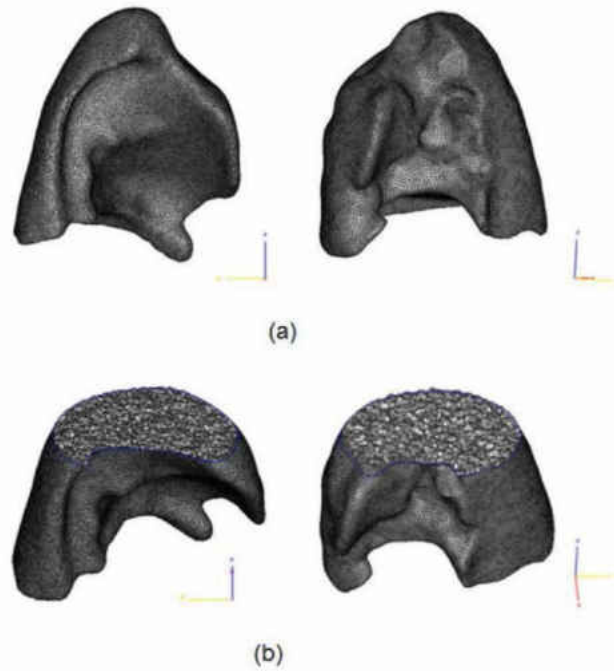


Figure 5-1: Three dimensional lung shapes generated from 4D-CT scan; (a) surface meshes (b) cutout of a section of reconstructed lungs, typical computational volume meshes generated and applied in the finite element model

5.2.3.3 Governing Equations

The biomechanical model involves solution of the coupled poro-elastic flow-structure interaction sets of equations within the lung. The porosity represents the proportion of total volume (solid and fluid) which is occupied by the fluid, and is defined as [88]

$$\phi = 1 - \frac{J^0}{J} (1 - \phi^0) \tag{5-3}$$

where \mathbf{J} is the geometric element Jacobian and the superscript “0” indicates the quantities at initial reference configuration.

In contrast to the conventional fluid-structure interaction approach in which fluid and structural variables are coupled only at the interface, the present analysis allows coupling in the entire porous medium [88]. The microscopic fluid stress ($\boldsymbol{\sigma}_f \equiv -p_f \mathbf{I}$) is added to the structural model as internal stress and displacement compatibility must be satisfied throughout the porous medium ($\mathbf{u}_f = \mathbf{u}_s = \mathbf{u}$) where \mathbf{u}_f and \mathbf{u}_s represent the fluid and solid displacement, respectively.

Assuming incompressible transient flow condition in the fluid domain, the pore fluid flows through the porous solid structure according to the Darcy’s law [88], thus:

$$\frac{\mu_f}{\mathbf{K}} \cdot (\mathbf{v} - \mathbf{w}) + \nabla p_f + \rho_f \mathbf{g} = \mathbf{0} \quad (5-4)$$

where \mathbf{K} , μ_f and ρ_f represent the permeability tensor, viscosity and density of air respectively, p_f is the local (pore) pressure, \mathbf{v} is the air velocity vector and \mathbf{w} represents the moving mesh velocity vector. The displacement compatibility indicates that the moving mesh velocity is equal to the solid velocity ($\mathbf{w} = \dot{\mathbf{u}}$) throughout the porous medium. In the solid domain the lung tissue is assumed to be linear isotropic elastic [89, 90]. Note that the isentropic assumption is considered within each element and the Young’s modulus varies from one element to another. The solid displacement is obtained by solving for the elastic displacement field, \mathbf{u} , from the Navier’s equation:

$$G \nabla^2 \mathbf{u} + \frac{G}{1-2\nu} \nabla(\nabla \cdot \mathbf{u}) = \nabla p_f - \mathbf{b} \quad (5-5)$$

where G and ν are the tissue Shear modulus and Poisson ratio, respectively, and \mathbf{b} is body force.

The Shear modulus is related to the Young's modulus (E) through the relation $G = \frac{E}{2(1+\nu)}$.

Equations (5-4) and (5-5) are solved for the individual, specific patient lung geometry using the ADINA computational code [91] to predict spatial distribution of the lung displacement ($\mathbf{u} = \mathbf{f}_{CFD}$). This displacement is used as input in the fusion algorithm as described in a previous Section 5.2.1.

5.2.3.4 Material Properties

The local elastic properties of the subject-specific lung are determined using an inverse non-invasive methodology [22]. The maximum Young's modulus (YM) obtained at the lower part of the lobe is 4.03 kPa for the left lung and 4.05 kPa for the right lung, while a minimum value of 0.01 kPa is obtained at the top for both lungs. The average YM obtained and used in the present study is 0.64 kPa for the left lung and 0.67 kPa for the right lung. These values fall within the range that has been used in other studies [50]. The heterogeneous YM values are implemented in the CFD model using in-house C code.

5.2.3.5 Input Data and Boundary Condition

The Poisson ratio ν is assumed to be 0.35, which falls within the range (0.25-0.47) suggested in previous studies [118]. The lung density is assumed to be 700kg/m³ [118].

The spatially-dependent Young's modulus obtained in Section 5.2.3.4 is utilized in the model. The inlet is assumed to be at the hilum where the airway enters the lung, determined by the intersection of the trachea with the lung. Periodic pressure boundary condition is imposed at the inlet to the

lobe as illustrated in Figure 5-2 over one breathing cycle. The inlet pressure is assumed to reach its maximum value at $t=2\text{sec}$ at the end of the inhalation phase.

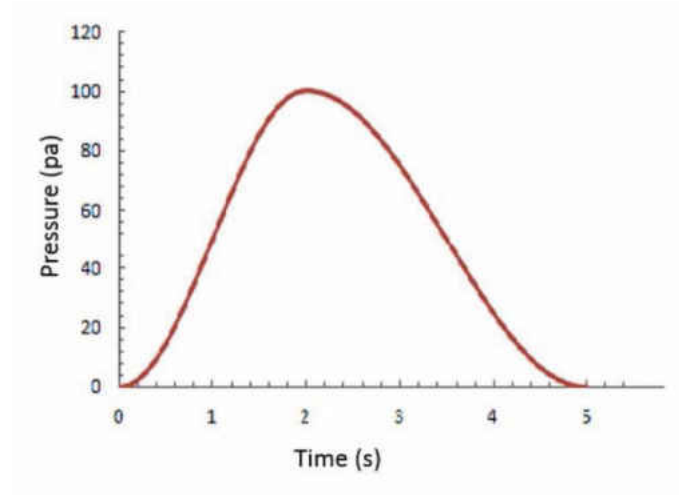


Figure 5-2: Prescribe inlet pressure

5.3 Results

The following presents the results obtained from the experiment and CFD model. These results are utilized in testing the current state of the fusion algorithm.

5.3.1 *Image Registration Results*

Figure 5-3 shows the CT slice of the lung anatomy at the end-expiration stage. This anatomy is used as the reference anatomy and the voxel deformation is computed for each voxel in the end-expiration stage by mapping to the end-inspiration stage.

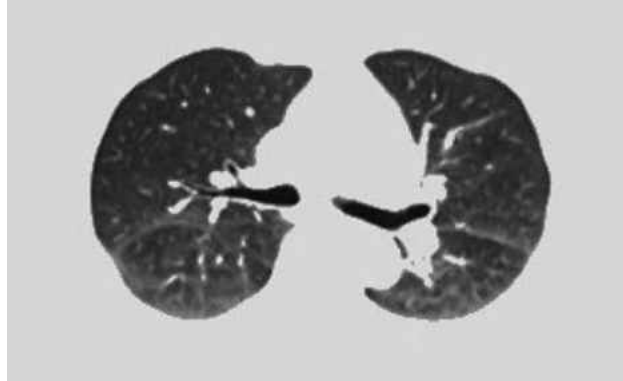


Figure 5-3: 3DCT lung anatomy used as the reference geometry for the CFD analysis

Figure 5-4 (a) depicts the 3D lung deformation computed using the 4D DIR for the left lung. The corresponding results for the right lung are presented in Figure 5-4(b), illustrating the differences between the deformation of both lungs. Figure 5-5(a) and Figure 5-5(b) show the 3D volume-rendered representation of the Young's modulus obtained from the linear elastic deformation model and the 4D lung DIR mechanism.

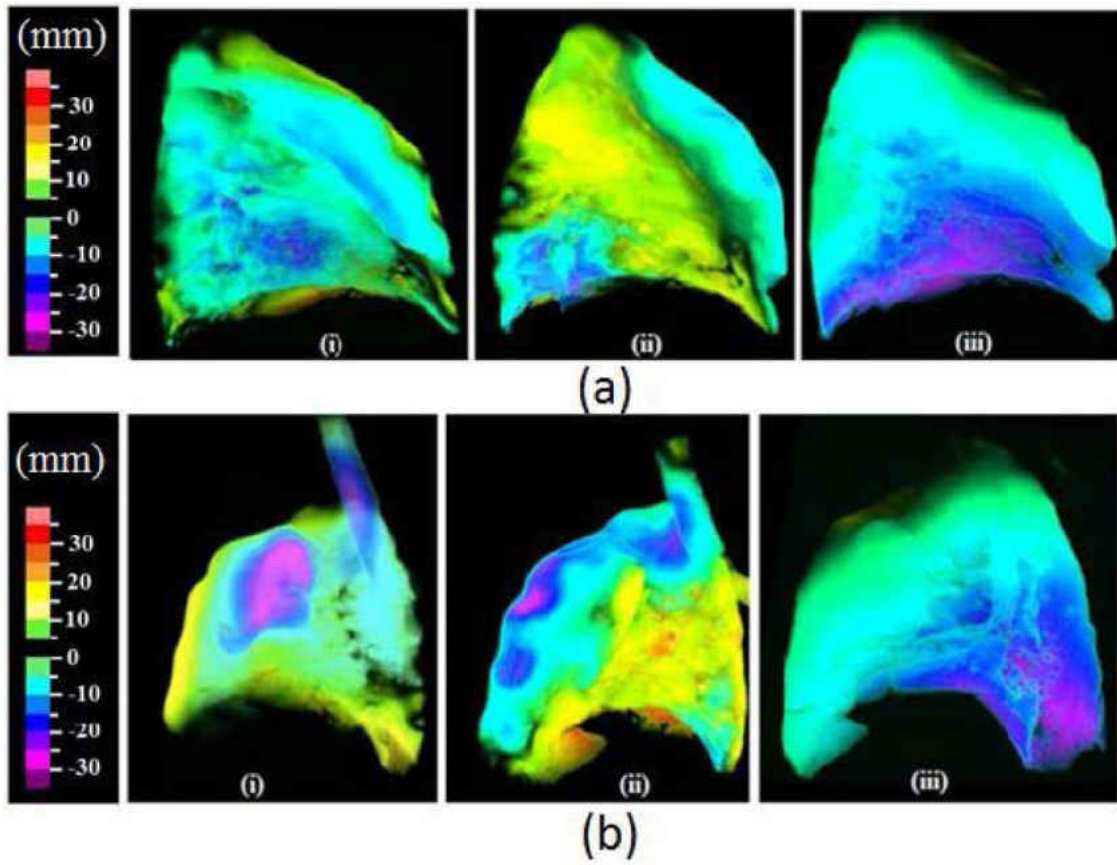


Figure 5-4: Lung deformation along the (i) x axis, (ii) y axis, and (iii) z axis computed for the (a) left lung and (b) right lung using a multi-resolution optical flow algorithm

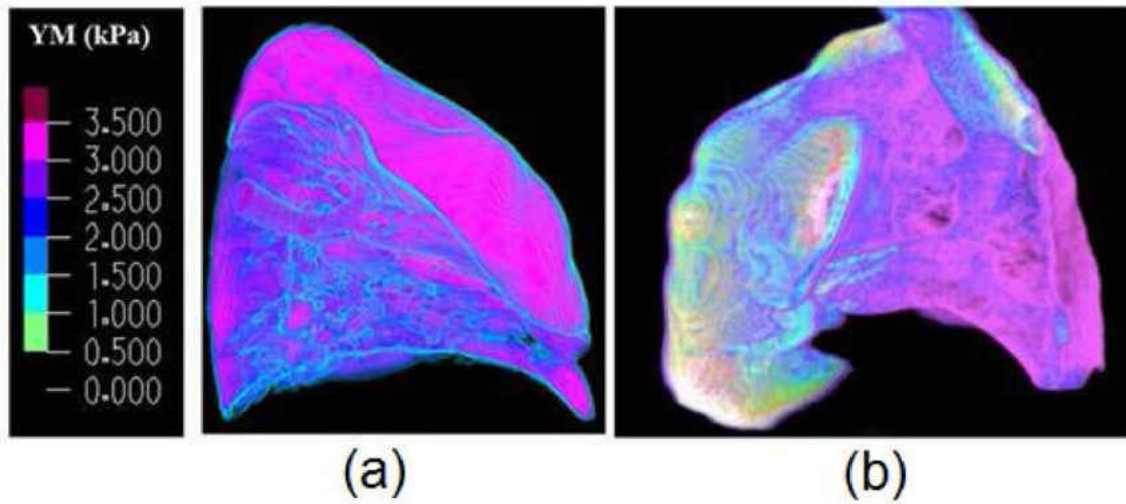


Figure 5-5: Three-dimensional volume rendering of the Young's modulus values for the (a) right and (b) left lung obtained from the 4DCT lung registration and a linear deformation model

5.3.2 CFD Results

The predicted map of displacement using the porous flow-structure interaction model in x, y and z directions (in mm) is plotted in Figure 5-6 (a) and Figure 5-6 (b) for the left and right lung, respectively. The maximum and minimum displacements are presented for both lungs with variations between the two extremes.

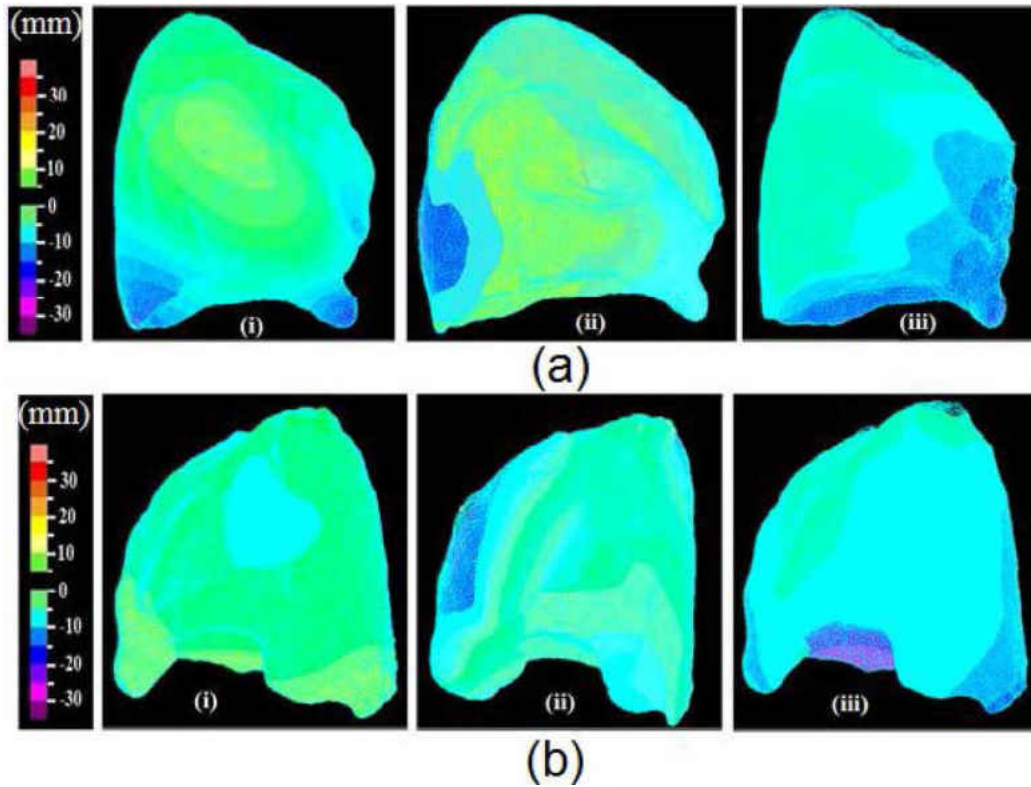


Figure 5-6: Lung deformation along the (i) x axis, (ii) y axis, and (iii) z axis computed for the (a) left lung and (b) right lung using CFD model

5.3.3 *Optimal Results from Fusion Algorithm*

The fused displacement results obtained from fusion algorithm are used to calculate the spatially distributed optimal Young's modulus in an inverse manner. The value of the optimized Young's modulus are applied in the CFD model to obtain the optimal displacement. Figure 5-7 (a) and Figure 5-7 (b) show the predicted map of the optimal CFD displacement in the x, y and z directions (in mm) for the right and left lung, respectively. The maximum and minimum displacements are presented for both lungs with variations between the two extremes.

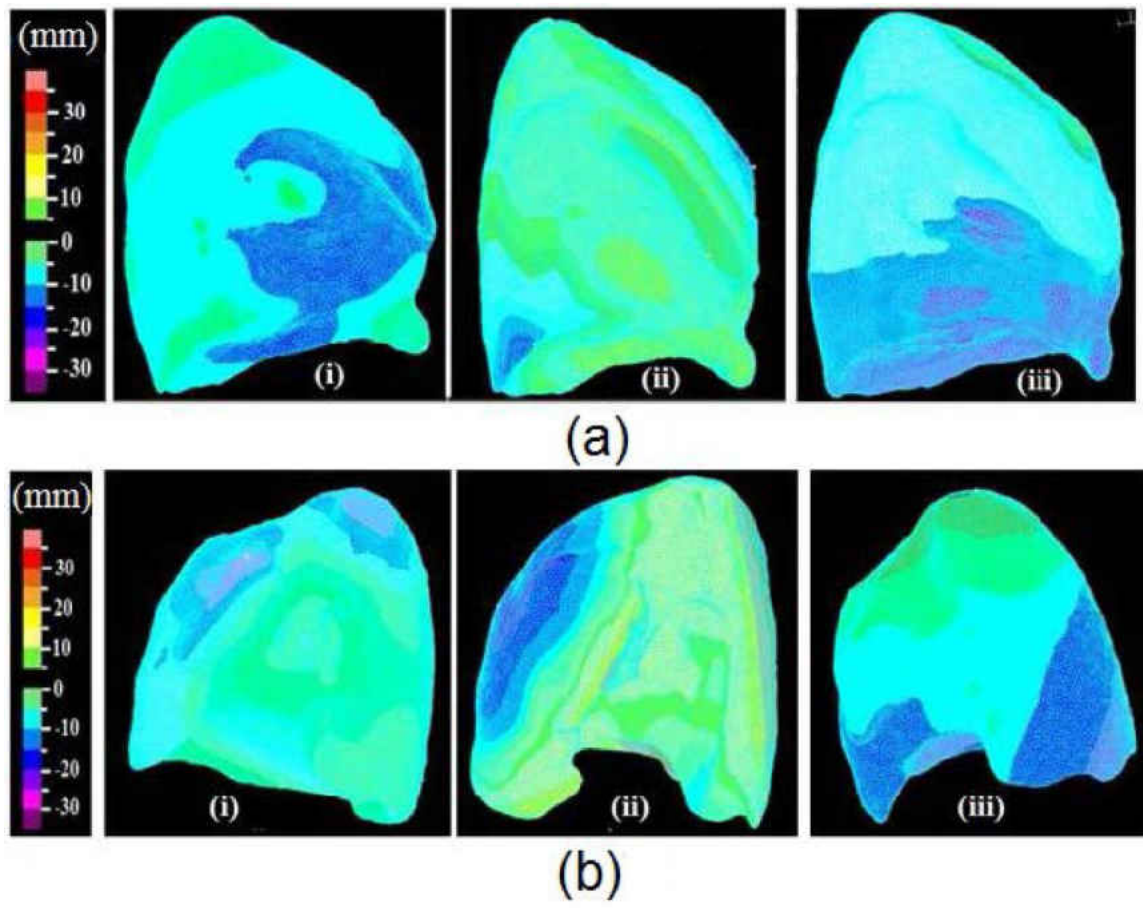


Figure 5-7: Optimal lung deformation along the (i) x axis, (ii) y axis, and (iii) z axis computed for the (a) left lung and (b) right lung

5.3.4 Validation

Figure 5-8 shows the discrepancy observed between the optimal lung deformation and the deformation observed in 4DCT DIR. The results show that the discrepancies are less than 3 mm for most of the interior nodes and larger on the surface, particularly at the sharp edges of the lungs.

In order to investigate the effect of optimization in error reduction, the absolute displacement error for 15 selected landmark locations in both lungs are monitored and compared for both the CFD and optimal model. Table 5-1 compares the CFD simulation errors between the initial YM and optimal YM after the regularization. The DIR results are used as the gold standard to validate the results of the optimal CFD model.

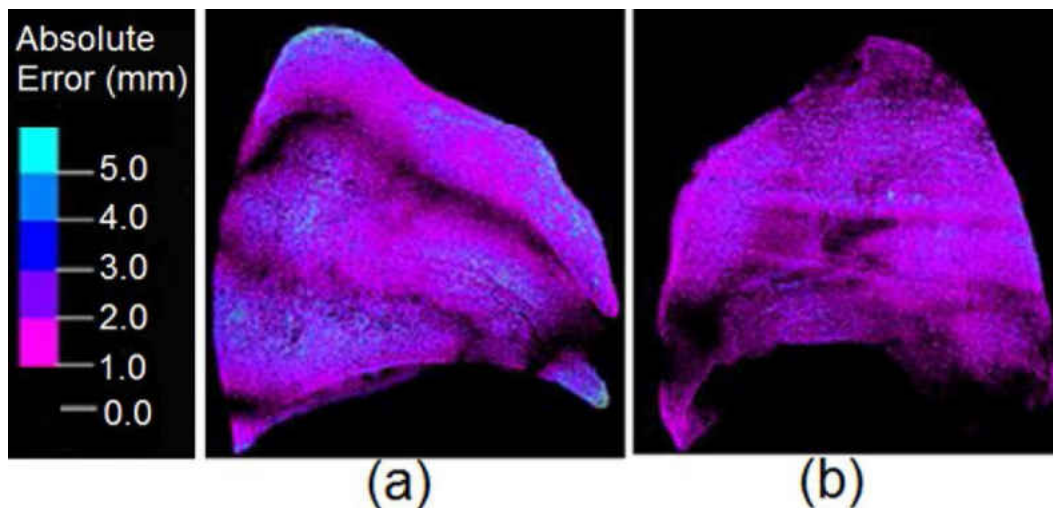


Figure 5-8: Differences in the displacement observed between the optimal lung deformation and the deformation observed in the 4D-CT DIR shown for (a) left and (b) right lungs

Landmarks are selected at the interior, sharp edges and surfaces, identified by their x, y, z coordinates. The same coordinate system is used for the biomechanical model, 4DCT and the fusion model. Therefore, having the x, y, z coordinates for each landmark, the same landmarks were chosen for comparison.

Figure 5-9 (a) and Figure 5-9 (b) show the selected landmark locations (P1-P15) in the left and right lungs, respectively. Table 5-1 shows the absolute errors obtained from the standard CFD and optimal model for both lungs. The results for optimal model indicate a smaller error compared to the standard CFD model. The 95% confidence interval for the displacement error for the selected landmarks in both lungs is (3 ± 0.41) mm for the biomechanical model and (1.50 ± 0.46) mm for the optimal model. The landmarks on the surfaces and sharp edges are shown in gray while landmarks in the interior are shown in white in Table 5-1. Optimization results in a significant reduction in error for the interior landmarks. In the left lung, the average error for the landmarks on the surface and edges is reduced by 1.11 mm while this value is 2.96 mm for the interior nodes. In the right lung, the average displacement errors after optimization are reduced by 1.34 mm and 0.86 mm for the interior and surface nodes, respectively. These results show that although optimization is effective in reducing the displacement error at the surface nodes, it is more effective for the interior nodes.

Table 5-1: Discrepancy observed between the CFD (deformation) results using initial YM values and CFD (deformation) results using optimal YM values (mm) and the deformation observed in

4DCT DIR

Left Lung			Right Lung		
Nodes	Absolute error (mm)- CFD results using initial YM values	Absolute error (mm)- CFD results using optimal YM values	Nodes	Absolute error (mm)-CFD results using initial YM values	Absolute error (mm)- CFD results using optimal YM values
P1	3.5	3.2	P16	3.73	1.41
P2	3.68	2.19	P17	4.07	3.15
P3	4.39	4.03	P18	1.71	1.51
P4	2.5	0.22	P19	3.86	2.91
P5	4.92	1.49	P20	1.64	0.54
P6	4.5	0.28	P21	1.34	0.67
P7	3.3	0.011	P22	3.79	2.16
P8	3.3	2.03	P23	2.35	0.6
P9	4.5	0.51	P24	0.85	0.088
P10	2.11	0.51	P25	1.42	0.71
P11	2.98	2.6	P26	2.83	1.16
P12	1.83	0.43	P27	2.41	0.00
P13	4.03	4.00	P28	2.5	2.00
P14	3.8	0.28	P29	3.01	2.56
P15	4.09	3.5	P30	0.77	0.09

Landmarks on the surfaces and sharp edges are shown in gray.

Landmarks in the interior are shown in white.

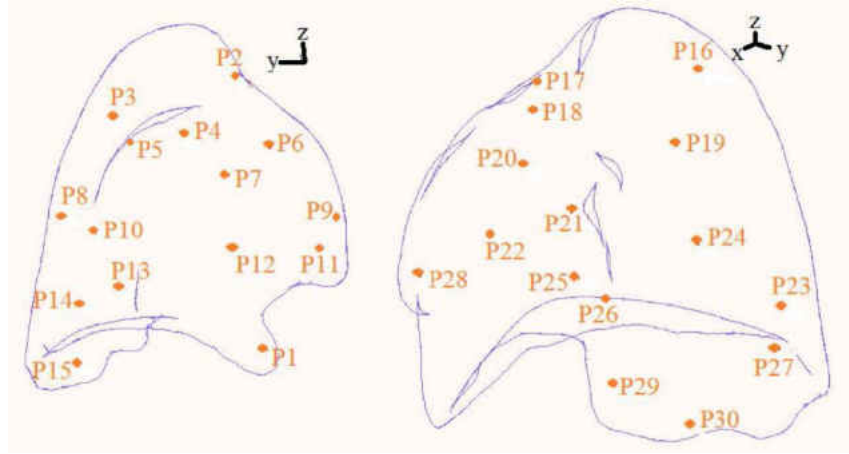


Figure 5-9: Location of selected landmarks in (a) left and (b) right lung

5.4 Conclusion

A mathematical method is developed to integrate deformation results from a deformable image registration (DIR) and physics-based modeling approaches in order to represent consistent volumetric lung dynamics. The computational fluid dynamics (CFD) simulation assumes the lung is a poro-elastic medium with spatially distributed elastic property.

Simulation is performed on a 3D lung geometry reconstructed from four-dimensional computed tomography (4DCT) dataset of a human subject. The heterogeneous Young's modulus (YM) is estimated from a linear elastic deformation model with the same lung geometry and 4D lung DIR. The deformation obtained from the CFD is then coupled with the displacement obtained from the 4D lung DIR by means of the Tikhonov regularization (TR) algorithm. The numerical results include 4DCT registration, CFD, and optimal displacement data which collectively provide

consistent estimate of the volumetric lung dynamics. The fusion method is validated by comparing the optimal displacement with the results obtained from the 4DCT registration.

For the landmarks inside the lung, the optimization results in a significant reduction in error. Specifically, in the left lung, the average error for the landmarks on the surface and edges is reduced by 1.11 mm while this value is 2.96 mm for the nodes, while, in the right lung, the average displacement errors after optimization are reduced by 1.34 mm and 0.86 mm for the interior and surface nodes respectively.

Although validation of the results discussed in Table 5-1 can prove the optimality of the regularization process, a phantom study would be ideal to systematically understand the regularization process. Such a lung phantom that is both compatible with the patient's observed physiology and airflow physics does not currently exist. The design of such physics-based multi-modality consistent lung models would be desirable in a future study.

5.5 Nomenclature

b	body force
c	optimal nodal value vectors
E	Young's modulus
f_{CFD}	CFD displacement
f_{opt}	optimal displacement
f_{4DCT}	4DCT displacement
g	gravity vector
G	Shear modulus
$h, l_e, m, n_e, o, p_e, q_e, t$	Interpolation functions
I	identity matrix
J	geometric element Jacobian
K	permeability tensor
p_f	the local (pore) pressure
q	number of nodes

R	the SO(3) rotation group matrix
S	expansion of the SO(3) rotation group matrix in 3D
u	lung displacement vector
v	air velocity vector
w	moving mesh velocity vector
Y	HSH transform
z	objective functional
α	regularization parameter
γ	CFD nodal value vectors
δ	Dirac delta function
ε	discrepancy between optimal and 4DCT displacement
(θ, φ, χ)	hyper-spherical coordinate
μ_f	air viscosity
ν	Poisson ratio
ρ_f	density of air

σ_f *fluid stress*

ω regularization operator

ϕ porosity

Superscript

e element defined variable

0 initial reference configuration

Subscript

CFD CFD value

e element defined variable

opt optimal value

λ, l, m, n HSH coefficients

0 coordinate origin

4DCT 4DCT value

5.6 Appendix: Numerical Solution of the Objective Functional

The functions in Equation (6-2) are defined based on the nodal values. For each element, consider $e=1, 2 \dots q$; q represents the number of nodes and $\mathbf{c}(\mathbf{x}_e)$ and $\boldsymbol{\gamma}(\mathbf{x}_e)$ are the optimal and CFD nodal value vectors, respectively. Then within each element, the optimal and CFD functions are defined respectively as:

$$\mathbf{f}_{opt}(\mathbf{x}) = \sum_{e=0}^q \mathbf{h}(\mathbf{x}, \mathbf{x}_e) \mathbf{c}(\mathbf{x}_e) \quad (5-6)$$

$$\mathbf{f}_{CFD}(\mathbf{x}) = \sum_{e=0}^q \mathbf{h}(\mathbf{x}, \mathbf{x}_e) \boldsymbol{\gamma}(\mathbf{x}_e) \quad (5-7)$$

In the above equations, $\mathbf{h}(\mathbf{x}, \mathbf{x}_e)$ is the interpolation function. The optimal and CFD functions are in fact the sum over all nodal values in the element. By defining the optimal and CFD functions in terms of nodal values, the next step is to substitute these functions in Equation (5-2) and differentiate with respect to nodal values to find the minimum objective functional in each element.

$$\begin{aligned} \mathbf{z} = & \frac{1}{2} \alpha [\mathbf{f}_{4DCT}(\mathbf{x}) - \sum_{e=0}^q \mathbf{h}(\mathbf{x}, \mathbf{x}_e) \mathbf{c}(\mathbf{x}_e)]^2 + \frac{1}{2} \sum_{e=0}^q \mathbf{h}^2(\mathbf{x}, \mathbf{x}_e) [\mathbf{c}(\mathbf{x}_e) - \boldsymbol{\gamma}(\mathbf{x}_e)]^2 + \\ & \frac{1}{2} \sum_{e=0}^q \mathbf{o}^2(\mathbf{x}, \mathbf{x}_e) [\mathbf{c}(\mathbf{x}_e) - \boldsymbol{\gamma}(\mathbf{x}_e)]^2 + \frac{1}{2} \sum_{e=0}^q \mathbf{t}^2(\mathbf{x}, \mathbf{x}_e) [\mathbf{c}(\mathbf{x}_e) - \boldsymbol{\gamma}(\mathbf{x}_e)]^2 + \\ & \frac{1}{2} \sum_{e=0}^q \mathbf{m}^2(\mathbf{x}, \mathbf{x}_e) [\mathbf{c}(\mathbf{x}_e) - \boldsymbol{\gamma}(\mathbf{x}_e)]^2 \end{aligned} \quad (5-8)$$

where \mathbf{o} , \mathbf{t} and \mathbf{m} are new interpolation functions, defined as $\frac{\partial \mathbf{h}(\mathbf{x}, \mathbf{x}_e)}{\partial x}$, $\frac{\partial \mathbf{h}(\mathbf{x}, \mathbf{x}_e)}{\partial y}$, and $\frac{\partial \mathbf{h}(\mathbf{x}, \mathbf{x}_e)}{\partial z}$ respectively.

Differentiating Equation (5-8) with respect to $\mathbf{c}(\mathbf{x}_e)$,

$$\begin{aligned} \frac{\partial z}{\partial \mathbf{c}(\mathbf{x}_e)} = & \tau^e \alpha [\mathbf{f}_{4DCT}(\mathbf{x}) - \sum_{e=0}^q \mathbf{h}(\mathbf{x}, \mathbf{x}_e) \mathbf{c}(\mathbf{x}_e)] [-\mathbf{l}_e(\mathbf{x}, \mathbf{x}_e) + \sum_{e=0}^q \mathbf{h}(\mathbf{x}, \mathbf{x}_e) \mathbf{l}_e(\mathbf{x}, \mathbf{x}_e) [\mathbf{c}(\mathbf{x}_e) - \\ & \boldsymbol{\gamma}(\mathbf{x}_e)] + \sum_{e=0}^q \mathbf{o}(\mathbf{x}, \mathbf{x}_e) \mathbf{n}_e(\mathbf{x}, \mathbf{x}_e) [\mathbf{c}(\mathbf{x}_e) - \boldsymbol{\gamma}(\mathbf{x}_e)] + \sum_{e=0}^q \mathbf{t}(\mathbf{x}, \mathbf{x}_e) \mathbf{p}_e(\mathbf{x}, \mathbf{x}_e) [\mathbf{c}(\mathbf{x}_e) - \boldsymbol{\gamma}(\mathbf{x}_e)] + \\ & \sum_{e=0}^q \mathbf{m}(\mathbf{x}, \mathbf{x}_e) \mathbf{q}_e(\mathbf{x}, \mathbf{x}_e) [\mathbf{c}(\mathbf{x}_e) - \boldsymbol{\gamma}(\mathbf{x}_e)] \end{aligned} \quad (5-9)$$

$$\text{where, } \mathbf{l}_e(\mathbf{x}, \mathbf{x}_e) = \frac{\partial \mathbf{h}(\mathbf{x}, \mathbf{x}_e)}{\partial \mathbf{c}(\mathbf{x}_e)}, \mathbf{n}_e(\mathbf{x}, \mathbf{x}_e) = \frac{\partial \mathbf{o}_e(\mathbf{x}, \mathbf{x}_e)}{\partial \mathbf{c}(\mathbf{x}_e)}, \mathbf{p}_e(\mathbf{x}, \mathbf{x}_e) = \frac{\partial \mathbf{t}_e(\mathbf{x}, \mathbf{x}_e)}{\partial \mathbf{c}(\mathbf{x}_e)}, \text{ and } \mathbf{q}_e(\mathbf{x}, \mathbf{x}_e) = \frac{\partial \mathbf{m}_e(\mathbf{x}, \mathbf{x}_e)}{\partial \mathbf{c}(\mathbf{x}_e)}.$$

The parameter τ^e is an indicator of whether or not imaging data exist in the current element [7]. If no imaging data exists in the element the value of τ^e becomes zero and the first integral in Equation (5-9) is eliminated, otherwise the value of τ^e is set to unity (1).

Minimizing the equation by setting the LHS of Equation (5-9) to zero,

Let

$$\mathbf{d}(\mathbf{x}, \mathbf{x}_e) = \mathbf{h}(\mathbf{x}, \mathbf{x}_e) \mathbf{l}_e(\mathbf{x}, \mathbf{x}_e) + \mathbf{o}(\mathbf{x}, \mathbf{x}_e) \mathbf{n}_e(\mathbf{x}, \mathbf{x}_e) + \mathbf{t}(\mathbf{x}, \mathbf{x}_e) \mathbf{p}_e(\mathbf{x}, \mathbf{x}_e) + \mathbf{m}(\mathbf{x}, \mathbf{x}_e) \mathbf{q}_e(\mathbf{x}, \mathbf{x}_e) \quad (5-10)$$

$$0 = \tau^e \alpha [\mathbf{f}_{4DCT}(\mathbf{x}) + \sum_{e=0}^q \mathbf{h}(\mathbf{x}, \mathbf{x}_e) \mathbf{c}(\mathbf{x}_e) \mathbf{l}_e(\mathbf{x}, \mathbf{x}_e)] + \sum_{e=0}^q \mathbf{d}(\mathbf{x}, \mathbf{x}_e) [\mathbf{c}(\mathbf{x}_e) - \boldsymbol{\gamma}(\mathbf{x}_e)] \quad (5-11)$$

The equation can be further simplified as,

$$0 = \tau^e \alpha [\mathbf{f}_{4DCT}(\mathbf{x}) + \sum_{e=0}^q \mathbf{h} \mathbf{l}_e(\mathbf{x}, \mathbf{x}_e) \mathbf{c}(\mathbf{x}_e)] + \sum_{e=0}^q \mathbf{d}(\mathbf{x}, \mathbf{x}_e) [\mathbf{c}(\mathbf{x}_e) - \boldsymbol{\gamma}(\mathbf{x}_e)] \quad (5-12)$$

Let

$$\mathbf{d}'(\mathbf{x}, \mathbf{x}_e) = \mathbf{d}(\mathbf{x}, \mathbf{x}_e) + \tau^e \alpha \mathbf{h} \mathbf{l}_e(\mathbf{x}, \mathbf{x}_e) \quad (5-13)$$

$$0 = \tau^e \alpha \mathbf{f}_{4DCT}(\mathbf{x}) + \sum_{e=0}^q \mathbf{d}'(\mathbf{x}, \mathbf{x}_e) \mathbf{c}(\mathbf{x}_e) - \sum_{e=0}^q \mathbf{d}(\mathbf{x}, \mathbf{x}_e) \boldsymbol{\gamma}(\mathbf{x}_e) \quad (5-14)$$

$$\sum_{e=0}^q \mathbf{d}'(\mathbf{x}, \mathbf{x}_e) \mathbf{c}(\mathbf{x}_e) = \sum_{e=0}^q \mathbf{d}(\mathbf{x}, \mathbf{x}_e) \boldsymbol{\gamma}(\mathbf{x}_e) - \tau^e \alpha \mathbf{f}_{4DCT}(\mathbf{x}) \quad (5-15)$$

Now, we have two convolutions in a discrete domain on either side of the formulation, thus Hyper Spherical Harmonic (HSH) transformations are applied on either side of Equation (5-15) to get the following relation for $\mathbf{c}(\mathbf{x}_e)$. As a first step towards this process, we rewrite the $\mathbf{c}(\mathbf{x}_e)$ and $\boldsymbol{\gamma}(\mathbf{x}_e)$ using Hyper Spherical coordinates with a rotational invariant notation as follows [22],

$$\mathbf{c}(\mathbf{x}_e) = \mathbf{c}(\mathbf{r}_{(\theta_e, \varphi_e, \chi_e)}(\theta_0, \varphi_0, \chi_0)) \quad (5-16)$$

$$\boldsymbol{\gamma}(\mathbf{x}_e) = \boldsymbol{\gamma}(\mathbf{r}_{(\theta_e, \varphi_e, \chi_e)}(\theta_0, \varphi_0, \chi_0)) \quad (5-17)$$

In the above two equations, $(\theta_e, \varphi_e, \chi_e)$ represents the coordinate system for \mathbf{x}_e and $(\theta_0, \varphi_0, \chi_0)$ represents the coordinate origin. The term $\mathbf{r}_{(\theta_e, \varphi_e, \chi_e)}(\theta_0, \varphi_0, \chi_0)$ represents the SO(3) group rotation of the origin $(\theta_0, \varphi_0, \chi_0)$ by the angle $(\theta_e, \varphi_e, \chi_e)$. Such a group rotation term enables us to define Equations (5-16) and (5-17) in terms of the origin and then subsequently rotate the origin to the location given by $(\theta_e, \varphi_e, \chi_e)$. We now expand the formulation in Equation (5-16) and Equation (5-17) using HSH transformation thus,

$$\mathbf{c}(\mathbf{r}_{(\theta_e, \varphi_e, \chi_e)}(\theta_0, \varphi_0, \chi_0)) = \sum_{\lambda_1} \sum_{l_1} \sum_{m_1} \sum_{n_1} \mathbf{c}_{\lambda_1 l_1 m_1} \mathbf{Y}_{l_1 n_1} \mathbf{S}_{\lambda_1 m_1 n_1}(\theta_e, \varphi_e, \chi_e) \quad (5-18)$$

$$\mathbf{Y}\left(\mathbf{R}_{(\theta_e, \varphi_e, \chi_e)}(\theta_0, \varphi_0, \chi_0)\right) = \sum_{\lambda_1} \sum_{l_1} \sum_{m_1} \sum_{n_1} \mathbf{Y}_{\lambda_1 l_1 m_1} \mathbf{Y}_{\lambda_1 l_1 m_1} \mathbf{S}_{\lambda_1 m_1 n_1}(\theta_e, \varphi_e, \chi_e) \quad (5-19)$$

In the above two equations, the term $\mathbf{S}_{\lambda_1 m_1 n_1}(\theta_e, \varphi_e, \chi_e)$ refers to the 3D HSH transformation of the SO(3) rotation and $\mathbf{Y}_{\lambda_1 l_1 n_1}$ represents the HSH transformation of the input data. For detailed definition of these terms, see [22]. We now expand \mathbf{d} and \mathbf{d}' using HSH transformation as follows:

$$\mathbf{d}(\theta, \varphi, \chi, \theta_e, \varphi_e, \chi_e) = \sum_{\lambda_2} \sum_{l_2} \sum_{\lambda'_2} \sum_{l'_2} \sum_{m'_2} \mathbf{d}_{\lambda_2 l_2 \lambda'_2 l'_2 m'_2} \left(\mathbf{Y}_{\lambda_2 l_2 m'_2}^*(\theta_e, \varphi_e, \chi_e) \right) \mathbf{Y}_{\lambda'_2 l'_2 m'_2}(\theta, \varphi, \chi) \quad (5-20)$$

$$\mathbf{d}'(\theta, \varphi, \chi, \theta_e, \varphi_e, \chi_e) = \sum_{\lambda_2} \sum_{l_2} \sum_{\lambda'_2} \sum_{l'_2} \sum_{m'_2} \mathbf{d}'_{\lambda_2 l_2 \lambda'_2 l'_2 m'_2} \left(\mathbf{Y}_{\lambda_2 l_2 m'_2}^*(\theta_e, \varphi_e, \chi_e) \right) \mathbf{Y}_{\lambda'_2 l'_2 m'_2}(\theta, \varphi, \chi) \quad (5-21)$$

The term $\tau^e \alpha \mathbf{f}_{4DCT}(\mathbf{x})$, which is on the RHS of Equation (5-15) can be expanded as

$$\tau^e \alpha \mathbf{f}_{4DCT}(\theta, \varphi, \chi) = \sum_{\lambda} \sum_l \sum_m \tau^e \alpha \mathbf{f}_{4DCT}(\theta, \varphi, \chi) \delta(\lambda) \delta(l) \delta(m) \quad (5-22)$$

where δ is the Dirac delta function.

The first term of the RHS of Equation (5-15) can be expanded as

$$\sum_{\lambda_1} \sum_{l_1} \sum_{m_1} \sum_{n_1} \sum_{\lambda_2} \sum_{l_2} \sum_{\lambda'_2} \sum_{l'_2} \sum_{m'_2} \mathbf{Y}_{\lambda_1 l_1 m_1} \mathbf{d}_{\lambda_2 l_2 \lambda'_2 l'_2 m'_2} \mathbf{S}_{\lambda_1 m_1 n_1}(\theta_e, \varphi_e, \chi_e) \mathbf{Y}_{l'_2 m'_2}(\theta_0, \varphi_0, \chi_0) \mathbf{B}_{\lambda_1 l_1 n_1 \lambda'_2 l'_2 m'_2} \quad (5-23)$$

where

$$\mathbf{B}_{\lambda_1 l_1 n_1 \lambda'_2 l'_2 m'_2} = \delta_{\lambda_1 \lambda'_2} \delta_{l_1 l'_2} \delta_{n_1 m'_2} \quad (5-24)$$

The term can be further simplified as

$$\sum_{\lambda_1} \sum_{l_1} \sum_{m_1} \sum_{\lambda_2} \sum_{l_2} \sum_{m_2} \mathbf{Y}_{\lambda_1 l_1 m_1} \mathbf{d}_{\lambda_1 l_1 \lambda_2 l_2 n_1} \mathbf{S}_{\lambda_1 m_1 n_1}(\theta_e, \varphi_e, \chi_e) \mathbf{Y}_{\lambda_2 l_2 n_1}'(\theta_0, \varphi_0, \chi_0) + Q(\theta, \varphi, \chi) \quad (5-25)$$

where $Q(\theta, \varphi, \chi)$ is a constant term.

Similarly the LHS of Equation (5-15) can be simplified using HSH transformation

$$\sum_{\lambda_1} \sum_{l_1} \sum_{m_1} \sum_{\lambda_2} \sum_{l_2} \sum_{n_1} \mathbf{c}_{\lambda_1 l_1 m_1} \mathbf{d}'_{\lambda_1 l_1 \lambda_2 l_2 n_1} \mathbf{S}_{\lambda_1 m_1 n_1}(\theta_e, \varphi_e, \chi_e) \mathbf{Y}_{l_2 n_1}'(\theta_0, \varphi_0, \chi_0) \quad (5-26)$$

Equating the frequency coefficients for $\lambda_1 l_1 m_1 \neq 0$ we get

$$\mathbf{c}_{\lambda_1 l_1 m_1} = \frac{\sum_{\lambda_2} \sum_{l_2} \sum_{n_1} \mathbf{d}'_{\lambda_1 l_1 \lambda_2 l_2 n_1} * \mathbf{Y}_{\lambda_1 l_1 m_1}}{\sum_{\lambda_2} \sum_{l_2} \sum_{n_1} \mathbf{d}_{\lambda_1 l_1 \lambda_2 l_2 n_1}} \quad (5-27)$$

and for $\lambda_1 l_1 m_1 = 0$ we get:

$$\mathbf{c}_{000} = \frac{\sum_{\lambda_2} \sum_{l_2} \sum_{n_1} \mathbf{d}'_{00 \lambda_2 l_2 n_1} * \mathbf{Y}_{000} + [\text{constant } Q(\theta, \varphi, \chi)]}{\sum_{\lambda_2} \sum_{l_2} \sum_{n_1} \mathbf{d}_{00 \lambda_2 l_2 n_1}} \quad (5-28)$$

It can be seen that the formulation is analytical in nature, i.e. for known values of \mathbf{f}_{4DCT} and the subsequent nodal values of the CFD analysis, $\mathbf{c}_{\lambda_1 l_1 m_1}$ can be calculated and ultimately the \mathbf{f}_{opt} can be estimated. The formulation by itself is a non-iterative direct solution.

CHAPTER 6: EFFECT OF GRAVITY ON SUBJECT-SPECIFIC HUMAN LUNG DEFORMATION

6.1 Introduction

Biomechanical modeling of human lung dynamics has attracted significant attention in recent years due to its potential utility in radiotherapy. Such physics- and physiology-based models enable precise prediction of respiration-induced lung deformation during which is crucial for tumor localization and targeted radiotherapy in patients with lung cancer. Accurate estimation of lung deformation requires a model that considers all the contributing factors. The effect of one such factors, gravity on lung deformation is systematically considered here as well as the effect on the the accuracy of numerical results.

There is considerable physiological and experimental evidence of the effect of gravity on lung dynamics [54-57]. Specifically, it has been shown that regional lung expansion and variation in pleural pressure is largely determined by gravity [58, 59]. These initial studies were instrumental in demonstrating the importance of gravity on lung deformation. However, most of the previous mathematical modeling studies were based on simplified geometry and computational techniques.

The integration of biomechanical modeling with patient-specific lung data has been a subject of recent investigations [49, 50, 53]. The simulations were typically performed on three-dimensional (3D) lung geometry reconstructed from 4DCT scan dataset of real human patients. The breathing process was modelled by applying prescribed displacement [53] or pressure [28, 35] boundary condition on the surface of the lung. Most of these models however have largely ignored the effect

of gravity. In addition, the models most often rely on simplified material property data derived from animal studies.

The biomechanical model considered here uses the geometry and heterogeneous elastic properties obtained for a real human patient to systematically investigate the contribution of gravity to lung deformation. The simulation employs a porous flow-structure interaction (PFSI) technique to simultaneously solve the coupled airflow and structural dynamics equations of the lung tissue. The following section describes details of the material properties and the method of solution of the dynamical equations.

6.2 Materials and Methods

6.2.1 *Geometry Reconstruction and Mesh Generation*

The lung geometry is derived from 4DCT scan dataset of a real human patient acquired at the University of California, Los Angeles (UCLA), Department of Radiation Oncology. The surface of the lung is reconstructed using Mimics commercial code [116] and geometry modification and meshing are performed using 3-matic code [117]. Figure 6-1(a) to (d) show the images of the lung in the frontal, horizontal, lateral, and 3D views, respectively. Figure 6-2 shows the 3D shape of the lung derived from the 4DCT scans and used for this study.

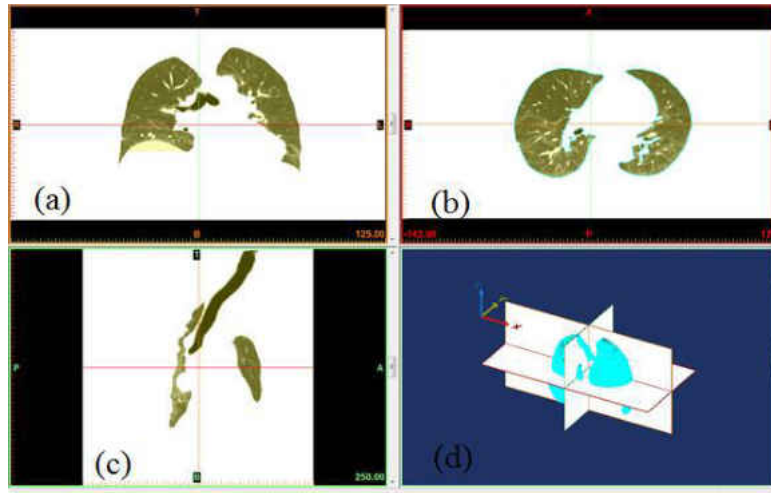


Figure 6-1: Images of human lungs in (a) frontal (b) horizontal(c) lateral, and (d) 3D views

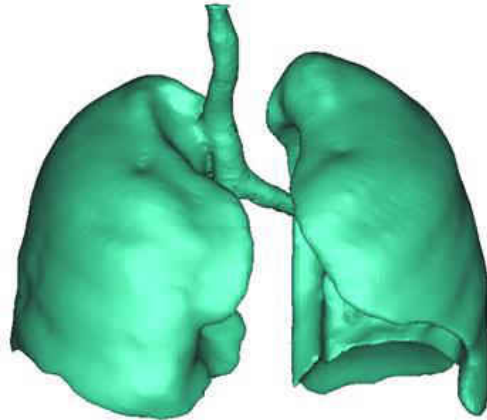


Figure 6-2: Three-dimensional geometry of human lung reconstructed from 4DCT scans

6.2.2 Governing Equations

The lung tissue is assumed to be linear and isotropic [90]. It should be noted that isotropy is assumed only at the elemental level while the YM is allowed to vary from one element to another. Allowance is made for geometric nonlinearity by assuming the deformation to be large. A Lagrangian formulation is used for the solid domain. Unlike the conventional fluid-structure interaction approach in which the fluid and structural variables are coupled only at the interface, the porous fluid structure interaction approach enables coupling in the whole porous medium through displacement and traction conditions [88]. The microscopic fluid stress is added to the structural model as an internal stress. The stresses in the porous medium are thus expressed as:

$$\boldsymbol{\sigma}_f = -P_f \mathbf{I} \quad (6-1)$$

$$\boldsymbol{\sigma}_s^t = \boldsymbol{\sigma}_s - P_f \mathbf{I} \quad (6-2)$$

where $\boldsymbol{\sigma}_f$, $\boldsymbol{\sigma}_s$ represent respectively the Cauchy stress tensor of the pore fluid and Cauchy stress tensor of the skeleton, $\boldsymbol{\sigma}_s^t$ is the total Cauchy stress in solid and \mathbf{I} is the identity matrix. The total stress must satisfy the equilibrium condition:

$$\nabla \cdot \boldsymbol{\sigma}_s^t + \rho_s \mathbf{f} = 0 \quad (6-3)$$

where ρ_s and \mathbf{f} represent the density of the tissue and gravity force, respectively. Lungs are subjected to deformation caused by breathing and gravity. Equation (6-3) shows that in the equilibrium state, gravity force should be balanced by the inner lung reacting forces specified by the Cauchy stress tensor $\boldsymbol{\sigma}_s^t$.

The resulting trans-pulmonary pressure (Ptp) in the presence of gravity is the sum of the assumed value of Ptp in the absence of gravity (1 cmH₂O in this study) and the change in pressure caused by gravity. Gravity can change the transpulmonary pressure by -0.6 cmH₂O in the supine body position [58]. Thus it can caused marked characteristic changes in the resulting trans-pulmonary pressure and lung volume.

The total Cauchy stress tensor in the solid is transformed to the second Piola-Kirchhoff stress tensor \mathbf{S} according to the equation:

$$\mathbf{S}_s^t = J \mathbf{F}^{-1} \cdot \boldsymbol{\sigma}_s^t \cdot \mathbf{F}^{-T} \quad (6-4)$$

where $\mathbf{F} = \mathbf{I} - \nabla_0 \mathbf{u}$ is the deformation gradient tensor and $J = \det \mathbf{F}$. Thus the total stress in the solid becomes:

$$\mathbf{S}_s^t = \mathbf{S}_s - J \mathbf{F}^{-1} P_f \mathbf{F}^{-T} \quad (6-5)$$

The constitutive equation in the solid domain for the generalized De Saint Venant-Kirchhoff elasticity model employed is given by the generalized Hooke's law:

$$\mathbf{S}_s = \mathbf{C} : \mathbf{E} \quad (6-6)$$

where \mathbf{C} is the tangent operator which is dependent only on two constants (the Young's modulus and the Poisson ratio) and \mathbf{E} represents the Green-Lagrangian strain tensor defined as:

$$\mathbf{E} = \frac{1}{2} (\mathbf{F}^T \cdot \mathbf{F} - \mathbf{I}) \quad (6-7)$$

The governing equation for the total stress in the solid is the momentum equation given by:

$$\rho_s \frac{D^2(\mathbf{u}_s)}{Dt^2} = \nabla \cdot (\mathbf{F} \cdot \mathbf{S}_s^t) + \rho_s \mathbf{f} \quad (6-8)$$

where \mathbf{u}_s represents the displacement vector in the solid domain and ρ_s and \mathbf{f} represent the density of the tissue and gravity force, respectively. Displacement is interpreted to be an estimate of the lung motion field during breathing (from end of expiration to end of inhalation).

The Arbitrary Lagrange-Euler (ALE) formulation is applied to the deformable fluid domain. The pore fluid flows through the porous solid structure according to the Darcy's law [88], thus:

$$\frac{\mu_f}{K} \cdot (\mathbf{v} - \mathbf{w}) + \nabla P_f + \rho_f \mathbf{g} = \mathbf{0} \quad (6-9)$$

where K , μ_f and ρ_f represent the permeability tensor, viscosity and density of air, respectively. \mathbf{v} is the air velocity vector, \mathbf{w} represents the moving mesh velocity vector, P_f is the pore pressure, and \mathbf{g} is the gravity vector.

The compatibility of displacement/velocity must be satisfied in the whole porous medium, thus;

$$\mathbf{u}_s = \mathbf{u}_f \quad (x, y, z) \in \Omega_p \quad (6-10)$$

where \mathbf{u}_f is the fluid displacement and Ω_p represents the porous domain. This condition also ensures that the moving mesh velocity in the previous Equation (4-9) is identical to the solid velocity ($\mathbf{w} = \dot{\mathbf{u}}_s$) in the porous medium.

6.2.3 Computational Details

The lung is assumed to be a porous medium with fluid and solid domains coexisting. Thus, the entire lung is considered the geometry for both the fluid and solid. The model used 330,933

tetrahedral volume meshes for both the solid and fluid domains for the left lung, and 390,164 tetrahedral elements for the right lung. The meshes are utilized in the ADINA commercial code [91] for numerical solution of the governing equations described in the previous section 6.2.2.

The iterative two-way coupling or partitioned method embodied in ADINA [91] is applied to solve the coupled fluid-structure problem in order to predict the spatio-temporal lung deformation. In this approach, the fluid and solid equations are solved independently in a sequence, using the most recent information from another part of the coupled system. This iteration is repeated until convergence is achieved in the solution.

6.2.4 *Input Data*

The values of the physiological parameters for the tissue stiffness (Young's modulus, YM, and Poisson's ratio) are defined only for the solid. The spatially-dependent YM values are estimated using inverse analysis from a model for the same lung geometry. The method is based on the approach discussed in a previous study [22]. The lung is decomposed into voxel points and each voxel point is associated with a single YM and a common Poisson's ratio of 0.35 which falls within the range (0.25–0.47) suggested in previous studies [51, 118]. The maximum and minimum YM values obtained for a single voxel point are 4.03 kPa and 0.01 kPa at the bottom and top of the lobe respectively. The airflow is assumed unsteady and laminar. The fluid is assumed to be Newtonian and incompressible with density and viscosity of $\rho_f = 1.205 \text{ kgm}^{-3}$ and $\mu_f = 1.83 \times 10^{-5} \text{ kgm}^{-1}\text{s}^{-1}$.

6.2.5 *Boundary Condition and Applied Loading*

Lung inflation is due to pressure induced by the respiratory muscles of the diaphragm and rib cages. Taking the initial state of breathing to be the end of expiration with zero pressure as a reference, the contraction of the respiratory muscles causes pressure to become negative and its magnitude increases gradually during inspiration and air enters the lungs. The lungs are thus pulled open. When the respiratory muscles relax, the magnitude of pressure decreases, the lung volume decreases and air is expelled. For realistic simulation of breathing mechanics in the present study a periodic pressure boundary condition is imposed on the surface of the lung over the breathing cycle and a stress-free boundary condition is imposed at the inlet assumed to be at the hilum. Thus, the resulting tissue motion is due to surface pressure and gravity. The pressure applied on the lung for a given change in volume is computed using the pressure-volume curve measurement [107]. Mass proportional loading is used to model gravity loading interpreted as a physical body force and is used in the construction of gravity acceleration thus:

$$a_i^t = f(t).A_i.g \quad i = x, y, z \quad (6-11)$$

where $f(t)$ is the value of the time function, A_i is the vector giving the direction of gravity, and g is magnitude of gravity. In this study the 4DCT scans were acquired when the patient lay in the supine body position during radiotherapy. Therefore our calculation assumes this supine body position and gravity is applied in the y (posterior) direction, giving $a_y^t = g$. Figure 6-3 shows the direction of the gravity assumed in the study.

The time functions used for gravity loading and surface pressure are shown in Figure 6-4 in which the time function represented by the solid line defines the load increments used for gravity loading.

Pressure loading is applied in the load steps using a different time function, represented by the dash line in Figure 6-4. Hence, during the final five seconds, the response of the structure is due to both the maximum gravity loading and surface pressure loading.

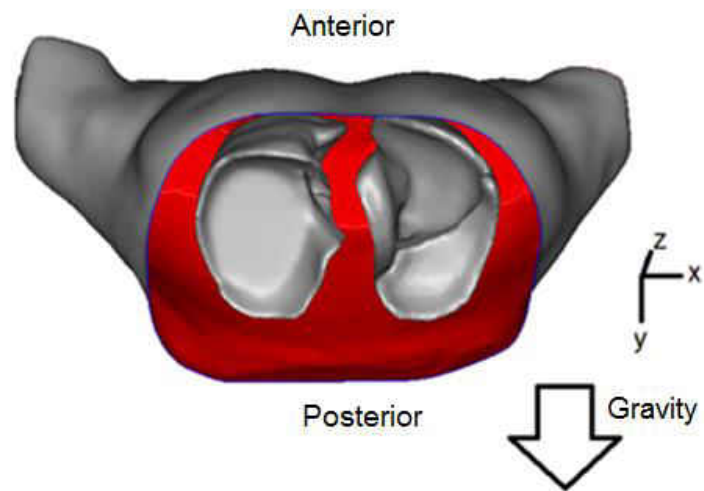


Figure 6-3: Gravity direction assumed in the model

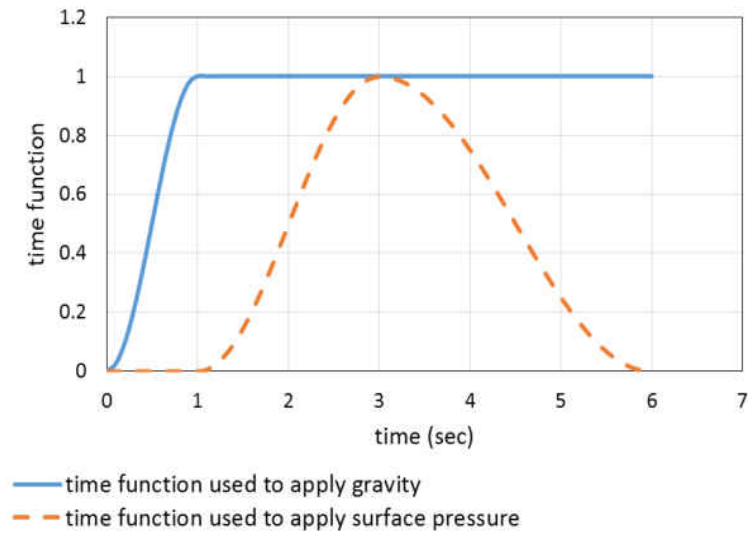


Figure 6-4: Time functions used in the simulation

6.3 Results

The following presentation first concerns the deformation predicted with allowance for gravity. Next, the predictions with and without gravity are compared. The transient displacements in the x (left-right), y (anterior-posterior), and z (superior-inferior) directions at selected landmarks are also monitored and analyzed.

Figure 6-5(a) and Figure 6-5(b) show the predicted magnitude of deformation (in mm) due to gravity loading in the supine body position for the left and right lungs, respectively. The average magnitude of displacement over the left lung is 1.1 mm and the maximum is 2.1 mm. The corresponding values for the right lung are 1.4 mm and 2.5 mm. The displacement generally increases from top to bottom (i.e. superior-inferior direction). The local displacement pattern

depends on the shape of the lung, the distribution of the elastic properties, and the location where the lung is anchored. Note that the lung is anchored at the top and root (hilum) in the biomechanical model to be consistent with the imaging data.

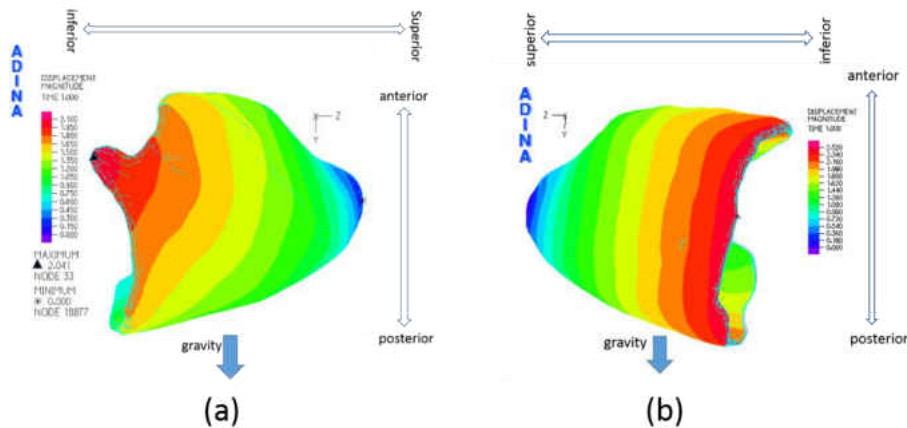


Figure 6-5: Predicted magnitude of deformation (in mm) due to the weight of the lung (gravity-induced deformation) in (a) left lung, (b) right lung

Figure 6-6 (a) and Figure 6-6 (b) show the predicted displacement in the x (left-right), y (anterior-posterior), and z (superior-inferior) directions without and with gravity, respectively. Note that boundary pressure is the only load applied in the case without gravity. Figure 6-6 shows that gravity changes both the magnitude and distribution of the displacements especially in the y direction along which gravity is aligned. The z-displacement is less affected because of the dominant role of inspiration-induced displacement in that direction.

Gravity increases the maximum x-displacement by 15% and 30% in the left and right lungs, respectively. The absolute minimum displacement increases by 9% in the left lung and 3% in the right lung. Incorporation gravity increases the maximum y-displacement by 63% and the minimum y-displacement by 40% in the left lung. Correspondingly, the maximum y-displacement increases by 46% and the minimum values decrease by 29% in the right lung. The location of the maximum y-displacement is also changed by the presence of gravity. The maximum z-displacement in the left lung increases by 16% and the minimum z-displacement decreases by 18% with allowance for gravity. The corresponding values for the right lung decreases by 8% and 2%.

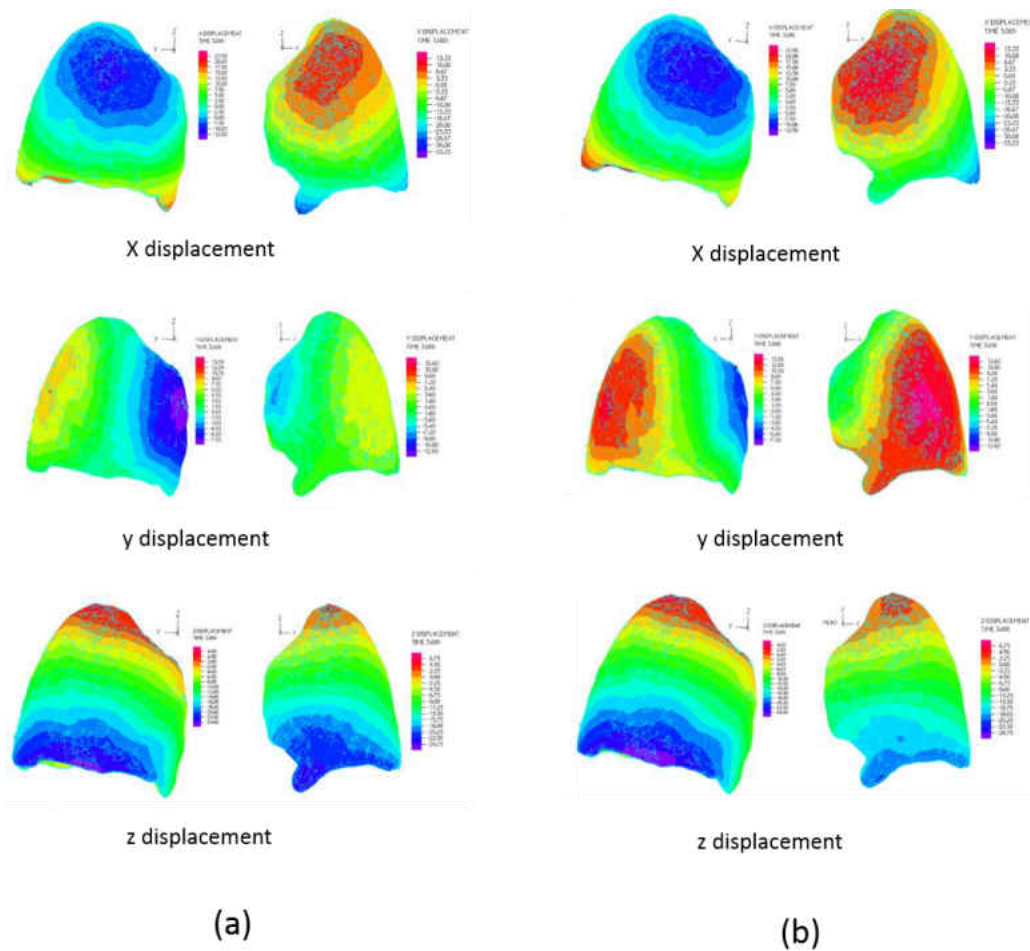


Figure 6-6: Predicted displacement in x, y, and z direction (in mm) due to (a) pressure loading only, and (b) both maximum gravity loading and pressure loading

In order to investigate the regional effect of gravity on the predicted deformation, cut-out views of specific slices of the lung in the transverse planes near the top, middle and bottom of the lung are presented in Figure 6-7. Figure 6-7 (a) and Figure 6-7 (b) show the predicted y-displacement in the selected slices without and with gravity, respectively. The predicted magnitude and distribution of the displacement are different between two cases. The average absolute y-displacement in the

right lung increases by 52%, 34%, and 11% for layers 1, 2 and 3, respectively. The corresponding results for the left lung are 67%, 48% and 33%. These results show that the effect of gravity on deformation is most significant at the top layer of the lobe and attenuates towards the bottom. This trend is plausible since diaphragm pressure dominates the motion in the lower part of the lobes.

Table 6-1 summarizes the average absolute displacement errors and standard deviation in left-right (LR), anterior-posterior (AP), and superior-inferior (SI) directions for the three layers considered in Figure 6-7. The errors are obtained by calculating the discrepancy observed between the predicted deformation and the deformation observed in 4DCT registration [105] on the same patient. The errors obtained are lower in the model with gravity than without gravity in all cases. Error reduction is more significant in the AP (gravity) direction and for the top layers in the consensus of the predicted trend in the effect of gravity relative to diaphragmatic pressure. The overall AP accuracy for the three layers considered are improved by about 1.1 mm.

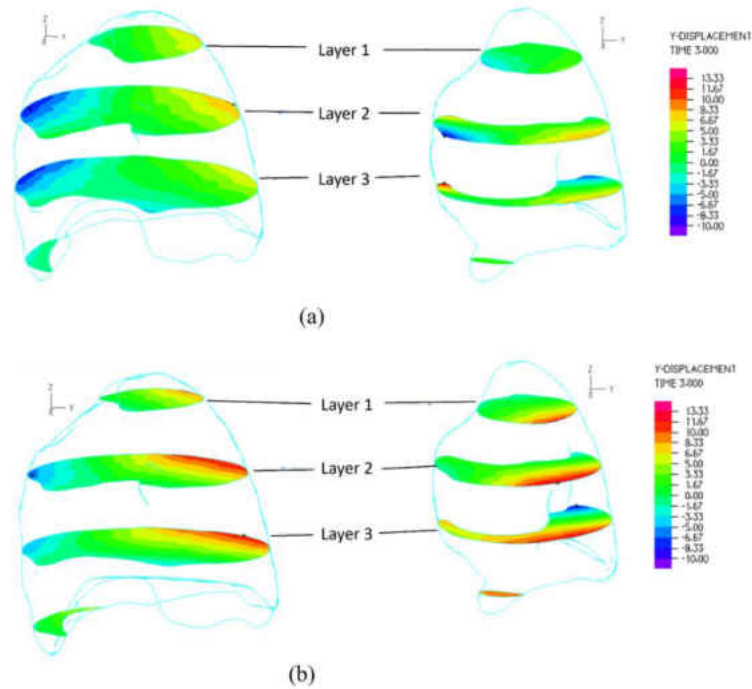


Figure 6-7: Comparison between magnitude of displacement obtained by the model (a) without gravity and (b) with gravity for selected slices in the lung

Table 6-1: Average absolute error of models without and with gravity for 3 layers in Figure 6-7

		Average absolute error (mm)			Average absolute error (mm)		
		without gravity			with gravity		
		LR	AP	SI	LR	AP	SI
Left lung	Layer 1	2.28 ± 1.5	2.94 ± 1.1	2.02 ± 1.7	1.1 ± 1.0	0.95 ± 1.5	1.1 ± 0.96
	Layer 2	2.27 ± 1.3	3.5 ± 0.6	2.4 ± 2.7	1.46 ± 0.4	1.8 ± 1.3	1.75 ± 1.42
	Layer 3	5.5 ± 0.96	3.26 ± 0.17	5.05 ± 1.14	4.8 ± 0.54	2.16 ± 1.18	4.5 ± 3.7
Right lung	Layer 1	1.33 ± 1.2	1.3 ± 2.3	4.63 ± 1.6	0.9 ± 1.15	0.63 ± 1.4	4.2 ± 1.05
	Layer 2	1.57 ± 2.8	1.83 ± 0.6	1.5 ± 0.88	1.16 ± 1.9	1.2 ± 0.1	1.26 ± 0.7
	Layer 3	4.4 ± 2.7	2.53 ± 0.7	4.76 ± 4.0	4.0 ± 0.3	2.24 ± 0.9	4.5 ± 4.6

The effect of gravity on lung deformation can be further quantified by monitoring the transient deformation at specific landmarks on the lobe. Three nodes are monitored on the lung surface, identified as A, B, and C in Figure 6-8, and their displacements along the x, y, and z coordinate directions are analyzed. Node A is at the top surface of the lobe, B is at the outer surface near the rib cage, and C is at the bottom of the lobe. Figure 6-9 shows the x, y, and z displacements of the monitored nodes A, B, and C over one breathing cycle for the two cases considered (with and without gravity loading). The predicted displacements with gravity are represented by dash lines while the displacements without gravity are represented by solid lines. In each case gravity loading was gradually increased to maximum value (g) after 1 sec as shown in Figure 6-4. The inhalation phase begins at $t = 1$ sec and lasts for 2 seconds and expiration phase starts at $t=3$ sec and lasts for 3 seconds. Thus, from $t = 1$ sec to $t = 6$ sec, the resulting deformation is due to both maximum gravity and surface pressure loadings.

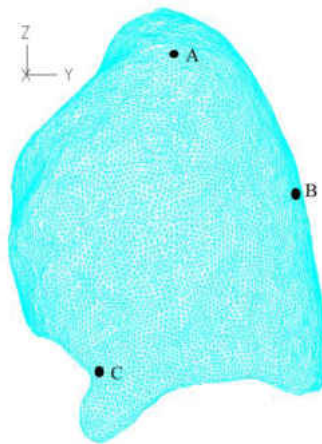


Figure 6-8: Location of monitored landmarks A, B, and C

The predicted peak displacements in the x and y directions for all monitored nodes in the case with gravity are larger than the displacements without gravity. The lung sags downward in the y-direction along which gravity is aligned. As a result, the tissue also remodels and expands in the x-direction. Gravity however minimally affects the z-displacement consistent with the results presented previously in Figure 6-6.

The differences between the x and y deformation of the two models (with and without gravity) increases over the inhalation phase ($t = 1$ sec to $t = 3$ sec) and reach maximum at the end of inhalation ($t=3$ sec). It should be noted that although the initial difference between the deformation of the two cases is quite small at the beginning of the inhalation phase, it could reach up to 10 mm at the end of inhalation at some specific locations such as Node C.

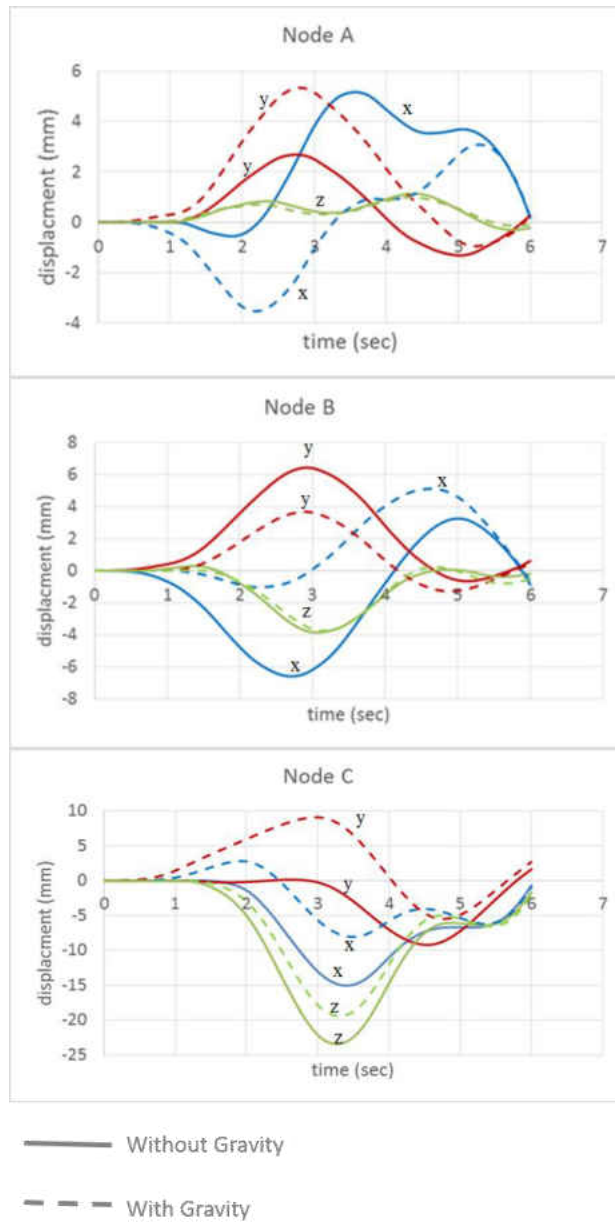


Figure 6-9: Predicted displacements over one breathing cycle for monitored landmarks A, B and, C with and without gravity

6.4 Summary and Conclusions

The study investigated the effect of gravity on lung deformation. A patient-specific biomechanical model of human lung was utilized. The lung assumed to be a poro-elastic medium. A porous flow-structure technique was applied to simultaneously solve the airflow equations and structural dynamics of the lung tissue, with the fluid and solid domains coupled within the lung parenchyma. The lung tissue was assumed to be linear with heterogeneous elastic properties. The major findings of the study can be summarized thus:

- Gravity has a significant effect on lung deformation and improves model accuracy.
- The effect of gravity on deformation is most significant in the direction of gravity. The maximum y-displacements increase by 63% and 46% in the left and right lungs respectively, with allowance for gravity.
- The effect of gravity is less significant in the z (SI) direction since breathing (diaphragmatic pressure) induced deformation is dominant in that direction. The maximum z-displacements increases by 16% and 8% in the left and right lungs respectively, with allowance for gravity.
- The effect of gravity on predicted deformation is regionally dependent and is more significant at the top part of the lung that is remote from the diaphragm.
- The discrepancy between model without and with gravity is small at the beginning of inhalation phase and gradually increases during inhalation phase, and reaches maximum at the end of inhalation.

- The error between predicted displacement and that derived from 4DCT registration is significantly reduced with gravity.

The above findings have profound implication in the optimization and targeting of radiation to tumor in radiotherapy. Allowance for gravity, as this study indicates, significantly affects the resulting spatio-temporal deformation of the lung. Furthermore, it is expected that the effect of gravity will be more significant in pathological cases such as lung cancer in which breathing capacity is severely impaired.

In order to use the finite element modeling for deformable image registration, both efficiency and accuracy are crucial. This study provides a means for improved accuracy of the deformation through incorporation of gravity in the biomechanical model of lung dynamics.

CHAPTER 7: CONCLUSIONS AND FUTURE WORK

7.1 Summary of Chapters

The conclusion from this research are readily summarized according to the findings in the relevant chapters of this dissertation as follows:

Chapter 3, The key contribution of this chapter is the use of patient-specific and heterogeneous elastic properties, and comparison with deformation obtained with homogenous elastic model. Existing simulation studies typically assume homogenous elastic material or a hyper-elastic material, an approach that severely limits the ability to account for patient physiological and pathological conditions. The approach presented in this chapter allows lung inhomogeneity associated with such conditions to be represented.

Chapter 4, The biomechanical model developed was applied to simulate spatial lung deformation and validated with data obtained from 4DCT registration on two human patients. The predicted displacement was found to be significantly improved by allowing for the heterogeneity of lung tissue. The regions near the ribcage and heart exhibit relatively larger displacement errors than the interior of the lungs.

Chapter 5, An algorithm was developed for fusing the quantitative DIR-based displacement and CFD-based fluid-structure interaction simulation data. A description was provided of how the biomechanical modeling outcomes can be combined with the DIR data using the theory of Tikhonov regularization. The quantitative DIR-based data is obtained by means of 4DCT lung

image registration algorithm to estimate lung motion. A heterogeneous poro-elastic model is employed to obtain the CFD solution for lung deformation. The accuracy of the numerical solution is enhanced through fusion with the imaging data beyond the classical comparison between the two sets of data. Such a model will in the future be used for the development of improved lung anatomy models and motion tracking mechanisms that will ultimately lead to an optimal patient radiation- treatment simulator.

Chapter 6, This chapter captures an often left out component of computational modeling for the lung, the effect of gravity. A patient-specific biomechanical model of human lung is developed and the effect of gravity is investigated on lung deformation. Gravity is found to significantly affect lung deformation and improve model accuracy. Effect of gravity on deformation is most significant in the direction along which the gravity is aligned and at the top of the lung, remote from the diaphragm.

7.2 Suggestions for Future Work

The following summarizes recommendations for future studies:

7.2.1 *Broader Application of Fusion Algorithm*

The Fusion Algorithm developed in this study can be applied to any branch of engineering provided that physical model and experimental data are available. In particular, the application of the fusion method can be extended to following:

- 1) *Aerodynamics and flight simulation*: To use the physics of numerical simulations to interpolate and extrapolate the experimental data where the sampling is limited.
- 2) *Weather prediction*: To combine variables such as temperature and atmospheric pressure into the model used in numerical weather prediction.
- 3) *Hydrology*: To integrate measurement and modeling to study the movement and distribution of water on earth.

7.2.2 Determination of Elastic Properties of Human Upper Airway

The method developed in this study for lung can be extended to the upper airways in order to establish the mechanical property and deformation of the oropharyngeal and laryngeal cavities, as well as the trachea. The mechanical properties of airways affect the flow in the trachea as the dynamic effects of rhythmic breathing will significantly affect the simulation of fluid flow in this region. In addition, understanding how these tissues mechanically behave is crucial for accurate modeling of the dynamics of human trachea, simulation of trachea deformation under different loading conditions, and design of endotracheal prostheses.

7.2.3 Improve Computational Time

Computation time is a key limitation for many CFD-based analyses. The proposed method of geometry representation took a few hours to complete the breathing simulation, which represents an improvement over previous run time calculations using full airway geometry. Future work should consider using high performance graphics processing units (GPU) to accelerate the calculations. In addition, the optimization process currently employs an in-house developed code for

performing the analysis. In future, it may be beneficial to design and develop a GPU based version of the optimization process that will enable the system to run much more optimally.

7.2.4 *Pulmonary Fibrosis*

The model developed in this study can be readily extended to study airflow distribution inside the lung and consequently diseases like pulmonary fibrosis. Pulmonary fibrosis is a disease marked by scarring of the tissue inside and between the air sacs in the lungs. The scar can be represented as a region with zero permeability, allowing scar-induced variation in air pressure and distribution to be studied. Such an approach will enable quantification of the relationship between airflow distribution and alveoli blood flow in order to fundamentally understand the cause of pulmonary hypertension and right heart failure in patients with pulmonary fibrosis.

7.2.5 *Modeling Airflow in Human Lung*

The model developed in this dissertation describes a methodology for coupling patient-specific elastic property with computational fluid dynamics (CFD) analysis to effectively predict lung deformation. While the current study focuses lung deformation, accurate prediction of regional airflow distribution is desirable. Such information is crucial to determination of gas exchange, respiratory drug delivery and particle deposition.

Airflow simulation in the lung requires integration of models at airways level with acinar region level, which remains a challenge. This is due to the complexity of multiple bifurcations which in turn results in large scale difference from the trachea to the alveoli [119]. In addition, it is not readily feasible to simulate airflow for each individual alveolar considering their large number (

about 300 million) in the human lung [61]. Subject-specific airway trees obtained by segmentation of medical images remains the most common method to simulate air flow in the lung [120-122]. However, this approach is quiet complex, computationally intensive and impractical. The porous media approach developed in this study enables modeling the airflow and anatomic complexity of the lung parenchyma in a computationally cost-effective manner.

7.2.6 Effect of ribcage on Heterogeneous Model of Human Lung

Another potential future research direction is to integrate the ribcage and chest cavity in the modeling to improve the boundary condition and consequently the accuracy of the biomechanical model. Chest cavity is typically modeled as an elastic body in previous studies but there is no consensus on the values of the elasticity constants used. Future studies should quantify the effect of ribcage on the accuracy of the model as a function of the elastic property assigned to the ribcage. Such studies can demonstrate the feasibility of the contact-surface modeling approach and the significance of the exact knowledge of the material of the organs used in the model.

APPENDIX A: COPYRIGHT PERMISSION

As stated in Chapter 1, most of the materials of Chapter 5 have been previously published in the American Society of Mechanical Engineering (ASME) Journal of Biomechanical Engineering as a technical paper. The paper is reused in this Dissertation with the following permission from ASME.

Dear Mr. Seyfi:

It is our pleasure to grant you permission **to use all or any part of** the following ASME paper “Analytic Intermodel Consistent Modeling of Volumetric Human Lung Dynamics,” by Olusegun Ilegbusi; Behnaz Seyfi; John Neylon; Anand P. Santhanam, J Biomech Eng. 2015; 137(10), cited in your letter for inclusion in a Dissertation entitled INVERSE-CONSISTENT DETERMINATION OF YOUNG’S MODULUS OF HUMAN LUNG to be published by University of Central Florida

Permission is granted for the specific use as stated herein and does not permit further use of the materials without proper authorization. Proper attribution must be made to the author(s) of the materials. **Please note:** if any or all of the figures and/or Tables are of another source, permission should be granted from that outside source or include the reference of the original source. ASME does not grant permission for outside source material that may be referenced in the ASME works.

As is customary, we request that you ensure full acknowledgment of this material, the author(s), source and ASME as original publisher. Acknowledgment must be retained on all pages printed and distributed.

Many thanks for your interest in ASME publications.

Sincerely,



Beth Darchi
Publishing Administrator
ASME
[2 Park Avenue, 6th Floor](#)
[New York, NY 10016-5990](#)
Tel 1.212.591.7700
darchib@asme.org

Figure A-1: ASME permission to reuse the published paper in Chapter 5 of this Dissertation.

APPENDIX B: AUTHOR'S BIOGRAPHY

Behnaz Seyfi Noferest graduated from the K.N. Toosi University of Technology with a Bachelor of Science (B.S.) degree in Physics in 2007. She moved to Orlando, Florida, USA to continue her education in Mechanical Engineering at the University of Central Florida. She earned a Master of Science (M.S.C.E.) and a Doctor of Philosophy (Ph.D.) degree in Mechanical Engineering with focus on Thermo-fluid in 2012 and 2015, respectively.

REFERENCES

- [1] M. R. Kaus and K. K. Brock, "Deformable image registration for radiation therapy planning: algorithms and applications," *Biomechanical Systems Technology: Computational Methods*, pp. 1-28, 2007.
- [2] P. J. Keall, G. S. Mageras, J. M. Balter, R. S. Emery, K. M. Forster, S. B. Jiang, *et al.*, "The management of respiratory motion in radiation oncology report of AAPM Task Group 76," *Medical physics*, vol. 33, p. 3874, 2006.
- [3] A. P. Santhanam, T. Willoughby, A. Shah, S. Meeks, J. P. Rolland, and P. Kupelian, "Real-time simulation of 4D lung tumor radiotherapy using a breathing model," in *Medical Image Computing and Computer-Assisted Intervention–MICCAI 2008*, ed: Springer, 2008, pp. 710-717.
- [4] A. P. Santhanam, Y. Min, J. P. Rolland, C. Imielinska, and P. A. Kupelian, "Four-Dimensional Computed Tomography Lung Registration Methods," *Lung Imaging and Computer Aided Diagnosis*, p. 85, 2011.
- [5] C. Plathow, S. Ley, C. Fink, M. Puderbach, W. Hosch, A. Schmähl, *et al.*, "Analysis of intrathoracic tumor mobility during whole breathing cycle by dynamic MRI," *International Journal of Radiation Oncology* Biology* Physics*, vol. 59, pp. 952-959, 2004.
- [6] A. P. Santhanam, F. G. Hamza-Lup, and J. P. Rolland, "Simulating 3-D lung dynamics using a programmable graphics processing unit," *Information Technology in Biomedicine, IEEE Transactions on*, vol. 11, pp. 497-506, 2007.
- [7] A. N. Tikhonov and V. Y. Arsenin, *Solutions of ill-posed problems*. Washington : New York: Winston ; Halsted Press, 1977.
- [8] M. Levitzky, *Pulmonary Physiology (Lange Physiology)*: McGraw Hill Medical, 2003.
- [9] M. G. Levitzky, *Pulmonary physiology* vol. 7: McGraw-Hill Medical New York, 2007.
- [10] S. J. Lai-Fook, "Pleural mechanics and fluid exchange," *Physiological reviews*, vol. 84, pp. 385-410, 2004.
- [11] M. Toshima, Y. Ohtani, and O. Ohtani, "Three-dimensional architecture of elastin and collagen fiber networks in the human and rat lung," *Archives of Histology and Cytology*, vol. 67, pp. 31-40, 2004.
- [12] L. Wiechert, R. Metzke, and W. A. Wall, "Modeling the mechanical behavior of lung tissue at the microlevel," *Journal of engineering mechanics*, vol. 135, pp. 434-438, 2009.

- [13] J. Hildebrandt, "Pressure-volume data of cat lung interpreted by a plastoelastic, linear viscoelastic model," *Journal of applied physiology*, vol. 28, pp. 365-372, 1970.
- [14] K. K. Brewer, H. Sakai, A. M. Alencar, A. Majumdar, S. P. Arold, K. R. Lutchen, *et al.*, "Lung and alveolar wall elastic and hysteretic behavior in rats: effects of in vivo elastase treatment," *Journal of Applied Physiology*, vol. 95, pp. 1926-1936, 2003.
- [15] S. M. Rausch, D. Haberthür, M. Stampanoni, J. Schittny, and W. Wall, "Local strain distribution in real three-dimensional alveolar geometries," *Annals of biomedical engineering*, vol. 39, pp. 2835-2843, 2011.
- [16] H. Fukaya, C. Martin, A. Young, and S. Katsura, "Mechanical properties of alveolar walls," *Journal of applied physiology*, vol. 25, pp. 689-695, 1968.
- [17] T. Sugihara, C. Martin, and J. Hildebrandt, "Length-tension properties of alveolar wall in man," *Journal of Applied Physiology*, vol. 30, pp. 874-878, 1971.
- [18] J. Gao, W. Huang, and R. Yen, "Mechanical properties of human lung parenchyma," *Biomedical sciences instrumentation*, vol. 42, p. 172, 2006.
- [19] F. Hoppin, G. Lee, and S. Dawson, "Properties of lung parenchyma in distortion," *Journal of Applied Physiology*, vol. 39, pp. 742-751, 1975.
- [20] D. Vawter, Y. Fung, and J. West, "Elasticity of excised dog lung parenchyma," *Journal of Applied Physiology*, vol. 45, pp. 261-269, 1978.
- [21] L. Wilson, D. Robinson, and M. Dadd, "Elastography-the movement begins," *Physics in medicine and biology*, vol. 45, p. 1409, 2000.
- [22] A. P. Santhanam, Y. Min, S. P. Mudur, A. Rastogi, B. H. Ruddy, A. Shah, *et al.*, "An inverse hyper-spherical harmonics-based formulation for reconstructing 3D volumetric lung deformations," *Comptes Rendus Mécanique*, vol. 338, pp. 461-473, 2010.
- [23] B. Goss, K. McGee, S. Kruse, A. Manduca, and R. Ehman, "Magnetic resonance elastography of the lung: Initial feasibility," in *Proceedings of International Society of Magnetic Resonance in Medicine*, 2003, p. 429.
- [24] T. Ebihara, N. Venkatesan, R. Tanaka, and M. S. Ludwig, "Changes in Extracellular Matrix and Tissue Viscoelasticity in Bleomycin-induced Lung Fibrosis: Temporal Aspects," *American journal of respiratory and critical care medicine*, vol. 162, pp. 1569-1576, 2000.
- [25] F. Liu, B. S. Shea, J. D. Mih, A. M. Tager, and D. J. Tschumperlin, "Lung parenchymal tissue stiffness in fibrosis and cellular responses to substrate stiffness," *Biophysical Journal*, vol. 96, p. 395a, 2009.

- [26] Y. Fung, P. Patitucci, and P. Tong, "Stress and strain in the lung," *Journal of the Engineering Mechanics Division*, vol. 104, pp. 201-223, 1978.
- [27] T. Zhang, N. P. Orton, T. R. Mackie, and B. R. Paliwal, "Technical note: A novel boundary condition using contact elements for finite element based deformable image registration," *Medical physics*, vol. 31, p. 2412, 2004.
- [28] O. J. Ilegbusi, B. Seyfi, and R. Salvin, "Patient-specific model of lung deformation using spatially dependent constitutive parameters," *Mathematical and Computer Modelling of Dynamical Systems*, pp. 1-11, 2013.
- [29] G. C. Lee and A. Frankus, "Elasticity properties of lung parenchyma derived from experimental distortion data," *Biophysical journal*, vol. 15, pp. 481-493, 1975.
- [30] Y.-C. Fung, "A theory of elasticity of the lung," *Journal of Applied Mechanics*, vol. 41, p. 8, 1974.
- [31] P. Tong and Y.-C. Fung, "The stress-strain relationship for the skin," *Journal of Biomechanics*, vol. 9, pp. 649-657, 1976.
- [32] Y.-C. Fung, "Stress, deformation, and atelectasis of the lung," *Circulation Research*, vol. 37, pp. 481-496, 1975.
- [33] Y. Zeng, D. Yager, and Y. Fung, "Measurement of the mechanical properties of the human lung tissue," *Journal of biomechanical engineering*, vol. 109, p. 169, 1987.
- [34] S. Rausch, C. Martin, P. Bornemann, S. Uhlig, and W. Wall, "Material model of lung parenchyma based on living precision-cut lung slice testing," *Journal of the Mechanical Behavior of Biomedical Materials*, vol. 4, pp. 583-592, 2011.
- [35] J. Eom, X. G. Xu, S. De, and C. Shi, "Predictive modeling of lung motion over the entire respiratory cycle using measured pressure-volume data, 4DCT images, and finite-element analysis," *Medical physics*, vol. 37, p. 4389, 2010.
- [36] P. Kowalczyk, "Mechanical model of lung parenchyma as a two-phase porous medium," *Transport in porous media*, vol. 11, pp. 281-295, 1993.
- [37] M. A. Lewis and M. R. Owen, "The mechanics of lung tissue under high-frequency ventilation," *SIAM Journal on Applied Mathematics*, vol. 61, pp. 1731-1761, 2001.
- [38] O. J. Ilegbusi, Z. Li, B. Seyfi, Y. Min, S. Meeks, P. Kupelian, *et al.*, "Modeling airflow using subject-specific 4DCT-based deformable volumetric lung models," *Journal of Biomedical Imaging*, vol. 2012, p. 4, 2012.
- [39] A. Krogh, *The comparative physiology of respiratory mechanisms*. Philadelphia: University of Pennsylvania Press 1941.

- [40] J. Mead, T. Takishima, and D. Leith, "Stress distribution in lungs: a model of pulmonary elasticity," *Journal of Applied Physiology*, vol. 28, pp. 596-608, 1970.
- [41] F. Matthews and J. West, "Finite element displacement analysis of a lung," *Journal of Biomechanics*, vol. 5, pp. 591-600, 1972.
- [42] Y. Seppenwoolde, H. Shirato, K. Kitamura, S. Shimizu, M. van Herk, J. V. Lebesque, *et al.*, "Precise and real-time measurement of 3D tumor motion in lung due to breathing and heartbeat, measured during radiotherapy," *International Journal of Radiation Oncology* Biology* Physics*, vol. 53, pp. 822-834, 2002.
- [43] M. J. Murphy and D. Pokhrel, "Optimization of an adaptive neural network to predict breathing," *Medical physics*, vol. 36, p. 40, 2009.
- [44] J. Hymphre, "Continuum biomechanics of soft biological tissues," *Proceedings of the Royal Society of London. Series A, Mathematical and Physical Sciences*, vol. 459, pp. 3-4, 2003.
- [45] H. H. Liu, P. Balter, T. Tutt, B. Choi, J. Zhang, C. Wang, *et al.*, "Assessing respiration-induced tumor motion and internal target volume using four-dimensional computed tomography for radiotherapy of lung cancer," *International Journal of Radiation Oncology* Biology* Physics*, vol. 68, pp. 531-540, 2007.
- [46] A. Al-Mayah, J. Moseley, M. Velec, and K. Brock, "Toward efficient biomechanical-based deformable image registration of lungs for image-guided radiotherapy," *Physics in medicine and biology*, vol. 56, p. 4701, 2011.
- [47] T. J. Carter, M. Sermesant, D. M. Cash, D. C. Barratt, C. Tanner, and D. J. Hawkes, "Application of soft tissue modelling to image-guided surgery," *Medical engineering & physics*, vol. 27, pp. 893-909, 2005.
- [48] S. Sundaram and C. Feng, "Finite element analysis of the human thorax," *Journal of Biomechanics*, vol. 10, pp. 505-516, 1977.
- [49] K. Brock, M. Sharpe, L. Dawson, S. Kim, and D. Jaffray, "Accuracy of finite element model-based multi-organ deformable image registration," *Medical physics*, vol. 32, p. 1647, 2005.
- [50] P.-F. Villard, M. Beuve, B. Shariat, V. Baudet, and F. Jaillet, "Simulation of lung behaviour with finite elements: Influence of bio-mechanical parameters," in *Medical Information Visualisation-Biomedical Visualisation, 2005.(MediVis 2005). Proceedings. Third International Conference on, 2005*, pp. 9-14.

- [51] R. Werner, J. Ehrhardt, R. Schmidt, and H. Handels, "Modeling respiratory lung motion: A biophysical approach using finite element methods," in *Medical Imaging*, 2008, pp. 69160N-69160N-11.
- [52] M. Li, E. Castillo, X.-L. Zheng, H.-Y. Luo, R. Castillo, Y. Wu, *et al.*, "Modeling lung deformation: A combined deformable image registration method with spatially varying Young's modulus estimates," *Medical physics*, vol. 40, p. 081902, 2013.
- [53] A. Al-Mayah, J. Moseley, and K. Brock, "Contact surface and material nonlinearity modeling of human lungs," *Physics in medicine and biology*, vol. 53, p. 305, 2008.
- [54] D. Bettinelli, C. Kays, O. Bailliart, A. Capderou, P. Techoueyres, J. L. Lachaud, *et al.*, "Effect of gravity and posture on lung mechanics," *J Appl Physiol (1985)*, vol. 93, pp. 2044-52, Dec 2002.
- [55] M. H. Tawhai, M. P. Nash, and E. A. Hoffman, "An imaging-based computational approach to model ventilation distribution and soft-tissue deformation in the ovine lung," *Acad Radiol*, vol. 13, pp. 113-20, Jan 2006.
- [56] M. Rohdin, J. Petersson, P. Sundblad, M. Mure, R. W. Glenny, S. G. Lindahl, *et al.*, "Effects of gravity on lung diffusing capacity and cardiac output in prone and supine humans," *J Appl Physiol (1985)*, vol. 95, pp. 3-10, Jul 2003.
- [57] R. L. Dellaca, D. Bettinelli, C. Kays, P. Techoueyres, J. L. Lachaud, P. Vaida, *et al.*, "Effect of changing the gravity vector on respiratory output and control," *Journal of Applied Physiology*, vol. 97, pp. 1219-1226, 2004.
- [58] S. Ganesan, K. E. Rouch, and S. J. Lai-Fook, "A finite element analysis of the effects of the abdomen on regional lung expansion," *Respiration physiology*, vol. 99, pp. 341-353, 1995.
- [59] A. Bryan, J. Milic-Emili, and D. Pengelly, "Effect of gravity on the distribution of pulmonary ventilation," *Journal of Applied Physiology*, vol. 21, pp. 778-784, 1966.
- [60] J. B. West and F. L. Matthews, "Stresses, strains, and surface pressures in the lung caused by its weight," 1972.
- [61] J. Tu, K. Inthavong, and G. Ahmadi, *Computational fluid and particle dynamics in the human respiratory system*: Springer Science & Business Media, 2012.
- [62] D. Vawter, "A finite element model for macroscopic deformation of the lung," *Journal of biomechanical engineering*, vol. 102, pp. 1-7, 1980.

- [63] E. Bar-Yishay, R. E. Hyatt, and J. R. Rodarte, "Effect of heart weight on distribution of lung surface pressures in vertical dogs," *Journal of Applied Physiology*, vol. 61, pp. 712-718, 1986.
- [64] E. D'Angelo, S. H. Loring, M. E. Gioia, M. Pecchiari, and C. Moscheni, "Friction and lubrication of pleural tissues," *Respiratory physiology & neurobiology*, vol. 142, pp. 55-68, 2004.
- [65] A.-L. Didier, P.-F. Villard, J. Saadé, J.-M. Moreau, M. Beuve, and B. Shariat, "A chest wall model based on rib kinematics," in *Visualisation, 2009. VIZ'09. Second International Conference in*, 2009, pp. 159-164.
- [66] Z.-H. Zhong, *Finite element procedures for contact-impact problems* vol. 7: Oxford university press Oxford, 1993.
- [67] K. Brock, S. Hollister, L. Dawson, and J. Balter, "Technical note: Creating a four-dimensional model of the liver using finite element analysis," *Medical physics*, vol. 29, p. 1403, 2002.
- [68] R. Werner, "Biophysical Modeling of Respiratory Organ Motion," in *4D Modeling and Estimation of Respiratory Motion for Radiation Therapy*, ed: Springer, 2013, pp. 61-84.
- [69] J. Saadé, A.-L. Didier, P.-F. Villard, R. Buttin, J.-M. Moreau, M. Beuve, *et al.*, "A preliminary study for a biomechanical model of the respiratory system," in *Engineering and Computational Sciences for Medical Imaging in Oncology-ECSMIO 2010*, 2010, p. 7.
- [70] Y. Niu, W. Shen, and J. H. Stuhmiller, "Finite element models of rib as an inhomogeneous beam structure under high-speed impacts," *Medical engineering & physics*, vol. 29, pp. 788-798, 2007.
- [71] J. Y. Chang, "Guidelines and Techniques for Image-Guided Radiotherapy for Non-Small Cell Lung Cancer."
- [72] T. J. Carter, C. Tanner, and D. J. Hawkes, "A comparison of linear and quadratic tetrahedral finite elements for image-guided surgery applications," *Medical Images and Signals IRC*, p. 47.
- [73] K. Nisugi, T. Hayase, and A. Shirai, "Fundamental study of hybrid wind tunnel integrating numerical simulation and experiment in analysis of flow field," *JSME International Journal Series B*, vol. 47, pp. 593-604, 2004.
- [74] P. H. Reisenhel, J. F. Love, D. J. Lesieutre, and M. F. Dillenius, "Innovative Fusion of Experiment and Analysis for Missile Design and Flight Simulation," DTIC Document2006.

- [75] T. Hayase, K. Nisugi, and A. Shirai, "Numerical realization for analysis of real flows by integrating computation and measurement," *International journal for numerical methods in fluids*, vol. 47, pp. 543-559, 2005.
- [76] K. Funamoto, T. Hayase, A. Shirai, Y. Saijo, and T. Yambe, "Fundamental Study of Ultrasonic-Measurement-Integrated Simulation of Real Blood Flow in the Aorta," *Annals of Biomedical Engineering*, vol. 33, pp. 415-428, 2005.
- [77] K. Funamoto, Y. Suzuki, T. Hayase, T. Kosugi, and H. Isoda, "Numerical validation of MR-measurement-integrated simulation of blood flow in a cerebral aneurysm," *Ann Biomed Eng*, vol. 37, pp. 1105-16, Jun 2009.
- [78] A. Schmidt-Richberg, J. Ehrhardt, R. Werner, and H. Handels, "Direction-dependent regularization for improved estimation of liver and lung motion in 4D image data," in *SPIE Medical Imaging*, 2010, pp. 76232Y-76232Y-8.
- [79] B. A. Zeldin and A. J. Meade, "Integrating experimental data and mathematical models in simulation of physical systems," *AIAA journal*, vol. 35, pp. 1787-1790, 1997.
- [80] W. Wang, "Exploration of Tikhonov regularization for the fusion of experimental data and computational fluid dynamics," *ETD <http://hdl.handle.net/1911/17309>*, 1999.
- [81] J. Navarrete, "Construction of airfoil performance tables by the fusion of experimental and numerical data," Rice University, 2004.
- [82] D. Yang, W. Lu, D. A. Low, J. O. Deasy, A. J. Hope, and I. El Naqa, "4D-CT motion estimation using deformable image registration and 5D respiratory motion modeling," *Medical physics*, vol. 35, pp. 4577-4590, 2008.
- [83] A. Bharatha, M. Hirose, N. Hata, S. K. Warfield, M. Ferrant, K. H. Zou, *et al.*, "Evaluation of three-dimensional finite element-based deformable registration of pre-and intraoperative prostate imaging," *Medical physics*, vol. 28, pp. 2551-2560, 2001.
- [84] K. K. Brock, L. A. Dawson, M. B. Sharpe, D. J. Moseley, and D. A. Jaffray, "Feasibility of a novel deformable image registration technique to facilitate classification, targeting, and monitoring of tumor and normal tissue," *International Journal of Radiation Oncology* Biology* Physics*, vol. 64, pp. 1245-1254, 2006.
- [85] P. Villard, M. Beuve, B. Shariat, V. Baudet, and F. Jaillet, "Simulation of lung behaviour with finite elements: Influence of bio-mechanical parameters," in *Medical Information Visualisation-Biomedical Visualisation, 2005.(MediVis 2005). Proceedings. Third International Conference on*, 2005, pp. 9-14.

- [86] R. De Wilde, J. Clement, J. Hellemans, M. Decramer, M. Demedts, R. Boving, *et al.*, "Model of elasticity of the human lung," *Journal of Applied Physiology*, vol. 51, pp. 254-261, 1981.
- [87] J. H. Leite-Júnior, P. R. Rocco, D. S. Faffe, P. V. Romero, and W. A. Zin, "On the preparation of lung strip for tissue mechanics measurement," *Respiratory physiology & neurobiology*, vol. 134, pp. 255-262, 2003.
- [88] H. Zhang, X. Zhang, S. Ji, Y. Guo, G. Ledezma, N. Elabbasi, *et al.*, "Recent development of fluid–structure interaction capabilities in the ADINA system," *Computers & structures*, vol. 81, pp. 1071-1085, 2003.
- [89] S. Sobin, Y. Fung, and H. Tremer, "Collagen and elastin fibers in human pulmonary alveolar walls," *Journal of Applied Physiology*, vol. 64, pp. 1659-1675, 1988.
- [90] M. Toshima, Y. Ohtani, and O. Ohtani, "Three-dimensional architecture of elastin and collagen fiber networks in the human and rat lung," *Archives of histology and cytology*, vol. 67, p. 31, 2004.
- [91] ADINA. (2013). *Automatic Dynamic Incremental Nonlinear Analysis*. Available: www.adina.com
- [92] M. Materialise, ed, 2013.
- [93] "3-matic, Materialise Inc.," vol. 5.01, 5.1 ed. Plymouth, MI.
- [94] A. Santhanam, S. P. Mudur, and J. P. Rolland, "An inverse 3D lung deformation analysis for medical visualization," in *Computer Animation and Social Agents*, Switzerland, pp. 229-242.
- [95] P. J. Keall, G. S. Mageras, J. M. Balter, R. S. Emery, K. M. Forster, S. B. Jiang, *et al.*, "The management of respiratory motion in radiation oncology report of AAPM Task Group 76a," *Medical physics*, vol. 33, pp. 3874-3900, 2006.
- [96] Y. Min, A. Santhanam, H. Neelakkantan, B. H. Ruddy, S. L. Meeks, and P. A. Kupelian, "A GPU-based framework for modeling real-time 3D lung tumor conformal dosimetry with subject-specific lung tumor motion," *Physics in Medicine and Biology*, vol. 55, p. 5137, 2010.
- [97] F. L. Matthews and J. B. West, "Finite element displacement analysis of a lung," *Journal of Biomechanics*, vol. 5, pp. 591-600, 1972.
- [98] K. K. Brock, M. B. Sharpe, L. A. Dawson, S. M. Kim, and D. A. Jaffray, "Accuracy of finite element model-based multi-organ deformable image registration," *Medical physics*, vol. 32, pp. 1647-1659, 2005.

- [99] M. J. Murphy and D. Pokhrel, "Optimization of an adaptive neural network to predict breathing," *Medical physics*, vol. 36, pp. 40-47, 2008.
- [100] O. J. Ilegbusi, B. Seyfi, and R. Salvin, "Patient-specific model of lung deformation using spatially dependent constitutive parameters," *Mathematical and Computer Modelling of Dynamical Systems*, vol. 20, pp. 546-556, 2014.
- [101] Y. C. Fung, "A theory of elasticity of the lung," *Journal of Applied Mechanics*, vol. 41, pp. 8-14, 1974.
- [102] Y. C. B. Fung, P. Patitucci, and P. Tong, "Stress and strain in the lung," *Journal of the Engineering Mechanics Division*, vol. 104, pp. 201-223, 1978.
- [103] A. Al-Mayah, J. Moseley, and K. K. Brock, "Contact surface and material nonlinearity modeling of human lungs," *Physics in Medicine and Biology*, vol. 53, p. 305, 2008.
- [104] J. Eom, X. G. Xu, S. De, and C. Shi, "Predictive modeling of lung motion over the entire respiratory cycle using measured pressure-volume data, 4DCT images, and finite-element analysis," *Medical physics*, vol. 37, pp. 4389-4400, 2010.
- [105] L. M. Vaina, S. A. Beardsley, and S. K. Rushton, *Optic flow and beyond* vol. 324: Springer, 2004.
- [106] D. A. Low, B. M. White, P. P. Lee, D. H. Thomas, S. Gaudio, S. S. Jani, *et al.*, "A novel CT acquisition and analysis technique for breathing motion modeling," *Physics in Medicine and Biology*, vol. 58, p. L31, 2013.
- [107] A. P. Santhanam, C. Imielinska, P. Davenport, P. Kupelian, and J. P. Rolland, "Modeling real-time 3-D lung deformations for medical visualization," *Information Technology in Biomedicine, IEEE Transactions on*, vol. 12, pp. 257-270, 2008.
- [108] B. Lande and W. Mitzner, "Analysis of lung parenchyma as a parametric porous medium," *Journal of Applied Physiology*, vol. 101, pp. 926-933, 2006.
- [109] R. ADINA, "ADINA R&D Inc," 9.1 ed. Watertown, MA.
- [110] "Mimics, Materialise Inc.," 13.1 ed.
- [111] J. Y. Chang, "Guidelines and Techniques for Image-Guided Radiotherapy for Non-Small Cell Lung Cancer," in *Image-Guided Radiotherapy of Lung Cancer*, C. J. Y. James D. Cox, Komaki Ritsuko Ed., ed: CRC Press, 2007, pp. 19-38.
- [112] O. Ilegbusi, B. Seyfi, J. Neylon, and A. P. Santhanam, "Analytic Intermodel Consistent Modeling of Volumetric Human Lung Dynamics," *Journal of biomechanical engineering*, vol. 137, p. 101005, 2015.

- [113] B. Seyfi, A. P. Santhanam, and O. J. Ilegbusi, "Application of Fusion Algorithm to Human Lung Dynamics," in *ASME 2012 International Mechanical Engineering Congress and Exposition*, 2012, pp. 239-245.
- [114] L. M. Vaina, S. A. Beardsley, and S. K. Rushton, *Optic flow and beyond* vol. 324: Springer, 2004.
- [115] Y. Min, J. Neylon, A. Shah, S. Meeks, P. Lee, P. Kupelian, *et al.*, "4D-CT Lung registration using anatomy-based multi-level multi-resolution optical flow analysis and thin-plate splines," *International journal of computer assisted radiology and surgery*, pp. 1-15, 2014.
- [116] Materialise. (2013). *Mimics*. Available: <http://www.materialise.com/mimics>
- [117] Materialise. (2013). *3-matic*. Available: <http://www.materialise.com/BiomedicalRnD/3-matic>.
- [118] S. Chhatkuli, S. Koshizuka, and M. Uesaka, "Dynamic tracking of lung deformation during breathing by using particle method," *Modelling and Simulation in Engineering*, vol. 2009, p. 7, 2009.
- [119] E. R. Weibel, *Geometry and dimensions of airways of conductive and transitory zones*: Springer, 1963.
- [120] M. H. Tawhai, E. A. Hoffman, and C. L. Lin, "The lung physiome: merging imaging-based measures with predictive computational models," *Wiley Interdisciplinary Reviews: Systems Biology and Medicine*, vol. 1, pp. 61-72, 2009.
- [121] M. H. Tawhai, P. Hunter, J. Tschirren, J. Reinhardt, G. McLennan, and E. A. Hoffman, "CT-based geometry analysis and finite element models of the human and ovine bronchial tree," *Journal of applied physiology*, vol. 97, pp. 2310-2321, 2004.
- [122] C.-l. Lin, M. H. Tawhai, G. McLennan, and E. A. Hoffman, "Computational fluid dynamics," *Engineering in Medicine and Biology Magazine, IEEE*, vol. 28, pp. 25-33, 2009.